TUM School of Natural Sciences

TUM
TECHNISCHE
UNIVERSITÄT
MÜNCHEN

Meso-scale modeling of the structural, electronic and transport properties governing (dis-)charging processes in lithium intercalated graphite anodes

Simon B. Anniés

1 Abstract

As the primary anode material of lithium ion batteries, lithium intercalated graphite is one of the central materials behind the transition towards a less CO_2-intensive energy economy. In spite of that, the atomistic processes governing (dis-)charging cycles, and limiting the speed, safety and reversibility thereof, are still not sufficiently understood. Specifically, diffusion kinetics, relative energetics of stoichiometrically equivalent intercalant-orderings and non-equilibrium phenomena like charge-density gradients due to fast charging speeds require additional research, so that batteries can be further optimized.

In this work, a new semi-empirical Density-Functional Tight-Binding method was parametrized, making use of modern machine-learning for the generation of the repulsion potential. In doing so, an accuracy comparable to that of state-of-the-art, dispersion-corrected Density Functional Theory calculations can be achieved at a fraction of the computational cost. The method was successfully benchmarked against both structural and energetic system properties. Based on it, accurate diffusion barriers, structural properties and the dielectric response were calculated, all in dependence of the state of charge and the semi-local ordering of the charge carriers. At the same time, the process of combining semi-empirical electronic structure based electrostatics with machine-learned repulsion was rigorously investigated and explained – an approach, which provides great promise for many other systems of interest. [1]

2 Zusammenfassung

Als primäres Anodenmaterial für Lithium-Ionen Batterien spielt mit Lithium interkaliertes Graphit eine zentrale Rolle beim Übergang zu einer weniger CO_2-intensiven Energiewirtschaft. Dennoch sind die atomistischen Prozesse, welche die Lade- und Entladezyklen bestimmen und deren Geschwindigkeit, Sicherheit und Umkehrbarkeit limitieren, bis heute nicht ausreichend verstanden. Insbesondere die Diffusionskinetik, die relative Energetik stoichiometrisch gleichwertiger Interkalant-Verteilungen und Phänomene im Nicht-Gleichgewicht, wie Ladungsdichte-Gradienten wegen schneller Ladegeschwindigkeiten, erfordern zusätzliche Untersuchungen, damit Batterien weiter verbessert werden können.

In dieser Arbeit wurde eine neue, semi-empirische "Density-Functional Tight-Binding" Methode parametrisiert. Dabei wurde zur Erzeugung der Repulsionspotentiale auf modernes maschinelles Lernen zurückgegriffen. Dadurch konnte eine Genauigkeit erreicht werden, welche mit der hochaktueller, dispersionskorrigierter "Density Functional Theory" Berechnungen vergleichbar ist, jedoch nur einen Bruchteil der Rechenzeit erfordert. Die Methode wurde erfolgreich sowohl für strukturelle, als auch für energetische Vergleichswerte des Systems validiert. Mit ihrer Hilfe wurden genaue Diffusionsbarrieren, Struktureigenschaften und die dielektrische Antwort des Systems berechnet, alle in Abhängigkeit vom Ladungszustand und der semi-lokalen Verteilung der Ladungsträger. Gleichzeitig konnte die Vereinigung semi-empirischer Elektronenstruktur und darauf basierender Elektrostatik mit machinell erlernter Repulsion ausführlich erforscht und erklärt werden – ein äußerst vielversprechender Ansatz auch für andere interessante Systeme.

3 List of abbreviations

BEV   battery electric vehicle

DFTB   density functional tight binding

DFT   density functional theory

GAP   Gaussian approximation potential

GPrep   Gaussian process repulsion

GPR   Gaussian process regression

ACE   atomic cluster expansion

PACE   performant atomic cluster expansion

LIB   lithium ion battery

SOC   state of charge

vdW   van der Waals

HOPG   highly oriented pyrolytic graphite

NG   natural graphite

SG   synthetic graphite

FG   flake graphite

MG   micro-crystalline graphite

OCV   open circuit voltage

SEM   scanning electron microscope

GIC   graphite intercalation compound

kMC   kinetic Monte Carlo

DCACP   dispersion corrected atom centered pseudopotential

PBE   Perdew–Burke-Ernzerhof

FF   force field

CC   coupled cluster

LDA   local density approximation

GGA   general gradient approximation

MBD   many-body dispersion

SCC self-consistent charge

ChIMES Chebyshev interaction model for efficient simulation

ZORA zero-order regular approximation

PSO particle swarm optimizer

LJ Lennard Jones

SOAP smooth overlap of atomic positions

Contents

4 Introduction & Motivation

With global warming being one of the greatest challenges mankind is presently facing as a species [2–5], fast technological progress in the field of carbon-neutral, renewable energies will undeniably have to be a central element of any possible solution. Beside the actual generation, by means of solar-, wind- and water-power, storing that fluctuating energy for use at different times and in different places is one of the primary challenges for the transition away from a fossil-fuel based energy economy. Lithium ion batteries are currently, and have been for at least two decades [6], the most important storage medium for a wide range of applications, from small consumer electronics, to battery electric vehicles (BEVs) and even to off-grid energy storage of entire buildings [7]. Even with significant improvements in alternative technology like other battery types, synthetic combustion fuels and hydrogen fuel cells, the great importance of lithium ion batteries (LIBs) is not expected to subside anytime within the next multiple decades. To the contrary, new applications and challenges, like electric mobility, require more efficient, safe and powerful iterations than ever before.

Despite this quickly arising need, the atomistic processes governing the performance of all LIB components - cathodes, electrolytes, and anodes - are not sufficiently understood yet, to harness their full potential. In particular, the currently-used graphite anodes are a limiting factor to charging speed and cycle stability [8], and need to be understood and improved for BEVs to effectively replace combustion vehicles as soon as possible.

Beyond this specific application, we also express a profound methodological interest in the density functional tight binding (DFTB) approach, which we consider a promising, but underused framework for accurate and informative yet affordable electronic structure calculations. According to our assessment, the lack of high-quality parameters available in literature has been the main hindrance regarding the broader adoption of this method, which partially stems from the ambition to provide general, transferable parameters [9, 10] - and thus establishing DFTB as a direct competitor to density functional theory (DFT), especially in terms of usability, without any need for the end-users to perform any parametrization themselves. However, in attempting this, a great deal of accuracy has to be sacrificed (at least up to now).

A fundamentally different approach to utilizing the power of DFTB is the creation of specialized parametrizations for one specific system at a time – operating at the other end of the fundamental compromise and sacrificing transferability for accuracy, as opposed to the other way round. This approach has not been used extensively yet, probably due to the amount of work involved in creating a full parametrization in the past. However, due to the rapid advancements in machine-learned interatomic potentials (like Gaussian process repulsion (GPrep) [11], Gaussian approximation potential (GAP) [12–14] and atomic cluster expansion (ACE)/performant atomic cluster expansion (PACE) [15–17]), both in terms of performance and – equally important – in terms of workflow and usability, we believe that this will change rapidly in the future. Essentially, the repulsion part (see chapter 7.2.7) within the DFTB framework is nothing else but an interatomic potential itself, that is simply trained on the difference between the high-level reference theory (e.g. DFT) and the simplified electronic part (see chapter 7.2.6). In that sense, it can be understood as a Δ-learning approach, which is why we do not view DFTB as a competitor

1

to the previously mentioned atomic potential methods at all, but as an enhancement thereof, benefitting from all the recent progress in the same way, while maintaining the physicality of an explicit (although simplified) electron density, that can be used for calculating band-structures, densities of states, and long-ranged Coulomb interactions beyond the range of the local descriptors, upon which the atomic potentials are constructed.

In this work, we constructed a DFTB-model with a machine-learned repulsion potential based on the GPrep framework, for the system of lithium intercalated graphite. Using this model, we investigated various previously inaccessible properties of the system, like the relative permittivity as a function of the state of charge (SOC), geometric properties of large structural domains and diffusion barriers depending on the surrounding configurations. With this, we hope to contribute to creating direct links between macroscopic and atomistic properties, and consequently to the systematic improvement of current battery technology, as well as the fundamental understanding of new battery-materials.
At the same time, we unravelled the entire parametrization process, giving a step-by-step guide to this process, with respect to the choice of hyper-parameters and training sets, hoping to shine some light on the great potential of DFTB and inspire similar endeavours for different applications in the future.

5   Lithium Ion Batteries

Lithium ion batteries (LIB) were introduced to the market in 1991, thanks to research by John B. Goodenough, M. Stanley Whittingham and Akira Yoshino, who were awarded the 2019 Nobel Prize in chemistry. Since then, LIBs have been by far the most important storage medium for electric power - with a production in the order of many billions per year [18] - in high-demand application like consumer electronics, where high gravimetric and volumetric capacities are crucial [19]. With the necessary transition towards a carbon-neutral energy system and related new applications in e.g. mobility, the importance of energy storage technology will rise significantly, and despite alternatives being actively researched, LIBs are expected to remain among the primary storage media [20]. Broken down to the simplest processes, LIBs consist of two electrodes (the cathode on the positive pole and the anode on the negative pole). They are separated by an electrolyte, which is conductive for cations, but insulating for electrons, and a cable with the opposite properties (see fig 1).
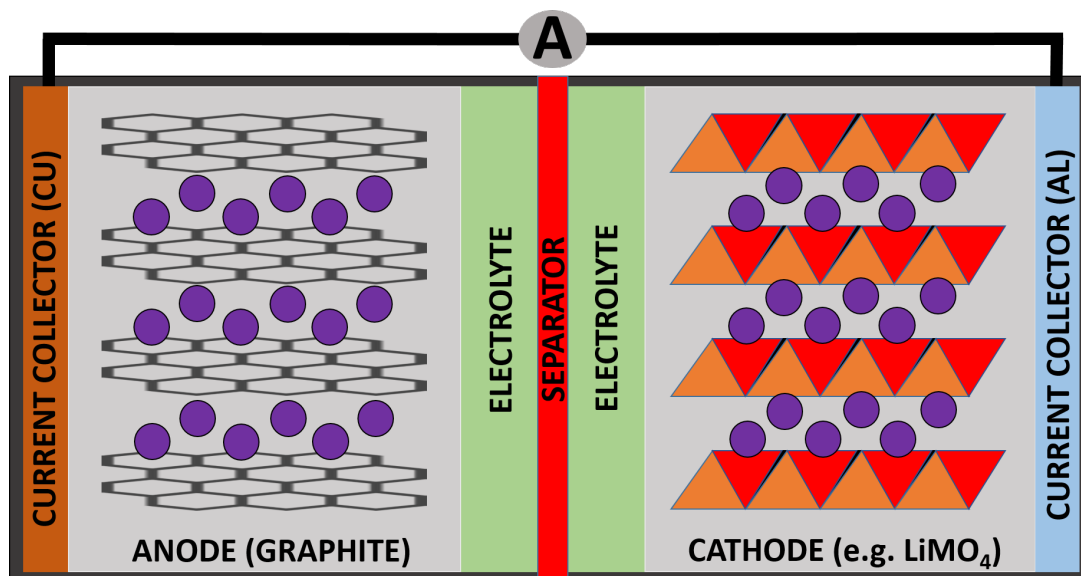

Figure 1: Illustration of a typical lithium ion battery (LIB). In the charged state, the Li-ions (purple spheres) are located in the anode; in the discharged state, they are located in the cathode. Both electrodes are separated by the electrolyte and the separator.

In the charged state, (most of) the lithium content is located in the anode, where it stays as long as the two poles are disconnected. Once the connection is made, the positive lithium ions travel through the electrolyte to the cathode, due to the difference in chemical potential, and the electrons travel through the cable connecting the poles, where they can be accessed as electric energy. The reverse process is achieved by applying an electric field (putting energy in).

In principle, this process is infinitely reversible, but in practice, limitations arise, caused by the degradation of all cell components. This is caused by a plethora of processes, gaining control over which has been the motivation for great research efforts for several decades, an endeavour that still is not close to being concluded. Cycle-stability, safety and fast-charging capabilities

are all still being improved upon by many research teams. [21, 22]

Lithium-deposition is the root cause of many problems LIB-technology still has not completely overcome. It is an umbrella-term for the formation of metallic lithium clusters of variable shapes and sizes, and driven by different processes between the anode and the electrolyte. In ideal equilibrium conditions, lithium intercalation is thermodynamically favoured over lithium deposition, due to a higher chemical potential [23], to a degree that no deposition should occur at all. However, charging and discharging processes do not take place in equilibrium and introduce additional effects which need to be taken into account. So-called over-potentials can be caused by diffusion kinetics, charge transfer and Ohmic drop. These over-potentials can make lithium deposition competitive with intercalation under certain circumstances. This tends to be the case especially at low temperature, for fast charging speed, and for high SOC [24]. In principle, the deposited lithium will still intercalate into the anode if given enough time for equilibration, but this is not always the case in everyday battery use. Furthermore, chunks of deposited metallic lithium can "break off" and move into the electrolyte, becoming so-called "dead" lithium, which is lost for future charging cycles, causing permanent reduction of capacity in the cell [25].

Beyond capacity-loss, lithium deposition also has severe implications for battery safety, as it can cause catastrophic failure by thermal runaway. The most prominent mechanism for this is the growth of so-called lithium dendrites – thin needles which can penetrate the liquid electrolyte and the separator and cause a short circle in the cell, which in turn causes exothermic reactions with the electrolyte. The reason for this phenomenon has been suggested to be an attractive interaction between sharp tips in the deposited lithium metal and the free Li^+ ions in the electrolyte – causing a positive feedback loop for the formation of dendrites instead of evenly plated lithium [26].
This important safety issue can be tackled in multiple ways. On one hand, the on-going development of solid electrolytes has its motivation in preventing dendrites from growing all the way to the cathode [27]. But on the other hand, it is equally important to understand the underlying atomistic mechanisms at the surface of the anode better. Then, it might be possible to avoid (or at least strongly reduce) lithium deposition with all its consequences altogether, by better controlling and managing the conditions within individual cells during charging and discharging processes.

5.1 State of the Art Cell Components

On the cathode side, two different types of material are mostly being used [28, 29]. The first and most common type is a group of layered oxides with the formula $LiMO_2$ (M=Co, Mn, Ni). The composition of the M-elements is the primary focus in research on these materials and can be altered in order to tweak the performance. At the same time, reducing the cobalt content as much as possible is an additional goal, since cobalt is rare and often mined under morally unacceptable conditions. The second common type of cathode materials are olivine phosphates with the base formula $LiFePO_4$.
The cathode has been the limiting part of the battery for a long time. This only changed recently,

with new cathode materials outperforming graphite on the anode side. Nowadays, the limiting factor governing the charging speed are the transport processes in the negative electrode (anode) [8].

As anode material, graphitic carbon has been the overwhelmingly most common choice for a long time. Lithium intercalation into graphite was first reported in the 1970s [30, 31], and the first commercial LIB with a graphite anode was introduced in 1991 [32], after compatibility issues with the electrolyte had been solved. As a material, graphite was and is an obvious choice, as it provides a number of desirable qualities in its decent energy- and power-density, high lithium diffusivity and electrical conductivity, as well as low volume change during charging and discharging, while at the same time being relatively cheap and abundantly available [33]. Specifically, it offers a high theoretical gravimetric capacity of 372 mAh/g [34]. Because of these benefits, and because Li-metal anodes were deemed too dangerous [35], the market share of graphite anodes has been 98% [36] since the mid-1990s, with the remaining 2% being $Li_4Ti_5O_{12}$ (LTO) [37].

In the near- and mid-term future, graphite is expected to remain an essential component of commercial lithium-ion batteries – either as sole anode active material or in combination with high-capacity compounds such as understoichiometric silicon oxide, silicon–metal alloys, or elemental silicon [32]. This has been stated by BEV manufacturers [38], material suppliers [39] and cell producers [40] alike, justifying the continuing pursuit of better understanding of this material.

6 Lithium Intercalated Graphite - the Devil in the Detail

The concept of storing lithium ions in a layered graphite structure may seem simple at first glance, but upon closer inspection, it turns out that it is anything but. In this chapter, we give a detailed overview over the numerous complexities that surface - both on the microscopic and the macroscopic scale - during the study of this system, and that all need to be taken into account when validating the performance of a model with the purpose of describing it physically.

6.1 Geometric Properties – Micro-Structure

The local atomic structure of graphite consists of carbon atoms oriented in hexagonal, flat graphene-planes. Each atom forms covalent bonds with its three next neighbours, leaving one valence electron to be delocalized and free to move and transport charge along the plane. This is a fundamentally different bonding situation than in diamond, where all four valence electrons of the carbon atoms are bound in covalent bonds, which is why diamond is an insulator, but graphite is not. The graphene sheets are weakly bonded by van der Waals (vdW) interactions and are stacked in an AB-pattern (see fig. 2), which transforms into an AA-pattern during intercalation with lithium ions, at an SOC of roughly 10% [41–43].

The cell dimensions of empty graphite have been measured experimentally to high accuracies as early as in the 1970s, with the C-C bond lengths being 1.23Å and the distance between the graphene sheets being 3.36Å [44, 45].
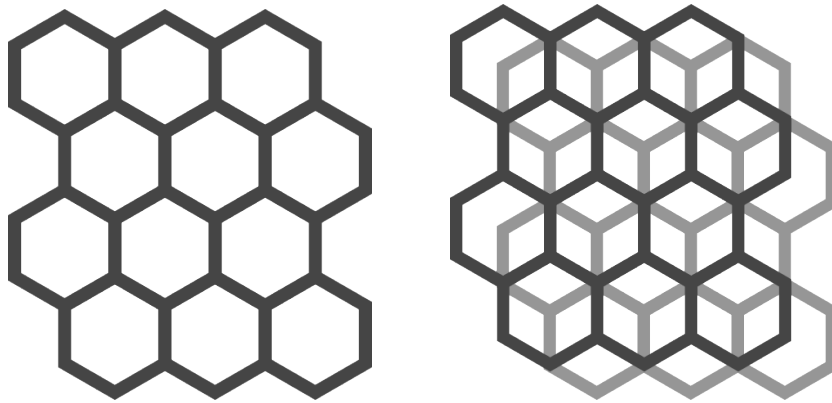
Figure 2: Illustration of the AA- (*left*) and AB-stacking order (*right*) of graphite. Grey hexagons indicate C_6-rings, with the C-atoms implied in the corners.

Intercalation occurs in the way of lithium ions being deposited in the empty areas called "galleries" between the graphene sheets. The lowest energy positions are above (and below) the middle of the C_6-rings, and diffusion between those occurs in a minima-hopping style of movement governed by local diffusion barriers and larger-scale kinetics. At least, this is the case above $\approx 10\%$ SOC, which is when the carbon sheets are AA-stacked. In the AB-stacking case, it is less clear where exactly the Li-ions are ideally located and how their movement can be described.

Under ambient equilibrium conditions, a stoichiometry of LiC_6 - which corresponds to one out of three local minima being occupied - has been considered the maximum SOC (=100%) for

a long time, and we will hold on to that definition within this work. Recently however, some experimental evidence has surfaced for higher states of lithiation also being possible without extreme conditions [46] - these shall be referred to as "over-lithiated". The fundamental difference is the fact that, for those system states, direct next-neighbour positions are permanently occupied by Li-ions, which in turn find themselves in a quasi-metallic chemical environment. In the traditional view, this does not happen, at least not in equilibrium. During super-fast charging processes, the situation may be different. It is conceivable, that if Li-ions are pumped into the anode faster than they can distribute themselves within it, local areas of over-lithiation may be created, which in turn may be responsible for some of the ageing effects, that are observed. However, to our knowledge, there are - as of today - no simulation techniques capable of trying to answer this question on an atomistic level.

Additionally, both defective and amorphous carbon micro-structures play a role in battery materials. The most typical natural defects are 5-rings, 7-rings, and C-atom vacancies. At the same time, purposefully introduced defects (doping) are also being actively researched, in attempts to increase the volumetric capacity [47, 48], cycle stability [49], and to support efficient recycling [50].
The term "amorphous" carbon is typically used to describe anything that is not purely graphite and also not purely diamond, but somewhere in between. One defining property of this type of material is the presence of "nano-pores" of varying sizes and shapes, which exhibit their own unique behaviour during intercalation processes by allowing for the formation of small metal-like clusters of the intercalant, even at lower SOC. These cavities seem to be crucial for enabling the intercalation of larger alkali metals (especially sodium) [51, 52], but less so for lithium, which is small enough to fit between the layers of ordered graphite without causing too much of a volume expansion.

Due to both these phenomena, it is important to not only train a model on ideally ordered, equilibrium structures, but to explore a wider, more diverse feature space.

6.2 Types of Graphite – Macro-Structure

While the term "graphite" is unequivocal on the microscopic scale (except for phenomena like defect densities), it actually describes a number of related but not identical compounds on the macroscopic scale. The closest to what is being studied in typical micro- and meso-scale simulations with perfect, periodic supercells, is a single crystal of highly oriented pyrolytic graphite (HOPG). Large single crystals can in principle be synthesized for experimental purposes, but this very specific type of graphite is not what is used in most batteries. Instead, various types of graphite powder fulfill the purpose of commercial anodes. By 2020, 39% were made of natural graphite (NG) and 58% were made of synthetic graphite (SG) [53], yet the market share of NG is expected to continue rising, due to the fact that it is less CO_2- and energy-intensive in its production [54]. It can be further classified into flake graphite (FG) and micro-crystalline graphite (MG), depending on the size and shape of its grains. In general, one can summarize

that graphite powder with larger anisotropic crystalline domains like FG has better volumetric capacity, while a larger fraction of edge-planes (like in SG) causes better cycle stability and kinetics [55, 56].

In current commercial LIBs, the desired particle shape (see fig. 3), which optimizes said compromise for the applications of interest, is more or less round ("potato-shape") and of a size of $8-30\,\mu$m [32]. For NG, this shape is achieved by mechanical "spheroidization" during or after the mining process [57]. For further enhancement of stability and performance in battery applications, these particles are often coated in amorphous carbon [58].
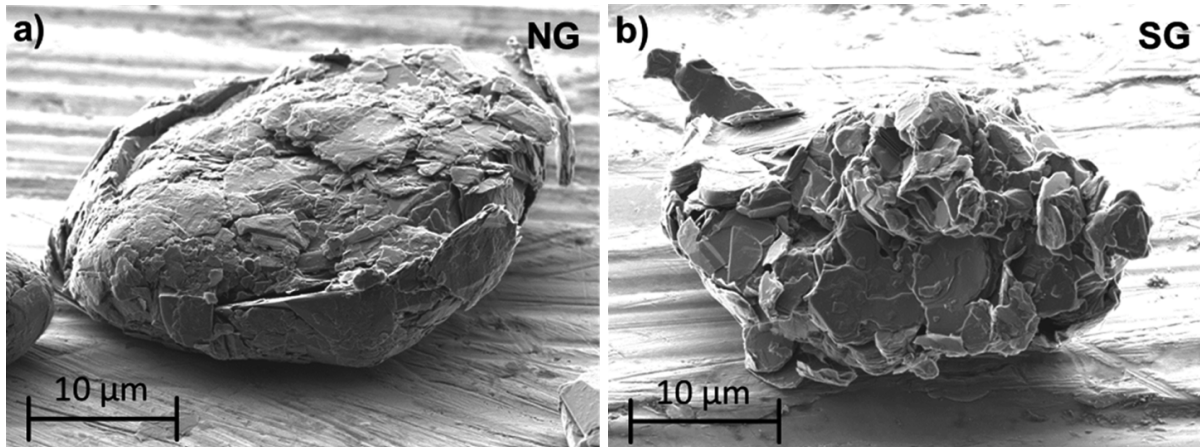

Figure 3: scanning electron microscope (SEM) images [32] of processed natural graphite (a) and synthesized graphite (b) particles, as used in commercial LIBs

For these reasons, it is obvious that purely micro-scale theoretical studies cannot be directly compared with experimental results and real-life anodes, without also taking into account factors like boundary effects, average grain sizes and orientation. Furthermore, the behaviour of lithium ions *between* grains - not only within them - is crucial for accurately simulating the functionality of full anodes within actual batteries. All of this further illustrates the need for an extensive multi-scale model, that can bridge the huge differences in length scales of all the relevant effects.

6.3 Staging and Domains

During the (de-)intercalation of lithium into a uniform area of a graphite crystal, it is energetically more favourable for the intercalant ions to populate as few galleries as possible (at that given SOC), as opposed to filling the whole structure up evenly. This concept was proposed as early as in 1938 by Rüdorff and Hofmann [59]. Specifically, stage I corresponds to each layer being filled, stage II to each second layer and so on. Additionally, an "L" added to the stage stands for "dilute" configurations with the populated layers being filled only partially, at less than their maximum capacity. Based on these, one can explain the sequence of stage-transitions observed in the open circuit voltage (OCV) curve of a (dis-)charging process of a graphite anode (see fig. 4).
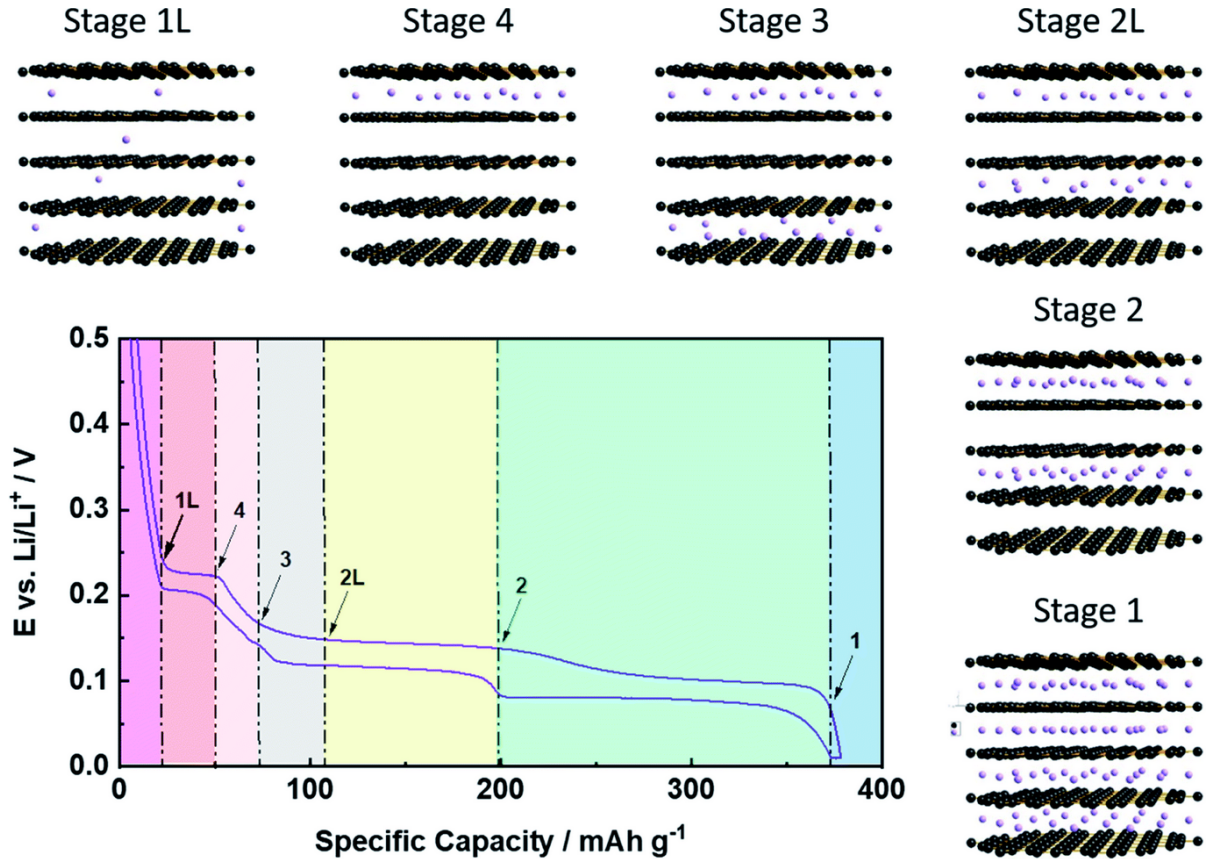
Figure 4: Illustration of the different stages of Li-graphite intercalation compounds (GICs), where they occur during the charging (lower curve) and discharging (upper curve) processes and what kinds of phase transitions can be observed when transitioning between them [32].

From an energetical point of view, there are two basic requirements which a model needs to fulfil, in order to correctly reproduce this OCV curve. Firstly, for any given SOC, the model needs to assign the lowest potential energy to the "correct" ordering of charge carriers at that stoichiometry, which in the ideal equilibrium case should be the one with the most pronounced staging behaviour, or at least close to it. Secondly, the model has to predict correct formation energies (in this case one may equivalently use the term intercalation energies) for the previously identified configurations, which are most favourable. Even these basic requirements by themselves are anything but trivial to fulfil, which becomes obvious when examining the vastly different formation energies predicted by different state-of-the-art DFT functionals [60]. This is mostly due to the difficulties vdW interactions still pose for even the most advanced DFT approaches. Staged compounds are at least partially favoured due to the smaller volume expansion they experience in z-direction, compared with their dilutely ordered counterparts at the same SOC [61], which is one of the central effects causing the stage transitions in the first place – and to a large degree governed by vdW interactions. In fact, Persson et al. claim that the stage transition at 50% SOC can only be captured at all, with dispersion accounted for by the model [62].

Once moving on from static, ideal conditions and actually looking at a full (dis-)charging process, the staging picture by Rüdorff and Hofmann poses problems regarding the exact mech-

anism of the previously mentioned phase-transitions. For example, in order to transition from stage III to stage II, an entire gallery would have to be depopulated, and two others populated instead. Diffusion *through* the graphene sheets is prohibited by a far too high energy barrier to be the explanation, while the possible path out of the particle and around the grain boundary would be very unfavourable from a kinetic point of view.

The solution was first put forward by Daumas and Herold in 1969 [63], in a proposed "domain-model", with the core premise that the previously described stage-ordering is localized within so-called domains - areas within the crystal of more or less arbitrary size (see fig. 5). In this picture, transitions between the phases can be realized simply by moving groups of Li-ions horizontally, within the gallery in which they are already located.
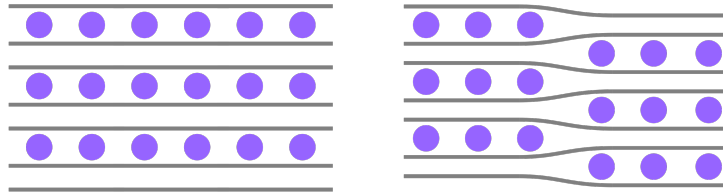

Figure 5: Illustration of a lithium GIC in a globally uniform stage II ordering (*left*) and in a stage II ordering according to the domain model (*right*). The latter circumvents the presence of globally full and empty galleries, enabling kinetically plausible transition paths between the stages.

For the bulk of the theoretical groundwork, which originally validated the hypothesis by Daumas and Herold in the early 1980s, we refer to Safran and Hamann [64–66], Hawrylak and Subbaswamy [67], as well as Kirczenow [68–70] and Axdal [71]. Experimental validation came much later, among others by Wang [72] and Dimiev [73] in the early 2010s, but nowadays, the general hypothesis of the Daumas-Herold domain model has widely been accepted. However, quantitative details, like the domain-size and dependencies thereof, as well as the underlying mechanisms on an atomistic level, have not yet been understood to a satisfactory degree. Even 50 years after first being proposed, the formation, stability and movement of domains are still being investigated in the present, both by theory [74, 75] and by experiment [56, 76].

One exemplary study we want to highlight here for informative purposes was presented by Krishan *et al.* in 2013. They studied the stability of compounds in stages II and III by means of kinetic Monte Carlo (kMC) simulations and DFT (using the Perdew–Burke-Ernzerhof (PBE) functional and a dispersion correction scheme called dispersion corrected atom centered pseudopotential (DCACP) [77]) in order to predict vdW forces between the graphite layers. Based on this approach, they were able to simulate a phase transition from stage III to stage II (see fig. 6) and to reproduce experimental results by Wang *et al.* from 2011 [72] – more specifically the observation that stage-ordering is the most pronounced close to the interface with the electrolyte. Furthermore, their kMC simulations (based on fixed diffusion barriers from [78]) show that even after a time span of the order of microseconds, lithium concentration gradients remain intact, thus further stressing the necessity of treating intercalation mechanisms as non-equilibrium phenomena.
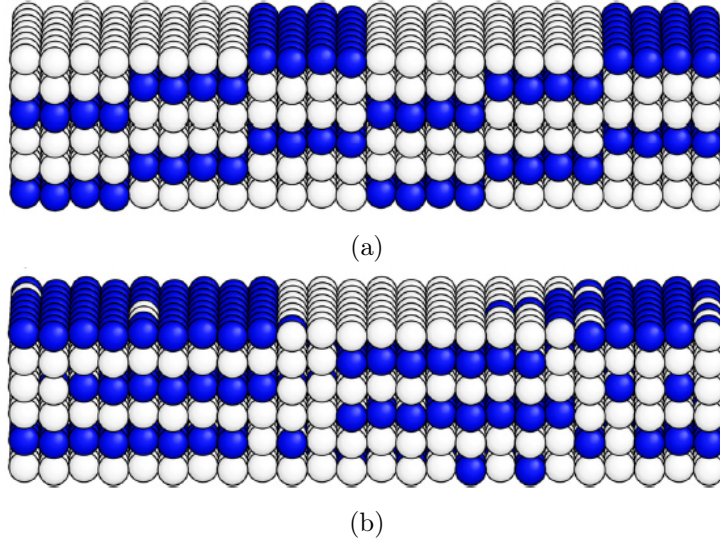
Figure 6: Simulated (by means of kMC) phase transition from an initial stage III compound (a) to one that is partially transformed to stage II (b) by Krishnan *et al.* [74]. Blue spheres signify lithium ions, white spheres vacancies, graphene sheets separating the galleries are implied. A particle bath on the left coupled via an interface to the compound is the driving force behind the stage transition, as would be the case at the interface between electrolyte and anode in a lithium ion battery.

However, despite these successes, the study was still strongly limited by the lack of a true multiscale approach. Diffusion barriers are fixed (an approximation in and of itself), which also means only small changes in the SOC can be investigated at a time. In order to simulate full charging and discharging cycles, a framework is necessary, that can compute diffusion-barriers on the fly, depending on the semi-local environment of the respective Li-ion. Furthermore, in order to investigate the stability of domains the size actually reported from experiment, much larger supercells are necessary.

An additional complication to keep in mind when investigating intercalation is the fact that - since only every third C_6-ring is occupied at 100% SOC - intercalated layers can assume AaAa stacking or AaAb stacking, the first one denoting configurations where the occupied Li-ion positions are directly above each other, and the second one configurations where they are not, but shifted to an adjacent C_6-ring. One can also define an AaAc-stacking, but this is symmetrically equivalent to AaAb and amounts to the same local chemical environment, with the main distributing feature being the presence or absence of Li-ion pairs on the positions above and below the same C_6-ring (see fig 7).
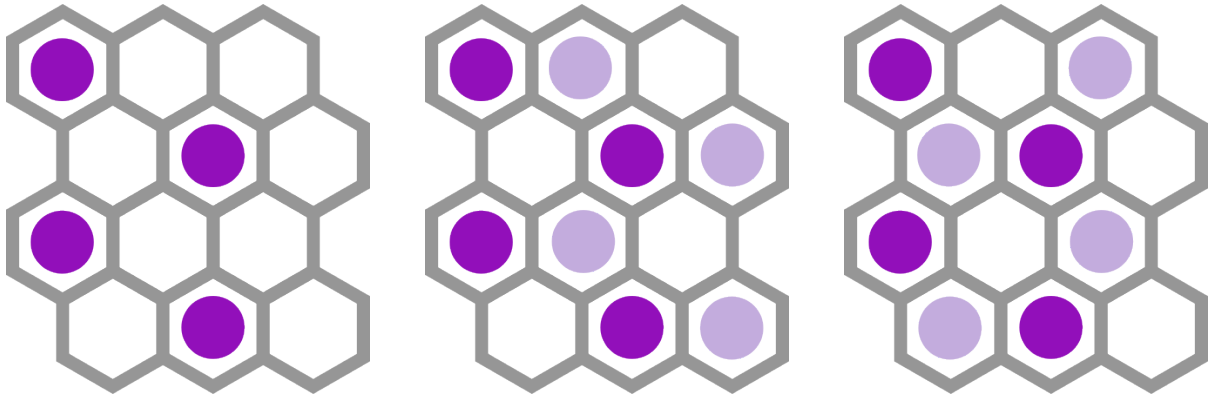
Figure 7: Two layers of lithium intercalated graphite at a stoichiometry of LiC_6, which corresponds to an SOC of 100%, in an AaAa- (*left*), AaAb- (*middle*), and AaAc-stacking (*right*), the latter two of which are symmetrically equivalent. Dark purple spheres correspond to Li-ions above the indicated carbon sheet, light purple spheres to Li-ions below it.

One could in principle go into even more detail and investigate stacking orders like AaAbAc, but the total energy differences between all those configurations are within kT at ambient conditions [79] and only AaAa may stand out as sufficiently distinct from the others to have any noticeable effect on kinetics and/or energetics. Whether this is actually the case is still an open question and has to our knowledge not been answered experimentally, but there is still relevance for our work at least to the degree that we demand of our DFTB parametrization to predict comparable energy differences between AaAa and AaAb/AaAc stacking, as given by the DFT reference method.

6.4 Inter-Layer Distance and Diffusion

The inter-layer distance between the graphene sheets is a property that deserves extra attention for multiple reasons. A central driver of the formation of (locally) staged compounds as opposed to uniform, dilute Li-ion distributions is the fact that the layer distance is slightly expanded (from 3.355Å in the empty state [44, 45] to 3.7Å in the filled state [80]) in areas where there already is a certain density of intercalant ions present, and thus makes these areas more energetically favourable for additional Li-ions to settle in than completely vacant and therefore tighter parts of the galleries. This effect is further enhanced by our own finding that the inter-layer distance does not increase linearly with the percentage of filling within a gallery [79] - in fact our DFTB-structure-relaxations predict that a filling precentage of 33% leads to an expansion of 52% of the full expansion at 100% filling, a filling percentage of 66% leads to an expansion of 80%. Because of this, the perfectly staged realization of any intermediate stoichiometry is always the one with the lowest volume expansion.

Furthermore, the local inter-layer distance also has a strong effect on the diffusion barriers of the Li-ion hopping process from one local minimum to the next. Persson *et al.* [78] calculated that even slight deviations in the layer distances ($\approx \pm 10\%$) lead to significant differences in the migration barriers ($\approx +100\%, -70\%$), especially for dilute, lower saturation stages. Similar (yet

13

not quite as pronounced) effects have also been reported by Xu *et al.* [81], as well. Consequently, any attempt of predicting accurate diffusion barriers is tied to the ability to calculate *very* accurate inter-layer distances.

Diffusion barriers for next-neighbour hopping are one of the defining properties (kinetics being the other one) of the overall diffusive behaviour within the system, a property that is still rather poorly understood. In fact, big discrepancies of macro-scale diffusion coefficients $(10^{-6} - 10^{-14} \frac{cm^2}{s})$ have been reported in experimental literature [78]. These can be attributed to a number of phenomena, like domain formation and sizes, grain boundary effects due to differing structural types of graphite powder (see section 6.2 for details), and more, but accurate inter-layer distances (and diffusion barriers) are a necessary foundation for ever making sense of these discrepancies with any theoretical approach.

Beyond that, diffusion barriers are also a fundamental building block of kMC simulations, which are one of the most promising approaches for linking atomistic processes with macro-scale properties [75, 82, 83]. In the past, it was necessary to make severe approximations - Krishnan *et al.* [74] assumed one fixed barrier height regardless of the semi-local environment of each respective Li-ion, and had decent success with that for short-timed investigations of domain formation, but such an approach would likely break down when attempting to simulate larger portions of (and eventually full) charging and discharging cycles.

Unfortunately, despite a lot of interest, the inter-layer distances (which are mostly governed by weak vdW interactions) in layered materials like lithium GICs are still notoriously difficult to capture properly, even with state-of-the-art DFT functionals and dispersion corrections [60]. This is already the case just for empty graphite, let alone the entire range of charge.

6.5 Summary

In summary, we strive to create a model which fulfils a rather long list of requirements. We summarize those, together with the main contributors responsible for capturing these properties well, in the following table:

Requirement	Main Contributor
Be sufficiently affordable to calculate systems large enough to capture realistic domain-sizes and low SOC	Method choice (DFTB)
Correctly capture the increase in C-C bond lenghts with SOC	Repulsion potential
Relax supercells to the correct inter-layer distances for the entire range of SOC	vdW correction
Energetically favour staged over dilute configurations	Electronic part
Favour AB-stacking in empty graphite, but AA-stacking above around 10% SOC	Electronic part
Output correct formation energies (at least compared to the reference DFT method of choice)	Electronic part & Repulsion potential
Predict correct atomic forces when moving Li-ions out of local minimum positions	Repulsion potential & Training data
Capture the correct bulk modulus for slight bending of the graphene sheets	Repulsion potential
Be prepared to encounter the event of over-lithiation. (Corresponding to correctly describing Li-ion pairs on direct next neighbour positions)	Training data
Deliver a satisfactory description of Li-metal	Training data

7 Theoretical Methods - Constructing the Multiscale Model

At the foundation of a large portion of elementary quantum chemistry lies the time-independent, non-relativistic Schrödinger equation 1 – in this formulation for a system consisting of M nuclei with N electrons, in the particular system state i, with $\hat{H}$ the Hamilton operator, and in absence of any magnetic or electric fields:

$$\hat{H}\Psi_i(\vec{x}_1, ..., \vec{x}_N, \vec{R}_1, ..., \vec{R}_M) = E_i\Psi_i(\vec{x}_1, ..., \vec{x}_N, \vec{R}_1, ..., \vec{R}_M) \ . \tag{1}$$

For any particular state of any chemical system, all information can be described by means of its wave function Ψ [84], which depends on the $3N$ spatial coordinates and the N spin coordinates of the electrons - both collected in $\vec{x}$ - as well as the $3M$ spatial coordinates of the nuclei $\vec{R}$. For a general many-body system, the Hamiltonian consists of the kinetic energies of the nuclei and the electrons ($\hat{T}_e$ and $\hat{T}_n$), as well as the interactions between pairs of electrons ($\hat{V}_{ee}$), nuclei ($\hat{V}_{nn}$) and mixed pairs ($\hat{V}_{en}$). However, within the realm of validity of the Born-Oppenheimer approximation, the slow-moving nuclei can be considered stationary within the time-frames of electron movement. Thus, $\hat{T}_n$ is approximated as 0, and $\hat{V}_{nn}$ is viewed as constant, leading to the non-relativistic form of the Hamiltonian:

$$\hat{H} = \hat{T}_e + \hat{V}_{ee} + \hat{V}_{en} + C \ . \tag{2}$$

The central challenge of many quantum chemical methods is the evaluation of said equation, an endeavour that - with increasing system size - quickly becomes impossible in analytical fashion due to the $4N$ scaling with the number of electrons. Therefore, a multitude of approximations and there-on based approaches have been developed - at vastly different regions of the accuracy vs. cost compromise. On the one end of the spectrum, wave function methods like coupled cluster (CC) theory [85] are highly accurate, yet hardly able to treat systems with more than a handful of atoms at a time, while on the other end, fully empirical atomistic force field (FF) approaches [86] are capable of calculating millions of atoms to somewhat reasonable accuracy, but lack any kind of physical information within the model.

Whenever multiple levels of theory are combined, in order to make up for each others weaknesses, one speaks of "multiscale modeling". As of now, it is not possible to create a link between atomic processes and macroscopic properties of solid materials by means of just one theoretical approach. Instead, it is common practice to construct a hierarchy of methods, each of them validated against more accurate calculations for relatively small systems, and then in turn used to validate the next, cheaper, approach against systems at the high end of their own computational capabilities. Figure 8 shows a summary of approaches commonly used in such a fashion.
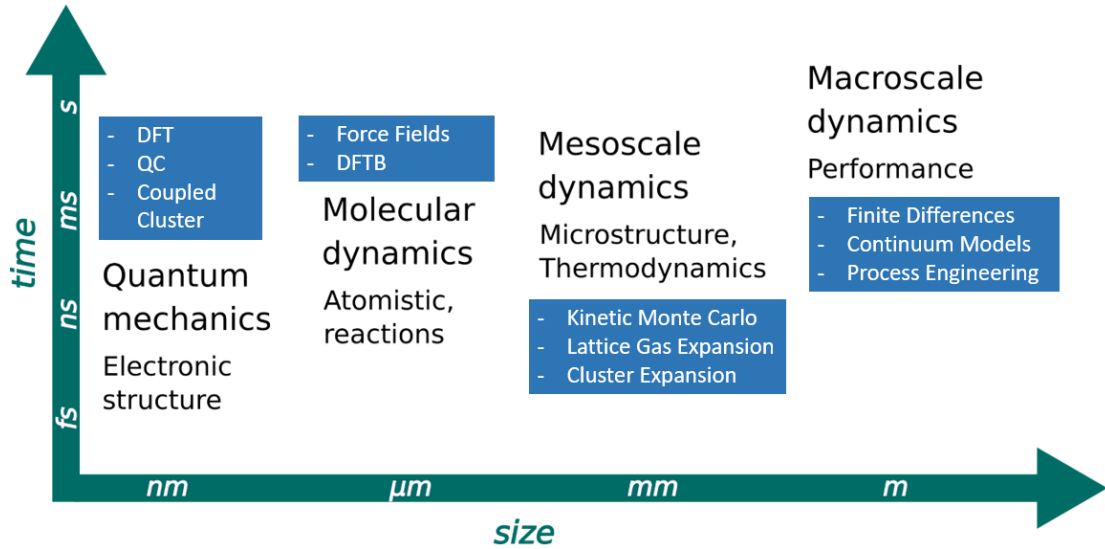
Figure 8: Illustration of the different length- and time-scales, as well as modeling techniques relevant to materials design and research.

Within this chapter, we give detailed introductions to the methods used in this work and describe the way we used them to construct our own multi-scale model for lithium GICs.

7.1   Density Functional Theory

DFT has been one of the most prominent work-horses of electronic structure calculations for the last multiple decades, with a vast variety of implementations and flavours available today. The foundation of all these methods is the idea that, instead of the wave-function, the electron density of a system can be used to calculate the energy. This property is significantly less complex, since it does not depend on the exact positions of the electrons (and spin thereof), but solely on their spatial distribution. It is also *real* and can in principle be measured.

The point of origin for the derivation of DFT is the total energy of a quantum mechanical system, as formulated by Kohn and Sham [87] (see equation 3), which expresses the total energy as a functional of the electron density $n(\vec{r})$, as well as the atomic positions $\vec{R}$:

$$E_{\mathrm{KS}}[n(\vec{r}), \vec{R}] = E_{\mathrm{kin}} + E_{\mathrm{ext}} + E_{\mathrm{Hartree}} + E_{\mathrm{II}} + E_{\mathrm{XC}} , \tag{3}$$

where E_{kin} is the non-interacting part of the kinetic electron energy, E_{ext} the interaction between all electrons and nuclei, as well as ions (if any are present), E_{Hartree} the classical Coulombic ground state energy, E_{II} the electrostatic potential between nuclei and ions and E_{XC} the so-called exchange-correlation energy. The first four of these contributions are well-defined and can in principle be calculated to an arbitrary accuracy. However, this is not the case for the final contribution (equation 4), which includes the non-classical many-body effects not covered by the other terms in the expression:

$$E_{\text{XC}} = E_{ee} - E_{\text{kin}} - E_{\text{Hartree}} \,. \tag{4}$$

According to the foundational theorem by Hohenberg and Kohn [88], only the exact ground state electron density results in the minimum total energy. Based on this, it is in principle possible to approach the ground state density and minimum energy by some variational minimization scheme, from an initial density guess – given that the Kohn-Sham energy functional is known. However, this is not quite the case, so the conundrum at the heart of every DFT-method is approximating the exchange-correlation functional E_{XC} as well as possible, while also remaining computationally affordable.

Available functionals differ vastly in complexity and methodology of the derivation. The simple, but comparatively fast local density approximation (LDA) ([89]) – only taking into account local values of the density – was introduced as early as 1980 and was the first truly productive version of DFT. Later, the class of general gradient approximation (GGA) functionals came to life in the late 90s, being based also on the local gradient of density. One famous example is the functional by Perdew, Burke and Ernzerhof (PBE) [90–92] – probably the most-used to date and the backbone of countless studies.

Further improvements upon certain shortcomings in the performance of GGAs have been attempted in many different ways [93]. Hybrid functionals for instance mix the approximate exchange functional with a certain fraction of exact exchange, and are still being actively researched to this day [94–97]. However, even these modern functionals are still local in nature. Therefore, none of them are capable of describing long ranged dispersion effects (not even qualitatively).

7.1.1 Van der Waals Corrections

Dispersion effects like vdW interactions have been one of the biggest challenges to DFT for many years [93]. Numerous approaches have been tried, but only in the 2010s, reliable post-corrections surfaced, beginning with the 2-body schemes by Grimme [98, 99], and by Tkatchenko and Scheffler [100]. Soon after, the many-body dispersion (MBD) correction by Tkatchenko was presented [101–105] and has been further improved both in terms of theory and in terms of implementation.

It is obvious, from just looking at the structure of lithium-GICs, that a good dispersion correction model is at least as important as the actual DFT functional, in order to achieve high-quality computations of all relevant system properties. As pointed out previously, the inter-layer distance between two adjacent graphene sheets is of crucial importance for the prediction of accurate Li-ion diffusion barriers – and is governed almost exclusively by dispersive interactions at least for lower SOC. Beyond that, it has been shown by Persson et al. [78] that the stage-transition at 50% SOC is only visible at all in DFT-calculations with vdW-corrections activated. Furthermore, we want to point out that not only the correct positions of the minima of the "potential energy vs. layer-distance" relationship are important, but also the related bulk modulus, i.e. how much any given non-minimum layer distance is punished energetically compared with the minimum. This is relevant on the one hand, since due to the local nature of the stage-domains, there are interfaces where the actual local layer-distance differs from the one that would

be expected in a perfectly staged compound of the same SOC, and on the other hand in order to correctly estimate the energy differences between different stacking order (AaAa, AaAb,...) in otherwise identical stoichiometries.

Replicating all of these properties correctly with our DFTB-models, relative to the dispersion-corrected DFT reference, has been one of the central challenges during this work.

7.1.2 Applications of DFT in this Work

DFT calculations are the primary reference and training method used in this work for the parametrization of our DFTB model. We selected the PBE functional [90–92] and the MBD dispersion correction [101], because this combination best captured experimentally known structural properties like bond lengths and inter-layer distances at both ends of the SOC-range of Li-GICs. All calculations were performed with the all-electron framework FHI-aims [106], with light settings and default tier-2 basis sets. The k-point grid is well-converged at $8 \times 8 \times 8$ for supercells in the training set, which are all smaller than $8\text{Å} \times 8\text{Å} \times 8\text{Å}$. Relativistic treatment is implemented via the atomic zero-order regular approximation (ZORA). Convergence criteria for the self-consistent cycle have not been changed from the default settings, as suggested in [106].

7.2 Density Functional Tight Binding

Semi-empirical electronic structure models have successfully played the niche role of capturing non-local quantum mechanical effects that cannot be properly described by fully empirical atomic force fields [107], which have otherwise been on the forefront of modern materials modeling - and especially successful for covalent or metallic systems [108–110]. To fill this niche, a wide variety of semi-empirical quantum chemistry approaches have been developed [111–117]. The most common among these is DFTB, which was first developed by Elstner, Porezag *et al.* [118, 119] in the late 1990s, building upon ideas by Harris and Foulkes [120, 121] from the late 1980s, and modernized into its state-of-the-art, self-consistent form by Oliveira *et. al* [122] in 2009. It introduces additional tight-binding approximations to the theoretical DFT framework, which in practice amount to not calculating the entire energy expression from scratch for each iteration. Instead, certain elements are obtained by interpolating pre-computed tables and parametrized potentials. The benefit of this is a speed-up of around 2-3 orders of magnitude compared to traditional (GGA-)DFT, which places DFTB at roughly the same cost as charge adaptive force fields like reaxFF [123] (which is 20 years old but still being heavily used and improved upon [124–126]). However, as opposed to atomistic FF methods, DFTB also has the advantage of providing full access to electronic structure properties like band structures and densities of states, which can be utilized in the same way as those output by DFT. Obviously, these benefits do not come without a trade-off. This manifests as a compromise between reduced accuracy and transferability, which can be tuned to a degree during the parametrization process, i.e. it is possible to either create very accurate parametrizations which only work for one specific system, or reasonably versatile parametrizations which have to sacrifice a fair bit of accuracy.

In the following sections we show a detailed derivation of the DFTB energy functional (specifically in the formulation implemented in the DFTB+ framework [127, 128]) from the DFT-functional, explain all simplifications and parameters that are introduced, and present the exact procedure of calculating a total energy value from an atomic cell.

7.2.1 The Underlying Energy Functional

The notation in this section is chosen as follows: nuclei are indicated with i, j, particle states as a and basis orbitals as μ, ν. We begin by explicitly writing the Kohn-Sham-energy (see equation 3) that DFT is also based upon:

$$E_{\mathrm{KS}}[n(\vec{r})] = \sum_a f_a \langle \psi_a | \left(\overbrace{-\frac{1}{2}\nabla^2}^{E_{\mathrm{kin}}} + \overbrace{\int V_{\mathrm{ext}}(\vec{r})n(\vec{r})}^{E_{\mathrm{ext}}} \right) |\psi_a\rangle + \overbrace{\frac{1}{2}\int\int' \frac{nn'}{|\vec{r}-\vec{r'}|}}^{E_{\mathrm{Hartree}}} + E_{\mathrm{II}} + E_{\mathrm{XC}} \quad (5)$$

with $f_a \in [0, 2]$ being the occupation of state ψ_a with energy ϵ_a and typically taken from a Fermi distribution. Now, the tight-binding flavour is introduced to the framework by the

assumption that the single-particle wave-functions can be sufficiently described by an orthogonal and minimal basis set (eq. 6), constructed only from the valence orbitals, and thus reducing the dimensionality of the problem greatly.

$$\psi_a = \sum_\mu c_\mu^a \phi_\mu(\vec{r}) \quad \text{with} \quad c_\mu^a = \left\langle \overbrace{\underbrace{\mu}_{\text{basis vectors}}}^{\text{coefficients of the orthogonal basis}} \middle| \psi_a \right\rangle \tag{6}$$

As another approximation, a pseudo-density $n_0(\vec{r})$ is introduced, which consists of the local electron densities around the free, neutral and non-interacting atoms within the system. In order to assure the latter of those qualities, a confinement potential is applied, which cuts off the diffuse tails of the simplified wave-function orbitals [129]. Determining the exact shape of this potential is part of the parametrization process and will be explained in section 7.2.6. The assumption made at this stage of the derivation is that this pseudo-density is reasonably similar to the true electron density of the structure and will therefore produce a similar system energy, when the (simplified) Kohn-Sham energy functional is applied to it:

$$n_{\text{true}}(\vec{r}) = n_0(\vec{r}) + \delta n(\vec{r}) \quad \text{with} \quad \delta n(\vec{r}) << n_0(\vec{r}) \ . \tag{7}$$

As a consequence, the total system energy can be Taylor-expanded around the pseudo-density of the non-interacting system $n_0(\vec{r})$ by a small deviation $\delta n(\vec{r})$. Interactions and correlations are treated in a perturbative manner [129]. In the earliest versions of DFTB, this expansion was truncated after terms of order zero (DFTB0) [130]. This worked well for mostly covalent systems, but not when any significant amount of charge transfer was present in the system. Today, it is most common to truncate the Taylor expansion after terms of the second order. This approach is called self-consistent charge (SCC) DFTB and was first proposed by Elstner *et al.* in 1998 [131]. It results in the following expression:

$$E[\delta n] \approx \sum_a f_a \langle \psi_a| \overbrace{-\frac{1}{2}\nabla^2 + V_{\text{ext}} + V_H[n_0(\vec{r})] + V_{\text{XC}}[n_0(\vec{r})]}^{H(n_0), \text{ no charge transfer}} |\psi_a\rangle \tag{8}$$

$$+ \frac{1}{2} \int \int' \left(\frac{\delta^2 E_{\text{XC}}[n_0(\vec{r})]}{\delta n \delta n'} + \frac{1}{\vec{r} + \vec{r'}} \right) \delta n \delta n' \tag{9}$$

$$- \frac{1}{2} \int (V_{\text{Hartree}}[n_0(\vec{r})]n_0(\vec{r}) + E_{\text{XC}}[n_0(\vec{r})] + E_{\text{II}})\delta n - \int (V_{\text{XC}}[n_0(\vec{r})]n_0(\vec{r}))\delta n \tag{10}$$

The first (0-order) term was named "band-structure energy" (E_{BS}) and amounts to the total self-energy of the non-interacting pseudo-system we introduced before, thus consisting of a sum of single-atom contributions. Due to the minimal basis set introduced in the first approximation,

these contributions consider only valence-electrons.

The 1st-order term in the second line is called "Coulomb energy" (E_{Coul}) and describes the electrostatic interactions between local charge densities caused by the varying electronegativities of the different species in the system, as well as some coupling effects between mobile charge fluctuations.

The term in the third line is called "repulsion energy" (E_{rep}) and is similar in spirit to the exchange-correlation energy in DFT, as it contains everything that could not be captured by the other terms: non-classical many-body effects, core effects and – in principle – all errors caused by the approximations introduced previously – at least relative to the DFT reference.

7.2.2 The Band-Structure Energy

The first and simplest part of the DFTB energy is the total self-energy of the non-interacting pseudo-system we introduced before. It straightforwardly amounts to the sum of the atomic contributions:

$$E_{\text{BS}}(\delta n) = \sum_a f_a \langle \psi_a | H(n_0) | \psi_a \rangle \ . \tag{11}$$

With the minimal basis set (eq. 6) applied, this becomes:

$$E_{\text{BS}}(\delta n) = \sum_a f_a \sum_{\mu\nu} c_\mu^a c_\nu^a \underbrace{\langle \phi_\mu | H^0 | \phi_\nu \rangle}_{\text{neutral−charge Hamiltonian } H_{\mu\nu}^0} \ . \tag{12}$$

Note that so far, the basis coefficients c_μ^a have yet to be specifically defined. This is done by means of a variational principle, as explained in chapter 7.2.5.

7.2.3 The Coulomb Energy and Atomic Charge Populations

The second contribution to the DFTB energy is the Coulomb term E_{Coul}. Before attempting to describe this as a function of the electron density, it is helpful to first examine it as a function of a partial atomic point charge Δq, as put forward by Parr *et al.* [132]:

$$E(\Delta q) \approx E_0 + \left(\frac{\delta E}{\delta \, \Delta q} \right) \Delta q + \frac{1}{2} \left(\frac{\delta^2 E}{\delta \, \Delta q^2} \right) \Delta q^2 \tag{13}$$

$$= E_0 - \chi \Delta q + \frac{1}{2} U \Delta q^2 \tag{14}$$

$$\text{with} \ \ \chi = \frac{1}{2}(IE + EA) \ \ = \ \ \text{neg. slope of } \Delta E \tag{15}$$

$$\text{and} \ \ U = IE - EA \ \ \ \ \ \ = \ \ \text{curvature of } \Delta E \tag{16}$$

χ is the electric susceptibility, which describes the degree of polarization induced as a response to an external electric field. U is the "Hubbard parameter" – two times the electronic hardness – and can intuitively be understood as the shape-wise reaction of the local electron-density to additional charge. Both these properties (for the free atom) can be calculated from the ionization energy IE (energy necessary to negatively ionize the neutral atom) and the electron affinity EA (energy needed to remove a second electron from the 1-anion) as shown in equations (15) and (16).

With this in mind, we can now specifically examine the Coulomb energy term in the DFTB framework:

$$E_{\mathrm{Coul}}[\delta n] = \frac{1}{2} \int \int' \left(\frac{\delta^2 E_{\mathrm{XC}}[n_0(\vec{r})]}{\delta n \delta n'} + \frac{1}{|\vec{r} - \vec{r'}|} \right) \delta n \delta n' \; . \tag{17}$$

In a first simplification, the total space integral is reformulated as a sum of integrals over areas V_i around the atomic positions of atom i:

$$\int_V = \sum_i \int_{V_i} \; . \tag{18}$$

At this stage, a distinction between the one-body $(i = j)$ and the two-body $(i \neq j)$ cases is necessary. For the first of the two, eq. 17 can be written as:

$$E_{\mathrm{Coul}_{i=j}}[\delta n] = \frac{1}{2} \Delta q_i^2 \underbrace{\sum_i \sum_i{}' \int_{V_i} \int_{V_i}' \left(\frac{\delta^2 E_{\mathrm{XC}}[n_0(\vec{r})]}{\delta n \delta n'} + \frac{1}{|\vec{r} - \vec{r'}|} \right) \delta n \delta n'}_{\approx U_i = IE - EA} \tag{19}$$

By comparing this equation and eq. 14, it becomes apparent that a large part of the expression can be approximated by the Hubbard parameter U.

For the two-body part situation, E_{XC} vanishes, since the exchange correlation functionals are local. With this, equation 17 becomes:

$$E_{\mathrm{Coul}_{i \neq j}}[\delta n] = \frac{1}{2} \sum_i \sum_j \Delta q_i \Delta q_j \int_{V_i} \int_{V_j}' \frac{\delta n_i \delta n_j'}{|\vec{r} - \vec{r'}|} \; . \tag{20}$$

This expression is purely electrostatic. To further unravel it, $\delta n_i(r)$ is approximated as a spherically symmetrical Gaussian:

$$\delta n_i(r) \approx \exp\left(\frac{-r^2}{2\sigma_i^2}\right) \quad \text{with} \quad \sigma = \frac{\text{FWHM}}{\sqrt{8ln2}} \ . \tag{21}$$

FWHM – the full width at half maximum – is derived by fitting the Gaussian to a reference charge density as a function of the distance plot, which is usually calculated in DFT. By comparing this with the one-body case, the following is derived:

$$\text{FWHM}_i = \sqrt{\frac{8ln2}{\pi} \frac{1}{U_i}} = \frac{1.329}{U_i} \ . \tag{22}$$

Applying this, and after further analytical simplifications, the Coulomb energy in the two-body case can be written as:

$$E_{\text{Coul}_{i \neq j}}(\delta n) = \frac{1}{2} \sum_i \sum_j \Delta q_i \Delta q_j \frac{erf(C_{ij}R_{ij})}{R_{ij}} \tag{23}$$

$$\text{with} \quad C_{ij} = \sqrt{\frac{4ln2}{(\frac{1.329}{U_i})^2 + (\frac{1.329}{U_j})^2}} \ . \tag{24}$$

Putting both cases together results in the following expression for the full Coulomb energy:

$$E_{\text{Coul}} = \frac{1}{2} \sum_{ij} \gamma_{ij}(R_{ij}) \Delta q_i \Delta q_j \tag{25}$$

$$\text{with} \quad \gamma_{ij} = U_i \qquad\qquad \text{for} \quad i = j$$
$$\text{and} \quad \gamma_{ij} = \frac{erf(C(U_i, U_j)R_{ij})}{R_{ij}} \quad \text{for} \quad i \neq j$$

There are only two quantities this expression is dependent on: the Hubbard parameter U is usually available in literature for most elements, or can be calculated by means of DFT. However, if there is significant charge transfer present in the system of interest and the chemical environments of the atoms differ more strongly from the free atom state, the choice can also be made to treat U as an adaptable parameter, that is varied within reasonable boundaries during the parametrization process for a better description of the system (but again most likely at the cost of transferability).

The second necessary input for the computation of the Coulomb energy are the local charge populations $\Delta q_{i,j}$ at each atomic position. In order to treat these explicitly, Mulliken charge analysis [133, 134] is employed. The first step is writing down the number of electrons located in a volume around one atom i:

$$q_i = \sum_a f_a \int_{V_i} |\psi_a(\vec{r})|^2 d^3\vec{r} \tag{26}$$

Within the approximation of tightly bound electrons, it is sufficient to express the single-particle wave-functions in a minimal orthonormal basis consisting of only atomic valence orbitals:

$$\psi_a = \sum_\mu c_\mu^a \phi_\mu(\vec{r}) \ . \tag{27}$$

With this, eq. 26 can be written as:

$$q_i = \sum_a f_a \sum_{\mu\nu} c_\mu^{\alpha*} c_\nu^\alpha \int_{V_i} \phi_\mu^*(\vec{r})\phi_\nu(\vec{r})d^3\vec{r} \ . \tag{28}$$

There are three possible cases regarding the affinity of the orbitals μ and ν in relation to atom i - both of them, one of them or neither of them belonging to it. Splitting up the integral and treating all three cases explicitly, the equation becomes:

$$q_i = \sum_a f_a \bigg(\sum_{\mu,\nu \in i} c_\mu^{\alpha*} c_\nu^\alpha \int_{V_i} \phi_\mu^*(\vec{r})\phi_\nu(\vec{r})d^3\vec{r} \tag{29}$$

$$+ \sum_{\mu \in i, \nu \in j \neq i} c_\mu^{\alpha*} c_\nu^\alpha \int_{V_i} \phi_\mu^*(\vec{r})\phi_\nu(\vec{r})d^3\vec{r} \tag{30}$$

$$+ \sum_{\mu,\nu \notin i} c_\mu^{\alpha*} c_\nu^\alpha \int_{V_i} \phi_\mu^*(\vec{r})\phi_\nu(\vec{r})d^3\vec{r} \bigg) \tag{31}$$

Within the present approximations, the first term is simply the number of valence electrons in the neutral atom, while the third term vanishes completely due to the confined basis functions. Therefore, the second term amounts to the extra electron population at atom i, which is the negative of the local charge population Δq_i. By recognizing that the orbital overlap is distributed evenly between the volume elements V_i and V_j around atoms i and j (eq. 32), the expression for the charge populations can be further simplified (eq. 33 with *c.c.* for complex conjugate), finally providing a workable form:

$$\int_{V_i} \phi_\mu^*(\vec{r})\phi_\nu(\vec{r})d^3\vec{r} \approx \int_{V_j} \phi_\mu^*(\vec{r})\phi_\nu(\vec{r})d^3\vec{r} \approx \frac{\int_V \phi_\mu^*(\vec{r})\phi_\nu(\vec{r})d^3\vec{r}}{2} \approx \frac{S_{\mu\nu}}{2} \tag{32}$$

$$\Delta q_i = -\frac{1}{2} \sum_a f_a \sum_{\mu \in i} \sum_{\nu \in j \neq i} (c_\mu^{a*} c_\nu^a + c.c.) \underbrace{S_{\mu\nu}}_{\text{overlap matrix elements}} \tag{33}$$

The requirements for calculating the charge populations are the expansion coefficients $c_{\mu,\nu}^a$ of

the basis set and the corresponding element of the orbital overlap matrix $S_{\mu\nu}$.

7.2.4 The Repulsion Energy

Finally, the repulsion energy needs to be considered - the most obscure of the three contributions. It consists of a variety of many-body contributions (with unknown shape), core effects and double counting corrections (eq. 34). Similar in spirit to the exchange-correlation energy in DFT, it is essentially the difference between the reference energy of the training method and the previously discussed contributions to the DFTB energy:

$$E_{\text{rep}} = -\frac{1}{2} \int V_{\text{Hartree}}(n_0(\vec{r}))n_0(\vec{r}) + E_{\text{XC}}(n_0(\vec{r})) + E_{\text{II}} - \int V_{\text{XC}}(n_0(\vec{r}))n_0(\vec{r}) \ . \qquad (34)$$

In the context of traditional DFTB, it is constructed as a sum of spherically symmetric, pairwise repulsive two-body potentials as in eq. 35 (although other ways of describing it are also possible):

$$E_{\text{rep}} \approx \sum_{ij} V_{\text{rep}}^{ij}(R_{ij}) \ . \qquad (35)$$

Of course, assuming that such a simple form is able to capture the nuances of a superposition of many-body effects is a drastic approximation, but has worked surprisingly well for many chemical systems [9, 135, 136] in the past. This may be due to the fact that these many-body effects are usually small compared with their two-body counterparts, and also compared with the other approximations made during the derivation of the method. However, with the recent developments in machine-learned many-body atomic potentials like ACE/PACE ([15–17]) and previously GAP ([12–14]), using such an approach for the repulsion energy, in combination with a traditional DFTB electronic part, is expected to be a promising pathway towards further improving both methods. The recent addition of Chebyshev interaction model for efficient simulation (ChIMES) [137–139] to the DFTB+ framework is already a first step in this direction.

Whichever specific formulation is chosen, the repulsion energy is typically obtained by fitting to a DFT reference or other higher level theory and experimental properties, as described in section 7.2.7.

7.2.5 The Full Energy Expression and the Requirements for its Calculation

With all three contributions in place, the full energy expression can be written as:

$$E = \sum_a f_a \sum_{\mu\nu} c_\mu^{a*} c_\nu^a H_{\mu\nu}^0 + \frac{1}{2} \sum_{ij} \gamma_{ij}(U_{ij}, R_{ij})\Delta q_i \Delta q_j + \sum_{i<j} V_{\text{rep}}^{ij}(R_{ij}) \ . \qquad (36)$$

From this (and equation 33), it is apparent that there are four objects which need to be

calculated: the orbitals ϕ (as they appear in $H^0_{\mu\nu} = \langle\phi_\mu|H^0|\phi_\nu\rangle$ and in $S_{\mu\nu} = \langle\phi_\mu|\phi_\nu\rangle$), the neutral-charge Hamiltonian matrix H^0, the overlap matrix S (which is part of the expression for the charge populations $\Delta q_{i,j}$) and the basis set expansion coefficients $c^a_{\mu,\nu}$.

The orbitals ϕ are obtained by applying a confinement potential to the free atom orbitals, effectively cutting off the diffuse tails. See section 7.2.6 for a detailed explanation.

For the neutral Hamiltonian H^0, the entries in the case $\mu, \nu \notin i$ vanish due to the localized nature of the orbitals. In terms of the diagonal entries $\mu = \nu \in i$, there are a two options of how to proceed. The simple one is to approximate them by the valence energies of free, neutral atoms, which can be pre-calculated e.g. by means of DFT, or taken from literature. Alternatively, they can also be considered parameters during the electronic part parametrization process, which may increase the performance. Finally, the off-diagonal entries $\mu \in i, \nu \notin i$ are (in either case) pre-computed based on Slater-Koster transformations in a two-centre approximation, as in $H^0_{\mu\nu} = \langle\phi_\mu|H^0|\phi_\nu\rangle$.

The overlap matrix elements are calculated analogously (applying one- and two-body approximations) from the orbitals:

$$S_{\mu\nu} = \langle\phi_\mu|\phi_\nu\rangle \tag{37}$$

The largest part of the speed-up DFTB is able to achieve compared with DFT stems from the fact that the three previously mentioned objects can be pre-calculated in the beginning of a DFTB calculation and do not need to be obtained via a convergence-based variational approach. However, the same is not true for the basis expansion coefficients. Here, a set of secular equations is employed (eq. 38), with l_{lag} being some undetermined Lagrange multipliers.

$$\sum_\nu c^a_\nu(H_{\mu\nu} - l_{lag} \cdot S_{\mu\nu}) = 0 \tag{38}$$

$$\text{with} \quad H_{\mu\nu} = H^0_{\mu\nu} + \frac{1}{2}(\varepsilon_i + \varepsilon_j)S_{\mu\nu} \tag{39}$$

The total Hamiltonian $H_{\mu\nu}$ can be separated into the Hamiltonian of the pseudo system $H^0_{\mu\nu}$ and a contribution of charge fluctuations with $\varepsilon_{i,j}$ being the electrostatic energy of atoms i and j. Due to the fact that the expansion coefficients are needed to calculate the charge populations Δq, which themselves are necessary for the computation of $\varepsilon_{i,j}$ (see equations 25 and 33), a self-consistent, iterative procedure is necessary, starting at e.g. neutral charges and iterating until convergence is reached. This is the reason why second-order DFTB is also called self-consistent charge SCC DFTB.

7.2.6 Electronic Part Parametrization

As described before, the "electronic part" in the SCC-DFTB framework consists of the self-energy of the non-interacting, tightly bound pseudo system and the Coulomb interactions between the

valence electron density, as well as fluctuations thereof. In order to calculate it from an atomic structure, one requires values for the diagonal elements ε of the non-interacting Hamiltonian (also called energy eigenvalues) and the Hubbard parameter U, as well as a defined functional form for the confinement potential, which is responsible for localizing the orbitals. Each of these is unique per species in the system.

The confinement potential is a necessary "parameter", which always needs to be optimized – one for each species – by selecting an appropriate functional form and defining its coefficients. Among the forms that have been used are quadratic [140] and power functions [136], as well as the – in our opinion – slightly superior "Woods-Saxon potential" (see eq. 40), which achieves a smoother transition to zero in the orbital tails without dramatically affecting the core region:

$$V_{\text{conf}} = \frac{W}{1 + \exp(-a(r - r_a))} \; . \tag{40}$$

On the other hand, both ε and U are optionally optimizable parameters. Often, they are simply taken from the free atom. However, depending on the amount of charge transfer occurring in the system, the choice can be made to modify them as well. Either way, the parameter-space is then optimized based on selected criteria, which can be summarized in an appropriate cost function – typically a selection of features from the band structures of the chemical species present in the system of interest, compared with reference calculations e.g. from DFT. The cost function is then minimized by some optimizer, yielding the electronic part parameters.

7.2.7 Repulsion Potential Training

As explained previously, the repulsion potential has a similar function as the exchange-correlation energy in DFT, given that it attempts to capture all the higher-order effects that are not treated by the electronic part. In the traditional framework of DFTB, it comes as a set of relatively short-ranged two-body potentials - one for each possible combination of atomic species in the system, both homo- and hetero-nuclear. Despite its name, there is no obligation for the repulsion potential to be purely repulsive for its entire range - that is only the case in the short-distance limit [141].

There are multiple challenges that arise during the process of fitting a good set of repulsion potentials. It needs to be sufficiently adaptive to capture the physical nuances of all the effects summarized by the repulsion energy, while also being not *so* complicated, that the complexity and cost of the fitting procedure become a hindrance - especially the more different atomic species there are present in the system of interest [11]. Past endeavours have typically struggled with balancing these requirements, either being very rigid [9, 129, 136], or very cumbersome [142, 143], with many functional parameters. The latter problem can be mitigated to a degree by more efficient optimization algorithms, which has been attempted by multiple groups [144, 145], to some success, but only with the recent advances in machine-learning methods, it has truly become possible to get the best of both worlds. Machine-learned repulsion potentials like GPrep [11] allow for fully adaptive functional forms, while also making a simultaneous and fast

parametrization process possible, in a purely data-driven approach. See section 7.3 for details.

A more general challenge to the traditional two-body interpretation of the repulsion potential is the obvious fact that it cannot distinguish between different chemical environments around the otherwise identical constellation of two atoms. This is irrelevant in many systems, but important in many others, and strongly limits the possible transferability, which can ever be achieved with this approach. There have been several ideas on how to circumvent this issue, among them so-called generalized repulsive potentials [146], which employ machine-learning in order not only to teach their potentials the atom-types of the pair, but also introduce a variable bond-type between them. Another proposition is the introduction of polarizability and crystal field terms [147]. However, with the recent progress in machine-learned atomic potentials like ACE/PACE [15–17] and frameworks like ChIMES [137–139], we believe that many-body repulsion potentials will become the superior approach to making DFTB more general and transferable in the future.

7.2.8 Applications in this Work

Creating and gradually improving our DFTB parametrization for lithium intercalated graphite has been one of the primary tasks in this work. We trained against references based on DFT, with the PBE functional [90, 91] and the many-body-dispersion correction MBD [101]. For the electronic part, we found it unnecessary to change the free-atom energy eigenvalues ε and Hubbard parameters U. Our cost function consisted of a selection of features from the band-structures of lithium metal, graphite and diamond, and was optimized in 2D space by means of the particle swarm optimizer (PSO) [144].

The two-body repulsion potentials were fitted by means of the Gaussian process regression framework GPrep [11], against forces of distorted equilibrium structures throughout the entire range of charge, as well as diffusion step intermediates. In order to aid the learning of dispersive effects to a sufficient degree, we furthermore switch on a Lennard Jones (LJ) [148] dispersion correction. This way, we essentially teach the repulsion potential the difference between the simple LJ and the more sophisticated MBD dispersion correction, which we assume to be comparable at least in the long range beyond the cutoff of our repulsion potential.

In terms of applications, our DFTB parametrization was used extensively to investigate atomistic and previously inaccessible meso-scale properties of Li-GIC anodes. Beyond that, it is also featured as an integral part of the multi-scale model in two ways: by providing accurate diffusion barriers and relative permittivity in dependence of a large, semi-local environment of the respective Li-ion or vacancy, which is essential for (charge-) kMC simulations, and by providing large reference databases for the future endeavour of training even cheaper cluster expansion models. The exact settings like k-grid and convergence criteria of the DFTB calculations have been continually modified throughout this work and we refer to the papers for details.

7.3 Gaussian Process Regression

As outlined previously, the task of fitting the repulsion potential can be formalized as follows: based on a data set consisting of n data points (x_i, y_i), with x the input space and y the resulting values of the property of interest, the goal is to approximate the underlying, unknown functional relationship $f(x)$ as accurately as possible. In our specific case, x corresponds to the relative positions and species of the atoms, and y to the forces the atoms experience, as predicted by the DFT reference method.

In order to achieve this, the approach of choice in this work is Gaussian process regression (GPR), which falls into the category of Bayesian machine learning. Specifically, it aims at calculating a predicted probability distribution $p(\mathbf{f}(x_{\text{test}})|x_{\text{test}}, x, y)$ of the property value corresponding to an arbitrary input point x_{test}, which is not required to be part of the training space. For this, Bayes theorem is employed:

$$p(\mathbf{f}_A|\mathbf{f}_B) = \frac{p(\mathbf{f}_A)p(\mathbf{f}_B|\mathbf{f}_A)}{p(\mathbf{f}_B)} \tag{41}$$

with $p(\mathbf{f}_A|\mathbf{f}_B)$ the conditional probability distribution of A in the event of B. In the context of our present application, one can relate $\mathbf{f}_B$ to the available training data, and $\mathbf{f}_A$ to the model parameters, which in turn determine the prediction.

First, some formalism to express our probability distributions is required. Here, the choice is a Gaussian process (a generalization of the multivariate Gaussian distribution), which is fully defined by its mean, which in turn is formally variable but has been set to zero within this approach,

$$m(x) = \langle f(x) \rangle \tag{42}$$

and its covariance function, which measures the similarity between two points x, x' of the input space [149],

$$k(x, x') = \langle (f(x) - m(x))(f(x') - m(x')) \rangle \tag{43}$$

Based on this, Bayes theorem can be rewritten as

$$p(\mathbf{f}(x_{\text{test}}), \mathbf{f}(x)|x_{\text{test}}, x, y) = \frac{p(\mathbf{f}(x_{\text{test}}), \mathbf{f}(x)|x_{\text{test}}, x)p(y|\mathbf{f}(x))}{p(y)} \tag{44}$$

Next, the training targets $\mathbf{f}(x)$ are integrated out, leaving us with the desired probability distribution:

$$p(\mathbf{f}(x_{\text{test}})|x_{\text{test}}, x, y) = \int p(\mathbf{f}(x_{\text{test}}), \mathbf{f}(x)|x_{\text{test}}, x, y)d\mathbf{f} \tag{45}$$

Finally, after making use of the Gaussian process as the functional form, the mean of this posterior

distribution can be written as

$$\overline{f}(x_{\text{test}}) = \sum_{i=1}^{n} \alpha_i k(x_{\text{test}}, x_i) \tag{46}$$

with the coefficients α_i only depending on the training set. It is this mean, which is then used as the repulsion potential – see figure 9 for an illustration.
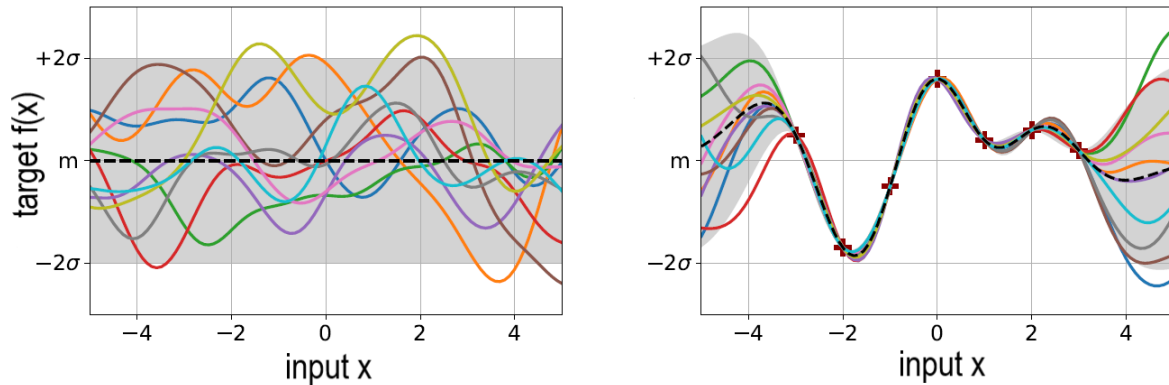

Figure 9: Exemplary illustration of a Gaussian process regression in 1D input space [149]. Coloured lines constitute the ensemble of Gaussian processes – linear combinations of kernel functions with different coefficients – with the black dashed line being the mean there-of. By incorporating the knowledge of the training data points and their prediction values, the prior distribution $p(\mathbf{f}(x_{\text{test}})|x_{\text{test}})$ (*left*) becomes the posterior distribution $p(\mathbf{f}(x_{\text{test}})|x_{\text{test}}, x, y)$ (*right*).

The computational bottleneck for the determination of the coefficients is the inversion of the covariance matrix K, which has the dimensions $N_{\text{pairs}} \times N_{\text{pairs}}$, with N_{pairs} denominating the number of atom pairs in the training set, which can obviously become quite large. In order to combat this problem, a sparsification approach is applied to reduce the dimensionality of the problem, making use of redundancy in the data set. For details, we refer to the GAP framework by Bartók et al. [12].

With all this in place, their remains the task to define the covariance (kernel) function $k(x, x')$, which measures the similarity between two elements of the input space. For this, we choose to employ the "squared exponential" kernel (SE):

$$k_{\text{SE}}(x, x') = \exp\left(\frac{-|x - x'|^2}{\theta^2}\right) \tag{47}$$

The parameter θ defines the length-scale on which the kernel operates, or in other words, how "lenient" it is, i.e. how quickly the kernel value decreases from 1 to 0 with decreasing similarity between the input points. Since the repulsion potential V_{rep} is constructed as a linear combination of kernel functions, θ also becomes a hyperparameter for the predictive model, which contributes to the smoothness of the repulsion potentials.

There is a number of additional hyperparameters which need to be defined within the GPR approach, namely the number of sparse input points N_s, the regularization parameter σ and

parameters of the cutoff function limiting the range of the repulsion potential. For details, we refer to the first paper included in this thesis [61], but in summary, within certain ranges, $V_{\rm rep}$ is rather robust to minor changes of these hyperparameters. Finding these ranges is an integral part of the parametrization process. An intuitive explanation for this can be derived – in the spirit of Bayesian learning – from the fact that the choices of hyperparameters essentially correspond to the choice of "prior" in the Bayesian context. Therefore, any reasonable prior should be able to converge to a similarly good fit of the available training data, given that the latter is sufficiently abundant and diverse.

8 Publications

8.1 DFTB Modeling of Lithium-Intercalated Graphite with Machine-Learned Repulsive Potential
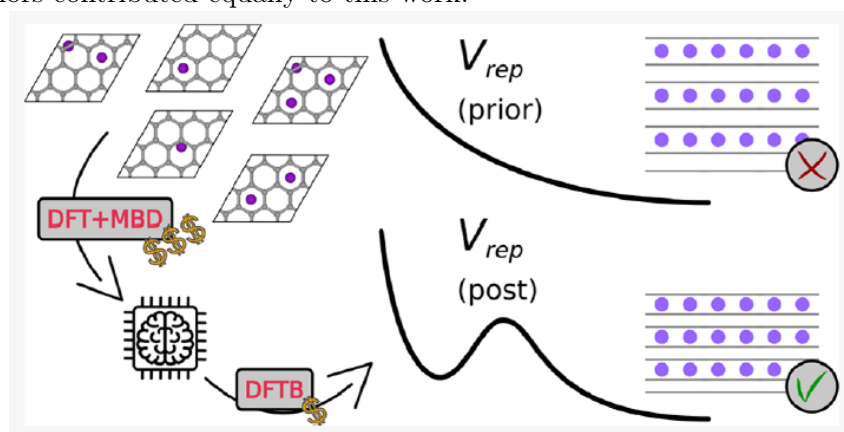
DFTB Modeling of Lithium-Intercalated Graphite with Machine-Learned Repulsive Potential

Chiara Panosetti,*[||] Simon B. Anniés,[||] Cristina Grosu, Stefan Seidlmayer, and Christoph Scheurer

||: These authors contributed equally to this work.

Summary: In this work, we first explored the possibility of using the GPR framework GPrep [11], which was previously developed within the group, in order to construct an accurate DFTB parametrization for lithium intercalated graphite. The primary focus was on establishing the workflow and on providing some good practices, to ensure not only accurate predictions, but also stability in the hyperparameter-space, and to avoid over- and under-fitting, which is crucial for good extrapolation behaviour outside of the trained-upon chemical space.

For the electronic part, we proclaimed a reasonable cost function based on selected features of the band structures of graphite, diamond and metallic lithium, which is optimized by means of a PSO in the 2D hyperparameter-space. The band-structure of LiC_6 was used as an example to show that our resulting Slater-Koster files extrapolate well and produce good results (within realistic expectations for a tightly bound model).

For the repulsion part, we investigated which types of structures (rattled and scaled equilibrium configurations as well as diffusion step intermediates) need to be included in the training set. The hyperparameter-space was rigorously investigated in terms of physicality and robustness of the resulting parametrizations. Beyond that, we also explored how to best incorporate the very important vdW interactions into our studies, settling on the MBD post-correction scheme [101] for the reference DFT calculations. For the DFTB calculations, a simple Leonnard-Jones (LJ)

model was applied. We found that the difference between the two corrections schemes can be encoded in the repulsion potential sufficiently well.

With all that in place, we obtained a parametrization that is capable of reproducing structural properties and local forces at all states of charge as well as the highest-level DFT methods available, at a fraction of the cost. We also predicted a set of diffusion barriers which agree well with significantly more expensive results from literature.

Individual Contributions: The parametrization process of the electronic part was a collaborative effort conceptually, but mostly executed by Dr. Chiara Panosetti. The construction of the various training set geometries, selection of the reference DFT functional and vdW correction, parametrization of the repulsion potentials and investigation of the corresponding hyperparameter-space was done by me, in close collaboration with Dr. Panosetti and Dr. Christoph Scheurer. The writing process and presentation of the results were a shared effort.

8.2 Accessing Structural, Electronic, Transport and Mesoscale Properties of Li-GICs via a Complete DFTB Model with Machine-Learned Repulsion Potential

Accessing Structural, Electronic, Transport and Mesoscale Properties of Li-GICs via a Complete DFTB Model with Machine-Learned Repulsion Potential

Simon Anniés [1,†] , Chiara Panosetti [1,2,*,†] , Maria Voronenko [1], Dario Mauth [1], Christiane Rahe [3] and Christoph Scheurer [2]
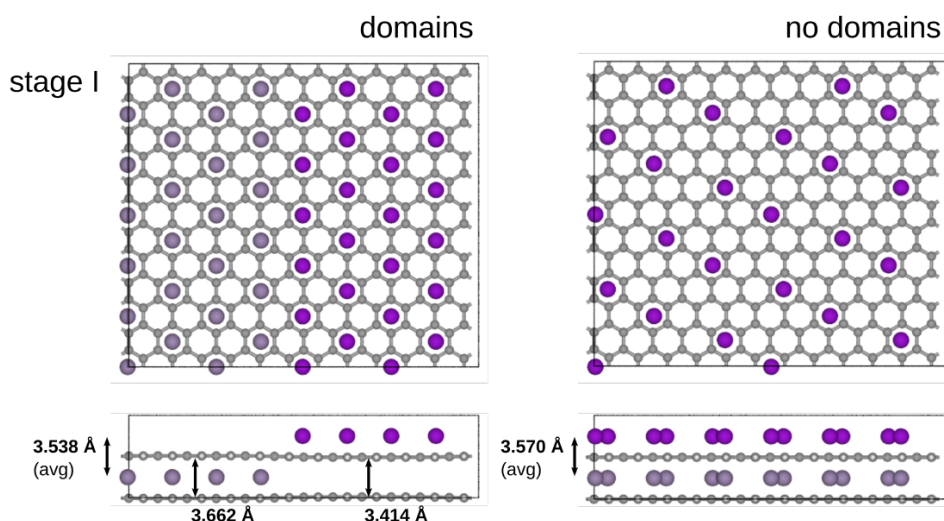
[1] Department of Chemistry, Technische Universität München, Lichtenbergstr. 4, 85748 Garching, Germany; simon.annies@tum.de (S.A.); maria.voronenko@tum.de (M.V.); dario.mauth@tum.de (D.M.)
[2] Fritz Haber Institute of the Max Planck Society, Faradayweg 4-6, 14195 Berlin, Germany; scheurer@fhi.mpg.de
[3] ISEA, RWTH Aachen University, Jägerstraße 17-19, 52066 Aachen, Germany; christiane.rahe@isea.rwth-aachen.de
* Correspondence: panosetti@fhi-berlin.mpg.de
† These authors contributed equally to this work.

Summary: In this work, we continued the development of our parametrization by including some previously neglected key features and additional benchmark criteria. One primary task was adding the lithium-lithium repulsion potential to the parametrization, without negatively impacting the previously demonstrated performance. Those interactions had been skipped in the previous work, because they are not needed for describing Li-GICs of the stoichiometries Li_xC_6, x ∈ [0:1], which was until very recently considered the "full" range of SOC. However, new findings by our experimental collaborators suggested that locally over-lithiated configurations are in fact possible at ambient conditions. In order to be able to investigate those, as well as dendrite formation at the anode-electrolyte interface and metallic lithium deposition between graphite grains, repulsive Li-Li interactions become non-negligible. We showed that extending the existing model by these interactions is unproblematic within the framework we had developed, simply by adding some lithium metal clusters and molecular dynamics snapshots to the

training set.

Additionally we extended our list of benchmark properties to the formation energies of LiC_6, LiC_{12} and LiC_{18}, which are necessary for estimating open circuit voltage (OCV) curves upon charging and discharging the anodes, as well as LiC_2 – representative for over-lithiated compounds, which we were able to capture nicely after some modifications of the hyperparameters.

Based on these improvements, we were able to conduct some new investigations, that were not possible before. We demonstrated that our method is capable of the full structure relaxation of large supercells in the order of thousands of atoms, and that within those, local domain areas relax to the expected local layer distances and are energetically favoured over dilute configurations (which is in agreement with experimental results and accepted theory). We furthermore sampled the intra-layer, long-ranged interactions between two lithium ions, validated that those are indeed predicted as Coulombic in nature, and explained how the intrinsic dielectric constant of the material can be calculated from it.

Individual Contributions: The construction of the Li-metal-like reference structures was done by Dario Mauth, under the supervision of Dr. Chiara Panosetti. The reparametrization, including said structures and taking into account the formation energies, was a shared effort between Dr. Panosetti and me. Dr. Christiane Rahe provided additional experimental references for the energetics, which were used for validation. The groundwork for analyzing the long-ranged Coulomb interactions was laid by Maria Voronenko. All other calculations and analyses there-of were performed by me, as well as most of the writing process and the presentation of the results. Dr. Panosetti and Dr. Christoph Scheurer provided input and guidance throughout the whole project.

8.3 The Intrinsic Electrostatic Dielectric Behaviour of Graphite Anodes in Li-Ion Batteries – Across the Entire Functional Range of Charge
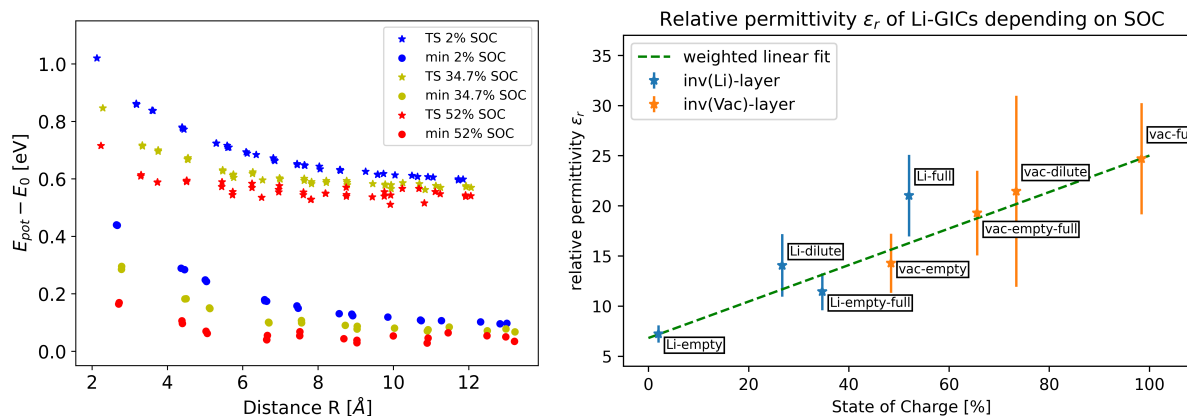
The intrinsic electrostatic dielectric behaviour of graphite anodes in Li-ion batteries—Across the entire functional range of charge

Simon Anniés [a,b,*], Christoph Scheurer [a], Chiara Panosetti [a]

[a] Fritz-Haber-Institute of the Max–Planck-Society, Faradayweg 4-6, 14195, Berlin, Germany
[b] Chair for Theoretical Chemistry, TU Munich, Lichtenbergstr. 4, 85747, Garching b. München, Germany

Summary: Building directly upon the results presented in the previous paper, we set out – for the first time – to investigate the dielectric behaviour of lithium intercalated graphite anodes, for the entire stoichiometric range accessed during a full charging-/discharging-cycle - a property, that is highly desired by the charge kinetic Monte Carlo (kMC) community, for the investigation of non equilibrium processes during fast charging cycles and in general for finally linking macro- and meso-scale properties of the system. At the present time, this investigation would not have been possible with any other modeling technique, due to the long-ranged nature of the interactions of interest.

Our approach was to sample the interactions between Li-ion- and Li-ion-vacancy-pairs at varying distances and with varying charge densities surrounding them. This required hundreds of full structure relaxations of supercells in the order of 1000 atoms, a size that was necessary in order to avoid the long-ranged Coulomb interactions being affected by the periodic images. Based on these calculations, we were able to discover a linear dependency of the dielectric screening on the state of charge (from ≈ 7 at 0% SOC to ≈ 25 at 100% SOC), which is reasonably robust to the exact realization of each stoichiometry. Furthermore, we also investigated the qualitative differences between the dielectric screening in-plane vs. out-of-plane, which is important for comparing experimental results that were obtained with randomly oriented graphite powder

samples, with theoretical results stemming from a perfectly oriented single crystal.

While the qualitative behaviour presented here is robust, the qualitative results are to a degree dependent on the Mulliken partial charge estimation within the DFTB framework and need to be taken with a grain of salt because of that, but we illustrated that, in principle, two experimental measurements at different SOC would suffice to validate them.

Individual Contributions: I constructed all geometries and performed all calculations featured in this paper. The theoretical analysis, discussion of the energetics and partial charges and presentation of the results were performend by me, in close collaboration with Dr. Chiara Panosetti and Dr. Christoph Scheurer. The writing process was mostly done by me.

9 Conclusions & Outlook

Kinetic and electrochemical processes inside and at the interface of the carbon anode are the causes of many limitations regarding the further development and improvement of lithium ion batteries (LIBs) in terms of safety, charging speed and low temperature performance. The complex behaviour of intercalated lithium, including the formation of stages and domains, the appearance of stage transitions, as well as the necessity of investigating the full range of state of charge (SOC) require simulations at mesoscale length scales inaccessible to density functional theory (DFT). Furthermore, an accurate description of dispersion effects like van der Waals (vdW) forces is required in order to achieve accurate diffusion barriers and energy ordering of different realizations of identical stoichiometries. These interactions are long-ranged in nature and can therefore not be captured by employing an atomic force field approach like ACE [15, 17] – at least not by itself.

In this work, we aimed at and succeeded in bridging this gap in simulation capability. This was achieved by developing a density functional tight binding (DFTB) parametrization, based on the GPrep [11] module – a framework for employing Bayesian GPR in order to formulate and train accurate, flexible repulsion potentials. This allowed us to bring forward a simulation tool which combines the speed and efficiency of an atomic force field approach with the physicality and versatility of DFT – at only a very minor cost in accuracy compared to the latter.

Making use of this model, we were able to calculate accurate diffusion barriers at speeds that are viable for an on-the-fly approach within kinetic Monte Carlo (kMC) simulations. Alternatively, sufficiently large sets of diffusion processes with differing surrounding lithium distributions could be calculated in order to train a surrogate model based on local environment descriptors like smooth overlap of atomic positions (SOAP) [13] for the same purpose. This should help bring forward much more advanced kMC simulations in the future, which are no longer reliant on a crude fixed barrier approximation.

Beyond that, our ability to calculate and relax much larger crystal cells, than e.g. with DFT, allowed for the validation of mechanisms stabilizing local domains during the intercalation process. Furthermore, we were able to sample the long-ranged Coulomb interactions between intercalated pairs of Li-ions and vacancies, within different surrounding charge densities, in order to – for the first time – calculate the dependency of the relative permittivity (also referred to as dielectric constant) on the state of charge. This was found to be linear and only negligibly dependent on the exact realization of a certain stoichiometry. Additionally, we were able to separately calculate this relative permittivity for the in-plane and the out-of-plane space directions, finding large differences. This allows for a more educated comparison between calculations and experimental measurements performed on graphite powder samples.

With our work here, we laid the groundwork for promising future investigations. Especially, kMC simulations will benefit greatly from the diffusion barriers (and semi-local dependencies there-of), as well as the SOC dependence of the dielectric behaviour we uncovered in this work. Due to this, new insights into the kinetic processes governing the limits of safe fast-charging of LIBs are expected in the near future.

41

Additionally, we see great promise in the general approach and workflow presented here. The combination of a simplified electron density in a tight-binding formulation with recently developed machine-learned interatomic force fields like ChIMES and ACE will be a major breakthrough for the simulation of complex functional materials, and we believe future endeavours of this nature will benefit from the example we lay out in this work.

10   Licences

Figures 3 and 4 are from the open access source [32], accessible at https://doi.org/10.1039/D0SE00175A. Full ownership is with the publisher. This work is licensed under the Creative Commons Attribution 3.0 Unported License. To view a copy of this license, visit http://creativecommons.org/licenses/by/3.0/ or send a letter to Creative Commons, PO Box 1866, Mountain View, CA 94042, USA.

Figure 6 is from the open access source [74], accessible at https://doi.org/10.1063/1.4850877. Full ownership is with the publisher. This work is licensed under the Creative Commons Attribution-NonCommercial-NoDerivatives 4.0 International License. To view a copy of this license, visit http://creativecommons.org/licenses/by-nc-nd/4.0/ or send a letter to Creative Commons, PO Box 1866, Mountain View, CA 94042, USA.

Figure 9 is from the source [149]. Permission for use has been granted by the author and can be proved upon request.

11 Acknowledgements

References

1. Anniés, S., Scheurer, C. & Panosetti, C. The intrinsic electrostatic dielectric behaviour of graphite anodes in Li-ion batteries—Across the entire functional range of charge. *Electrochimica Acta* **444,** 141966 (2023).

2. Sharp, M. *et al.* Extreme melt on Canada's Arctic ice caps in the 21st century. *Geophys. Res. Lett.* **38** (2011).

3. Fisher, D. *et al.* Recent melt rates of Canadian arctic ice caps are the highest in four millennia. *Glob. Planet. Change* **84,** 3 (2012).

4. Program, U. G. C. R. *Impacts of climate change on human health in the United States: a scientific assessment* (Skyhorse Publishing, 2018).

5. Anderson, T. R., Hawkins, E. & Jones, P. D. CO2, the greenhouse effect and global warming: from the pioneering work of Arrhenius and Callendar to today's Earth System Models. *Endeavour* **40,** 178 (2016).

6. Scrosati, B. History of lithium batteries. *J. Solid State Electrochem.* **15,** 1623 (2011).

7. Kebede, A. A. *et al.* Techno-economic analysis of lithium-ion and lead-acid batteries in stationary energy storage application. *J. Energy Storage* **40,** 102748 (2021).

8. Gallagher, K. G. *et al.* Optimizing areal capacities through understanding the limitations of lithium-ion electrodes. *J. Electrochem. Soc.* **163,** A138 (2015).

9. Oliveira, A. F., Philipsen, P. & Heine, T. DFTB parameters for the periodic table, part 2: Energies and energy gradients from hydrogen to calcium. *J. Chem. Theory Comput.* **11,** 5209 (2015).

10. Jenke, J., Ladines, A. N., Hammerschmidt, T., Pettifor, D. G. & Drautz, R. Tight-binding bond parameters for dimers across the periodic table from density-functional theory. *Phys. Rev. Mater.* **5,** 023801 (2021).

11. Panosetti, C., Engelmann, A., Nemec, L., Reuter, K. & Margraf, J. T. Learning to Use the Force: Fitting Repulsive Potentials in Density-Functional Tight-Binding with Gaussian Process Regression. *J. Chem. Theory Comput.* **16,** 2181 (2020).

12. Bartók, A. P., Payne, M. C., Kondor, R. & Csányi, G. Gaussian approximation potentials: The accuracy of quantum mechanics, without the electrons. *Phys. Rev. Lett.* **104,** 136403 (2010).

13. Bartók, A. P., Kondor, R. & Csányi, G. On representing chemical environments. *Phys. Rev. B* **87,** 184115 (2013).

14. Bartók, A. P. & Csányi, G. Gaussian approximation potentials: A brief tutorial introduction. *Int. J. Quantum Chem.* **115,** 1051 (2015).

15. Dusson, G. *et al.* Atomic cluster expansion: Completeness, efficiency and stability. *J. Computat. Phys.* **454,** 110946 (2022).

16. Lysogorskiy, Y. *et al.* Performant implementation of the atomic cluster expansion (PACE) and application to copper and silicon. *npj Comput. Mater.* **7,** 1 (2021).

17. Kovács, D. P. *et al.* Linear atomic cluster expansion force fields for organic molecules: beyond rmse. *J. Chem. Theory Comput.* **17,** 7696 (2021).

18. Scrosati, B. & Garche, J. Lithium batteries: Status, prospects and future. *J. Power Sources* **195,** 2419 (2010).

19. Lu, L., Han, X., Li, J., Hua, J. & Ouyang, M. A review on the key issues for lithium-ion battery management in electric vehicles. *J. Power Sources* **226,** 272 (2013).

20. Durmus, Y. E. *et al.* Side by side battery technologies with lithium-ion based batteries. *Adv. Energy Mater.* **10,** 2000089 (2020).

21. Gao, X.-L., Liu, X.-H., Xie, W.-L., Zhang, L.-S. & Yang, S.-C. Multiscale observation of Li plating for lithium-ion batteries. *Rare Met.* **40,** 3038 (2021).

22. Lin, X., Khosravinia, K., Hu, X., Li, J. & Lu, W. Lithium plating mechanism, detection, and mitigation in lithium-ion batteries. *Prog. Energy Combust. Sci.* **87,** 100953 (2021).

23. Doh, C.-H., Han, B.-C., Jin, B.-S. & Gu, H.-B. Structures and Formation Energies of Li_xC_6 (x=1−3) and its Homologues for Lithium Rechargeable Batteries. *Bull. Korean Chem. Soc.* **32,** 2045 (2011).

24. Waldmann, T., Kasper, M. & Wohlfahrt-Mehrens, M. Optimization of charging strategy by prevention of lithium deposition on anodes in high-energy lithium-ion batteries–electrochemical experiments. *Electrochim. Acta* **178,** 525 (2015).

25. Waldmann, T., Hogg, B.-I. & Wohlfahrt-Mehrens, M. Li plating as unwanted side reaction in commercial Li-ion cells–A review. *J. Power Sources* **384,** 107 (2018).

26. Aryanfar, A. *et al.* Dynamics of lithium dendrite growth and inhibition: Pulse charging experiments and Monte Carlo calculations. *J. Phys. Chem. Lett.* **5,** 1721 (2014).

27. Zheng, F., Kotobuki, M., Song, S., Lai, M. O. & Lu, L. Review on solid electrolytes for all-solid-state lithium-ion batteries. *J. Power Sources* **389,** 198 (2018).

28. Daniel, C., Mohanty, D., Li, J. & Wood, D. L. *Cathode materials review* in *AIP Conference Proceedings* **1597** (2014), 26.

29. Mishra, A. *et al.* Electrode materials for lithium-ion batteries. *Mater. Sci. Energy Technol.* **1,** 182 (2018).

30. Besenhard, J. & Fritz, H. Cathodic reduction of graphite in organic solutions of alkali and NR_4^+ salts. *J. Electroanal. Chem. Interfacial Electrochem.* **53,** 329 (1974).

31. Besenhard, J. The electrochemical preparation and properties of ionic alkali metal-and NR_4-graphite intercalation compounds in organic electrolytes. *Carbon* **14,** 111 (1976).

32. Asenbauer, J. *et al.* The success story of graphite as a lithium-ion anode material–fundamentals, remaining challenges, and recent developments including silicon (oxide) composites. *Sustain. Energy Fuels* **4,** 5387 (2020).

33. Nitta, N., Wu, F., Lee, J. T. & Yushin, G. Li-ion battery materials: present and future. *Mater. Today* **18,** 252 (2015).

34. Nishi, Y. Lithium ion secondary batteries; past 10 years and the future. *J. Power Sources* **100,** 101 (2001).

35. Laman, F. & Brandt, K. Effect of discharge current on cycle life of a rechargeable lithium battery. *J. Power Sources* **24,** 195 (1988).

36. Zhang, H., Yang, Y., Ren, D., Wang, L. & He, X. Graphite as anode materials: Fundamental mechanism, recent progress and advances. *Energy Storage Mater.* **36,** 147 (2021).

37. Weaving, J. *et al.* Development of high energy density Li-ion batteries based on LiNi$_{1\text{-x-y}}$Co$_{\text{x}}$Al$_{\text{y}}$O$_2$. *J. Power Sources* **97,** 733 (2001).

38. Intelligence, B. M. *Elon Musk: Our lithium ion batteries should be called* 2018.

39. Chen, T., Wu, J., Zhang, Q. & Su, X. Recent advancement of SiO$_{\text{x}}$ based anodes for lithium-ion batteries. *J. Power Sources* **363,** 126 (2017).

40. Nagai, R., Kita, F., Yamada, M. & Katayama, H. Development of highly reliable high-capacity batteries for mobile devices and small-to medium-sized batteries for industrial applications. *Energy* **450,** 350 (2003).

41. DiVincenzo, D., Fuerst, C. & Fischer, J. (P, T) phase boundary in Li-intercalated graphite: Theory and experiment. *Phys. Rev. B* **29,** 1115 (1984).

42. Solin, S. The nature and structural properties of graphite intercalation compounds. *Adv. Chem. Phys* **49,** 455 (1982).

43. Imai, Y. & Watanabe, A. Energetic evaluation of possible stacking structures of Li-intercalation in graphite using a first-principle pseudopotential calculation. *J. Alloys Compd.* **439,** 258 (2007).

44. Trucano, P. & Chen, R. Structure of graphite by neutron diffraction. *Nature* **258,** 136 (1975).

45. Yin, M. & Cohen, M. L. Structural theory of graphite and graphitic silicon. *Phys. Rev. B* **29,** 6996 (1984).

46. Grosu, C. *et al. Revisiting the storage capacity limit of graphite battery anodes: spontaneous lithium overintercalation at ambient pressure* 2021.

47. Tanaka, U., Sogabe, T., Sakagoshi, H., Ito, M. & Tojo, T. Anode property of boron-doped graphite materials for rechargeable lithium-ion batteries. *Carbon* **39,** 931 (2001).

48. Kang, S.-X. *et al.* Boosted electrochemical performance of graphite anode enabled by polytetrafluoroethylene-derived F-doping. *Mater. Chem. Phys.* **261,** 124214 (2021).

49. Lee, Y. T., Yoon, C. S. & Sun, Y.-K. Improved electrochemical performance of Li-doped natural graphite anode for lithium secondary batteries. *J. Power Sources* **139,** 230 (2005).

50. Markey, B. *et al.* Effective upcycling of graphite anode: healing and doping enabled direct regeneration. *J. Electrochem. Soc.* **167,** 160511 (2020).

51. Euchner, H., Vinayan, B. P., Reddy, M. A., Fichtner, M. & Groß, A. Alkali metal insertion into hard carbon–the full picture. *J. Mater. Chem. A* **8,** 14205 (2020).

52. Bommier, C., Ji, X. & Greaney, P. A. Electrochemical properties and theoretical capacity for sodium storage in hard carbon: insights from first principles calculations. *Chem. Mater.* **31,** 658 (2018).

53. Zhao, L. *et al.* Revisiting the Roles of Natural Graphite in Ongoing Lithium-Ion Batteries. *Adv. Mater.* **34,** 2106704 (2022).

54. Ma, C. *et al.* Synthesis and electrochemical properties of artificial graphite as an anode for high-performance lithium-ion batteries. *Carbon* **64,** 553 (2013).

55. Glazier, S., Li, J., Louli, A., Allen, J. & Dahn, J. An analysis of artificial and natural graphite in lithium ion pouch cells using ultra-high precision coulometry, isothermal microcalorimetry, gas evolution, long term cycling and pressure measurements. *J. Electrochem. Soc.* **164,** A3545 (2017).

56. Allart, D., Montaru, M. & Gualous, H. Model of lithium intercalation into graphite by potentiometric analysis with equilibrium and entropy change curves of graphite electrode. *J. Electrochem. Soc.* **165,** A380 (2018).

57. Mundszinger, M. *et al.* Morphology and texture of spheroidized natural and synthetic graphites. *Carbon* **111,** 764 (2017).

58. Zhao, H. *et al.* Modification of natural graphite for lithium ion batteries. *Solid State Sci.* **10,** 612 (2008).

59. Hofmann, U. & Rüdorff, W. The formation of salts from graphite by strong acids. *J. Chem. Soc. Faraday Trans.* **34,** 1017 (1938).

60. Lenchuk, O., Adelhelm, P. & Mollenhauer, D. Comparative study of density functionals for the description of lithium-graphite intercalation compounds. *J. Comput. Chem.* **40,** 2400 (2019).

61. Panosetti, C., Anniés, S. B., Grosu, C., Seidlmayer, S. & Scheurer, C. DFTB Modeling of Lithium-Intercalated Graphite with Machine-Learned Repulsive Potential. *J. Phys.Chem. A* **125,** 691 (2021).

62. Persson, K. *et al.* Lithium diffusion in graphitic carbon. *J. Phys. Chem. Lett.* **1,** 1176 (2010).

63. Daumas, N. & Herold, A. Relations between phase concept and reaction mechanics in graphite insertion compounds. *C. R. Hebd. Séances Acad. sci.* **268,** 373 (1969).

64. Safran, S. A. & Hamann, D. R. Long-Range Elastic Interactions and Staging in Graphite Intercalation Compounds. *Phys. Rev. Lett.* **42,** 1410 (1979).

65. Safran, S. Phase diagrams for staged intercalation compounds. *Phys. Rev. Lett.* **44,** 937 (1980).

66. Safran, S. & Hamann, D. Self-consistent charge densities, band structures, and staging energies of graphite intercalation compounds. *Phys. Rev. B* **23,** 565 (1981).

67. Hawrylak, P. & Subbaswamy, K. R. Kinetic Model of Stage Transformation and Intercalation in Graphite. *Phys. Rev. Lett.* **53,** 2098 (1984).

68. Kirczenow, G. Interference Phenomena in the Theory of Daumas-Hérold Domain Walls. *Phys. Rev. Lett.* **49,** 1853 (1982).

69. Kirczenow, G. Stage Order, Disorder, and Phase Transitions in Intercalation Compounds. *Phys. Rev. Lett.* **52,** 437 (1984).

70. Kirczenow, G. Domain model of stage order and disorder in intercalation compounds. *Phys. Rev. B* **31,** 5376 (1985).

71. Axdal, S. A. & Chung, D. A theory for the kinetics of intercalation of graphite. *Carbon* **25,** 377 (1987).

72. Wang, F. *et al.* Chemical Distribution and Bonding of Lithium in Intercalated Graphite: Identification with Optimized Electron Energy Loss Spectroscopy. *ACS Nano* **5,** 1190 (2011).

73. Dimiev, A. M. *et al.* Direct real-time monitoring of stage transitions in graphite intercalation compounds. *ACS nano* **7,** 2773 (2013).

74. Krishnan, S. *et al.* Revisiting the domain model for lithium intercalated graphite. *Appl. Phys. Lett.* **103,** 251904 (2013).

75. Gavilán-Arriazu, E. M. *et al.* The kinetic origin of the Daumas-Hérold model for the Li-ion/graphite intercalation system. *Electrochem. Commun.* **93,** 133 (2018).

76. Yadegari, H. *et al.* Operando measurement of layer breathing modes in lithiated graphite. *ACS Energy Lett.* **6,** 1633 (2021).

77. Von Lilienfeld, O. A., Tavernelli, I., Rothlisberger, U. & Sebastiani, D. Optimization of Effective Atom Centered Potentials for London Dispersion Forces in Density Functional Theory. *Phys. Rev. Lett.* **93,** 153004 (2004).

78. Persson, K., Hinuma, Y., Meng, Y. S., Van der Ven, A. & Ceder, G. Thermodynamic and kinetic properties of the Li-graphite system from first-principles calculations. *Phys. Rev. B* **82,** 125416 (2010).

79. Anniés, S. *et al.* Accessing Structural, Electronic, Transport and Mesoscale Properties of Li-GICs via a Complete DFTB Model with Machine-Learned Repulsion Potential. *Mater.* **14,** 6633 (2021).

80. Dahn, J., Fong, R. & Spoon, M. Suppression of staging in lithium-intercalated carbon by disorder in the host. *Phys. Rev. B* **42,** 6424 (1990).

81. Xu, B., Wu, M. S., Liu, G. & Ouyang, C. Y. Understanding the effect of the layer-to-layer distance on Li-intercalated graphite. *J. Appl. Phys.* **111,** 124325 (2012).

82. Gavilán-Arriazu, E. M. *et al.* Kinetic Monte Carlo applied to the electrochemical study of the Li-ion graphite system. *Electrochim. Acta* **331,** 135439 (2020).

83. Gavilán-Arriazu, E. M., Mercer, M., Barraco, D. E., Hoster, H. & Leiva, E. Kinetic Monte Carlo simulations applied to Li-ion and post Li-ion batteries: a key link in the multi-scale chain. *Prog. Energy* **3,** 042001 (2021).

84. Koch, W. & Holthausen, M. C. *A chemist's guide to density functional theory* (John Wiley & Sons, 2015).

85. Bartlett, R. J. & Musiał, M. Coupled-cluster theory in quantum chemistry. *Rev. Mod. Phys.* **79,** 291 (2007).

86. Drautz, R. Atomic cluster expansion for accurate and transferable interatomic potentials. *Phys. Rev. B* **99,** 014104 (2019).

87. Kohn, W. & Sham, L. J. Self-consistent equations including exchange and correlation effects. *Phys. Rev.* **140,** A1133 (1965).

88. Epstein, S. & Rosenthal, C. The Hohenberg–Kohn theorem. *J. Chem. Phys.* **64,** 247 (1976).

89. Ceperley, D. M. & Alder, B. J. Ground state of the electron gas by a stochastic method. *Phys. Rev. Lett.* **45,** 566 (1980).

90. Perdew, J. P. & Wang, Y. Accurate and simple analytic representation of the electron-gas correlation energy. *Phys. Rev. B* **45,** 13244 (1992).

91. Perdew, J. P., Burke, K. & Ernzerhof, M. Generalized Gradient Approximation Made Simple. *Phys. Rev. Lett.* **77,** 3865 (1996).

92. Ernzerhof, M. & Scuseria, G. E. Assessment of the Perdew–Burke–Ernzerhof exchange-correlation functional. *J. Chem. Phys.* **110,** 5029 (1999).

93. Becke, A. D. Perspective: Fifty years of density-functional theory in chemical physics. *J. Chem. Phys* **140,** 18A301 (2014).

94. Maier, T. M., Arbuznikov, A. V. & Kaupp, M. Local hybrid functionals: Theory, implementation, and performance of an emerging new tool in quantum chemistry and beyond. *Wiley Interdiscip. Rev. Comput. Mol. Sci.* **9,** e1378 (2019).

95. Zhang, M.-Y., Cui, Z.-H., Wang, Y.-C. & Jiang, H. Hybrid functionals with system-dependent parameters: Conceptual foundations and methodological developments. *Wiley Interdiscip. Rev. Comput. Mol. Sci.* **10,** e1476 (2020).

96. Klawohn, S. & Bahmann, H. Self-consistent implementation of hybrid functionals with local range separation. *J. Chem. Theory Comput.* **16,** 953 (2020).

97. Martin, J. M. & Santra, G. Empirical double-hybrid density functional theory: A 'third way'in between WFT and DFT. *Isr. J. Chem.* **60,** 787 (2020).

98. Grimme, S., Antony, J., Ehrlich, S. & Krieg, H. A consistent and accurate ab initio parametrization of density functional dispersion correction (DFT-D) for the 94 elements H-Pu. *J. Chem. Phys* **132,** 154104 (2010).

99. Grimme, S., Ehrlich, S. & Goerigk, L. Effect of the damping function in dispersion corrected density functional theory. *J. Comput. Phys* **32,** 1456 (2011).

100. Tkatchenko, A. & Scheffler, M. Accurate Molecular Van Der Waals Interactions from Ground-State Electron Density and Free-Atom Reference Data. *Phys. Rev. Lett.* **102,** 073005 (2009).

101. Tkatchenko, A., DiStasio, R. A., Car, R. & Scheffler, M. Accurate and Efficient Method for Many-Body van der Waals Interactions. *Phys. Rev. Lett.* **108,** 236402 (2012).

102. Ambrosetti, A., Reilly, A. M., DiStasio Jr, R. A. & Tkatchenko, A. Long-range correlation energy calculated from coupled atomic response functions. *J. Chem. Phys.* **140,** 18A508 (2014).

103. Gould, T., Lebègue, S., Ángyán, J. G. & Bučko, T. A Fractionally Ionic Approach to Polarizability and van der Waals Many-Body Dispersion Calculations. *J. Chem. Theory Comput.* **12,** 5920 (2016).

104. Kim, M. *et al.* uMBD: A materials-ready dispersion correction that uniformly treats metallic, ionic, and van der Waals bonding. *J. Am. Chem. Soc.* **142,** 2346 (2020).

105. Hermann, J. & Tkatchenko, A. Density functional model for van der Waals interactions: Unifying many-body atomic approaches with nonlocal functionals. *Phys. Rev. Lett.* **124,** 146401 (2020).

106. Blum, V. *et al.* Ab initio molecular simulations with numeric atom-centered orbitals. *Comput. Phys Commun.* **180,** 2175 (2009).

107. Deringer, V. L. & Csányi, G. Machine learning based interatomic potential for amorphous carbon. *Phys. Rev. B* **95,** 094203 (2017).

108. Deringer, V. L., Pickard, C. J. & Csányi, G. Data-driven learning of total and local energies in elemental boron. *Phys. Rev. Lett.* **120,** 156001 (2018).

109. Bartók, A. P. *et al.* Machine learning unifies the modeling of materials and molecules. *Sci. Adv.* **3,** e1701816 (2017).

110. Dragoni, D., Daff, T. D., Csányi, G. & Marzari, N. Achieving DFT accuracy with a machine-learning interatomic potential: Thermomechanics and defects in bcc ferromagnetic iron. *Phys. Rev. Mater.* **2,** 013808 (2018).

111. Stewart, J. J. Optimization of parameters for semiempirical methods VI: more modifications to the NDDO approximations and re-optimization of parameters. *J. Mol. Model.* **19,** 1 (2013).

112. Pal, S. *et al.* Nonadiabatic molecular dynamics for thousand atom systems: a tight-binding approach toward PYXAID. *J. Chem. Theory Comput.* **12,** 1436 (2016).

113. Grimme, S., Bannwarth, C. & Shushkov, P. A robust and accurate tight-binding quantum chemical method for structures, vibrational frequencies, and noncovalent interactions of large molecular systems parametrized for all spd-block elements (Z= 1–86). *J. Chem. Theory Comput.* **13,** 1989 (2017).

114. Sheppard, T., Lozovoi, A., Pashov, D., Kohanoff, J. & Paxton, A. Universal tight binding model for chemical reactions in solution and at surfaces. I. Organic molecules. *J. Chem. Phys.* **141,** 044503 (2014).

115. Urban, A., Reese, M., Mrovec, M., Elsässer, C. & Meyer, B. Parameterization of tight-binding models from density functional theory calculations. *Phys. Rev. B* **84,** 155119 (2011).

116. Dral, P. O., Wu, X. & Thiel, W. Semiempirical quantum-chemical methods with orthogonalization and dispersion corrections. *J. Chem. Theory Comput.* **15,** 1743 (2019).

117. Madsen, G. K., McEniry, E. J. & Drautz, R. Optimized orthogonal tight-binding basis: application to iron. *Phys. Rev. B* **83,** 184119 (2011).

118. Porezag, D., Frauenheim, T., Köhler, T., Seifert, G. & Kaschner, R. Construction of tight-binding-like potentials on the basis of density-functional theory: Application to carbon. *Phys. Rev. B* **51,** 12947 (1995).

119. Elstner, M. *et al.* Self-consistent-charge density-functional tight-binding method for simulations of complex materials properties. *Phys. Rev. B* **58,** 7260 (1998).

120. Harris, J. Simplified method for calculating the energy of weakly interacting fragments. *Phys. Rev. B* **31,** 1770 (1985).

121. Foulkes, W. M. C. & Haydock, R. Tight-binding models and density-functional theory. *Phys. Rev. B* **39,** 12520 (1989).

122. Oliveira, A. F., Seifert, G., Heine, T. & Duarte, H. A. Density-functional based tight-binding: an approximate DFT method. *J. Braz. Chem. Soc.* **20,** 1193 (2009).

123. Van Duin, A. C. T., Dasgupta, S., Lorant, F. & Goddard, W. A. ReaxFF: A reactive force field for hydrocarbons. *J. Phys. Chem. A* **105,** 9396 (2001).

124. Nielson, K. D., Van Duin, A. C., Oxgaard, J., Deng, W.-Q. & Goddard, W. A. Development of the ReaxFF reactive force field for describing transition metal catalyzed reactions, with application to the initial stages of the catalytic formation of carbon nanotubes. *J. Phys. Chem. A* **109,** 493 (2005).

125. Senftle, T. P. *et al.* The ReaxFF reactive force-field: development, applications and future directions. *npj Comput. Mater.* **2,** 1 (2016).

126. Sengul, M. Y. *et al.* INDEEDopt: a deep learning-based ReaxFF parameterization framework. *npj Comput. Mater.* **7,** 1 (2021).

127. Aradi, B., Hourahine, B. & Frauenheim, T. DFTB+, a Sparse Matrix-Based Implementation of the DFTB Method. *J. Phys. Chem. A* **111,** 5678 (2007).

128. Hourahine, B. *et al.* DFTB+, a software package for efficient approximate density functional theory based atomistic simulations. *J. Chem. Phys* **152,** 124101 (2020).

129. Koskinen, P. & Mäkinen, V. Density-functional tight-binding for beginners. *Comput. Mater. Sci.* **47,** 237 (2009).

130. Porezag, D., Frauenheim, T., Köhler, T., Seifert, G. & Kaschner, R. Construction of tight-binding-like potentials on the basis of density-functional theory: Application to carbon. *Phys. Rev. B* **51,** 12947 (1995).

131. Elstner, M. *et al.* Self-consistent-charge density-functional tight-binding method for simulations of complex materials properties. *Phys. Rev. B* **58,** 7260 (1998).

132. Parr, R. & Yang, W. *Density-Functional Theory of Atoms and Molecules* (Oxford University Press, 1994).

133. Mulliken, R. S. Electronic Population Analysis on LCAO–MO Molecular Wave Functions. I. *J. Chem. Phys.* **23,** 1833 (1955).

134. Fonseca Guerra, C., Handgraaf, J.-W., Baerends, E. J. & Bickelhaupt, F. M. Voronoi deformation density (VDD) charges: Assessment of the Mulliken, Bader, Hirshfeld, Weinhold, and VDD methods for charge analysis. *J. Comput. Chem.* **25,** 189 (2003).

135. Dolgonos, G., Aradi, B., Moreira, N. H. & Frauenheim, T. An improved self-consistent-charge density-functional tight-binding (SCC-DFTB) set of parameters for simulation of bulk and molecular systems involving titanium. *J. Chem. Theory Comput.* **6,** 266 (2010).

136. Wahiduzzaman, M. *et al.* DFTB parameters for the periodic table: Part 1, Electronic structure. *J. Chem. Theory Comput.* **9,** 4006 (2013).

137. Lindsey, R. K., Fried, L. E. & Goldman, N. ChIMES: a force matched potential with explicit three-body interactions for molten carbon. *J. Chem. Theory Comput.* **13,** 6222 (2017).

138. Koziol, L., Fried, L. E. & Goldman, N. Using force matching to determine reactive force fields for water under extreme thermodynamic conditions. *J. Chem. Theory Comput.* **13,** 135 (2017).

139. Goldman, N., Aradi, B., Lindsey, R. K. & Fried, L. E. Development of a multicenter density functional tight binding model for plutonium surface hydriding. *J. Chem. Theory Comput.* **14,** 2652 (2018).

140. Stöhr, M. *Simulation of Hybrid-Organic-Inorganic Interfaces with dispersion-inclusive semi-empirical electronic structure methods* MA thesis (Technische Universität München, Yale University, 2018).

141. Gaus, M., Goez, A. & Elstner, M. Parametrization and benchmark of DFTB3 for organic molecules. *J. Chem. Theory Comput.* **9,** 338 (2013).

142. Knaup, J. M., Hourahine, B. & Frauenheim, T. Initial Steps toward Automating the Fitting of DFTB E rep (r). *J. Phys. Chem. A* **111,** 5637 (2007).

143. Gaus, M., Chou, C.-P., Witek, H. & Elstner, M. Automatized parametrization of SCC-DFTB repulsive potentials: application to hydrocarbons. *J. Phys. Chem. A* **113,** 11866 (2009).

144. Chou, C.-P. *et al.* Automatized Parameterization of DFTB Using Particle Swarm Optimization. *J. Chem. Theory Comput.* **12,** 53 (2016).

145. Krishnapriyan, A., Yang, P., Niklasson, A. & Cawkwell, M. Numerical optimization of density functional tight binding models: application to molecules containing carbon, hydrogen, nitrogen, and oxygen. *J. Chem. Theory Comput.* **13,** 6191 (2017).

146. Kranz, J. J., Kubillus, M., Ramakrishnan, R., von Lilienfeld, O. A. & Elstner, M. Generalized density-functional tight-binding repulsive potentials from unsupervised machine learning. *J. Chem. Theory Comput.* **14,** 2341 (2018).

147. Lozovoi, A., Pashov, D., Sheppard, T., Kohanoff, J. & Paxton, A. Universal tight binding model for chemical reactions in solution and at surfaces. III. Stoichiometric and reduced surfaces of titania and the adsorption of water. *J. Chem. Phys.* **141,** 044505 (2014).

148. Zhechkov, L., Heine, T., Patchkovskii, S., Seifert, G. & Duarte, H. A. An efficient a posteriori treatment for dispersion interaction in density-functional-based tight binding. *J. Chem. Theory Comput.* **1,** 841 (2005).

149. Engelmann, A. *The generation of pairwise interatomic potentials from arbitrary structures - A machine learning approach with application in DFTB* MA thesis (Technical University Munich, 2018).

Appendix

A   Paper 1

DFTB Modeling of Lithium-Intercalated Graphite with Machine-Learned Repulsive Potential

Chiara Panosetti*, Simon Anniés*, Cristina Grosu, Stefan Seidlmayer, and Christoph Scheurer
The Journal of Physical Chemistry A, 2021

Article

DFTB Modeling of Lithium-Intercalated Graphite with Machine-Learned Repulsive Potential

Chiara Panosetti,*,[‖] Simon B. Anniés,[‖] Cristina Grosu, Stefan Seidlmayer, and Christoph Scheurer

Read Online

ACCESS | Metrics & More | Article Recommendations | Supporting Information

ABSTRACT: Lithium ion batteries have been a central part of consumer electronics for decades. More recently, they have also become critical components in the quickly arising technological fields of electric mobility and intermittent renewable energy storage. However, many fundamental principles and mechanisms are not yet understood to a sufficient extent to fully realize the potential of the incorporated materials. The vast majority of concurrent lithium ion batteries make use of graphite anodes. Their working principle is based on intercalation, the embedding and ordering of (lithium-) ions in two-dimensional spaces between the graphene sheets. This important process, it yields the upper bound to a battery's charging speed and plays a decisive role in its longevity, is characterized by multiple phase transitions, ordered and disordered domains, as well as nonequilibrium phenomena, and therefore quite complex. In this work, we provide a simulation framework for the purpose of better understanding lithium-intercalated graphite and its behavior during use in a battery. To address large system sizes and long time scales required to investigate said effects, we identify the highly efficient, but semiempirical density functional tight binding (DFTB) as a suitable approach and combine particle swarm optimization (PSO) with the machine learning (ML) procedure Gaussian process regression (GPR) as implemented in the recently developed `GPrep` package for DFTB repulsion fitting to obtain the necessary parameters. Using the resulting parametrization, we are able to reproduce experimental reference structures at a level of accuracy which is in no way inferior to much more costly *ab initio* methods. We finally present structural properties and diffusion barriers for some exemplary system states.
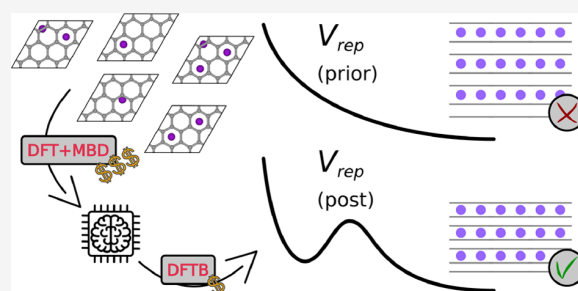
INTRODUCTION

Within the past decade, studies investigating the consequences of man-made climate change[1−3] have become more specific, the predicted time frames shorter, and the warnings more urgent. The immediate and radical reduction of carbon dioxide emissions by replacing fossil fuel-based energy sources with renewable ones has been found to be the only reasonable approach to at least limit those consequences.[4] While the generation of electric energy from wind and sun is already quite advanced and efficient, its storage and transport are the main factors holding it back compared to coal and oil. Currently, two main approaches are being pursued to eliminate these drawbacks. One aims directly at the synthesis of alternative liquid or gas-phase fuels. The other intends to improve upon existing battery technology, especially lithium ion batteries, enough, to make it a serious contender in terms of energy sustenance. In this work, we intend to lay some groundwork for gaining deeper insight into some of the atomistic mechanisms limiting the (dis-)charging speed and lifetime of the most common types of lithium ion batteries, with graphite intercalation anodes.

Ever since graphite was ascertained experimentally and theoretically to be an excellent candidate as an anode for Li-ion batteries, numerous attempts were made at fully describing the

working system.[5−9] Most of the electrochemical properties of the anode material itself are well known. However, in particular, transport processes during strongly driven operating conditions, like fast charging, are only poorly understood at a microscopic level. These technologically important macroscopic conditions are accompanied, *e.g.*, by temperature variations, leading to a capacity fade during ageing, as well as lithium plating. All of the above limit the lifetime of the battery.[10−12] Against this background, experiments and theory are pushed quite far to gain insight into the real processes occurring during the electrochemical operation. Depending on the quantities accessible *via* experiments and theory, two hypotheses are regularly invoked to explain the findings in the range of 0% (graphite) to 100% (LiC_6) state of charge (SOC): the staging and the domain model. The lithium intercalation process shows evidence of multiple phase transitions in the
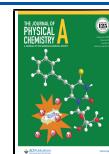
voltage *vs* SOC diagram. The corresponding system configurations are termed "stages" I, II, and so forth. In the simple staging model, these correspond directly to the number of empty galleries (spaces between graphene sheets) between the fully occupied ones (see Figure 1). In the domain model, these
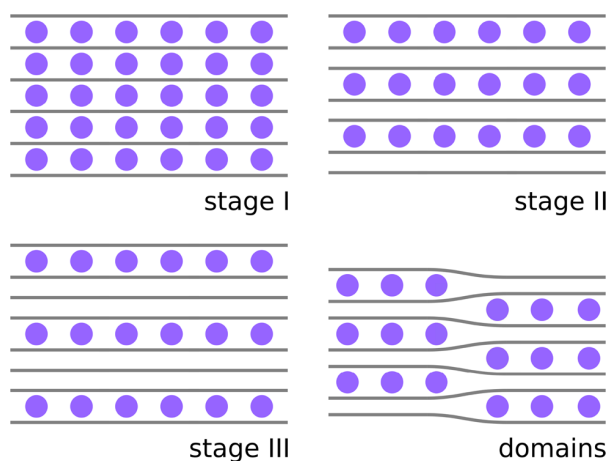

Figure 1. Sketch of Li-intercalated graphite in stage I–III configurations.[13] Violet spheres represent lithium ions; dark gray lines correspond to graphene sheets. Bottom right: illustration of the domain model.[14] The structure has the same nominal stoichiometry as the structure in stage II (top right).

motifs are not assumed to range over meso-/macroscopic dimensions but to form regions of finite lateral extent. Consequently, it is quite clear that different SOC with the same nominal stoichiometry LiC_x will not be configurationally homogeneous, making Li-intercalated graphite a profoundly nontrivial system to address.

To effectively connect to experimental studies, a theoretical framework for simulating large-scale and long-duration nonequilibrium processes in the graphite anode, based on kinetic Monte Carlo (kMC)[15] simulations, is required. The first step toward this goal is gaining the ability to quickly and accurately calculate diffusion barriers on the fly, which is the primary motivation of this work. This requires the ability to reproduce reliably and accurately layer distances (ideally of all possible configurations but predominantly of dilute, low-saturation stages) and the forces affecting the lithium ions, while the strains within the graphene layers are of lesser importance.

Large-scale atomistic simulations typically pursue force field approaches[16] for those systems where energetics and kinetics are well described within the upper end of the SOC range. However, those approaches are limited when it comes to the entire range of different SOC, from extremely diluted stages to fully concentrated ones. Recently, a Gaussian approximation potential (GAP) was reported to be able to describe amorphous carbon well.[17] However, when the latter was later extended to model lithium intercalation,[18] it became apparent that the insertion of lithium into those host structures requires a nontrivial description of the electrostatic interaction. Contrary to most approaches, including the one presented in this work, Fujikake et al. did not treat the full Li−C system but attempted to model the energy and force differences arising from lithium intercalation separately and then added them to the carbon GAP. More specifically, their machine learning (ML) process is based on fitting the energy and force

differences between identical carbon host structures but with and without an intercalated lithium atom. However, due to the fact that lithium intercalation energies are significantly larger in magnitude than electrostatic lithium−lithium interaction energies, they were not able to recover the latter from the data to a satisfactory degree and had to manually add an extra correction term (fitted to density functional theory (DFT)) to account for those contributions. To avoid similar shortcomings, we rather base our approach on density functional tight binding (DFTB),[19] a semiempirical, and thus computationally much cheaper, approximation to density functional theory (DFT),[20] which has been the most common technique for high-accuracy electrochemical simulations for many decades.[21] However, since the DFTB's speedup is achieved by precalculating atomic interactions to avoid expensive integrations at runtime, this comes at the cost—or rather, initial investment—of pairwise parametrization. As of now, no Li−Li and Li−C DFTB parameters are available. In the following, we combine for the first time the recently developed particle swarm optimization (PSO)[22] parametrization approach as first proposed by Chou et al.[23] with a more flexible ML repulsive potential,[24] obtained with Gaussian process regression (GPR) as implemented in the recently developed `GPrep` package,[25] to obtain finely tuned parameters for this system—taking advantage of its physics, albeit perhaps at the expense of some transferability. Let us however stress that the parametrization procedure employed here remains completely general, as the system specificity lies entirely in the choice of the training set(s).

■ METHODS

DFTB: Electronic Part. In DFTB jargon, the so-called "electronic part" includes the semiempirical band structure and the Coulombic contributions to the total energy of the system.[21] These depend parametrically on the diagonal elements ϵ of the noninteracting Hamiltonian, the Hubbard-*U*, and a confinement potential which is used to cut off the diffuse tails of the basis orbitals. For the free atom, the first two quantities are tabulated for most elements or can be calculated with DFT. However, using the free atom values is an approximation, and the decision whether it is justified must be made carefully on a case-to-case basis. The confinement potential, on the other hand, is always treated as a parameter. Quadratic[26] and general power-law functional forms[27] are commonly used, as well as the Woods−Saxon potential[23] (also employed here), which assures a smoother transition to zero in the orbital tails. Each of these parameters needs to be determined for every chemical species present in the system of interest, typically in a nonlinear optimization process. In the PSO, each particle then represents a set of parameters ($\{\epsilon\}$, $\{U\}$, and the confinement constants), with which the DFTB interaction is constructed, so that the parametrization can be improved by minimizing a cost function. The central task is thus the definition of a meaningful cost function. Frequently, one uses the weighted sum of an arbitrary number of contributions $f(\sigma^{DFT}, \sigma^{DFTB})$, each providing a measure of the deviation between DFT and DFTB for some system property σ. Hereby, as we are optimizing the electronic parameters only, the chosen target properties must not depend on repulsion. For our system, we target the band structures of metallic lithium, graphene, and diamond. Additional details on the definition of the corresponding cost function, as well as the resulting optimal values of the onsite energies ϵ and the
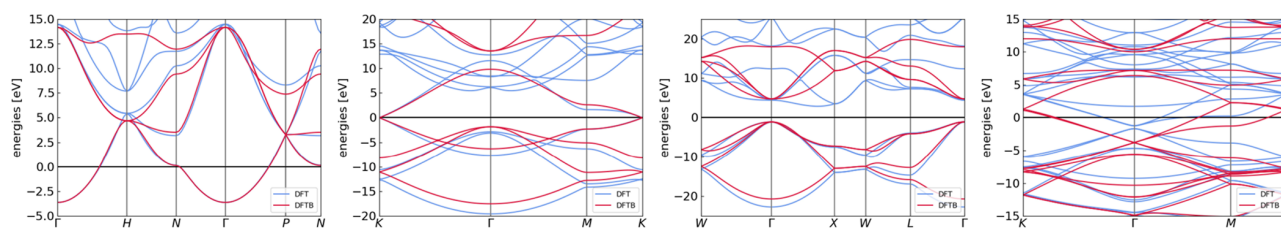
Figure 2. Comparison of band structures calculated with Perdew−Burke−Ernzerhof (PBE)-DFT (blue) and our DFTB electronic part parameters (red) for metallic lithium, graphene, diamond, and LiC_6 (left to right). The latter was not part of our cost function and serves as validation. All of the band structures are shifted to the respective DFT Fermi levels.

confinement coefficients, are provided in the Supporting Information (SI). Figure 2 shows our resulting band structures. Overall, we recognize decent agreement for all band structures, while some deviations are expected given the minimal basis in DFTB. For example, the pronounced mismatch in the conduction band at the H point in the lithium band structure as well as the incorrectly direct band gap of diamond can be ascribed to this oversimplification in the DFTB model. For the two carbon systems, we see very good qualitative agreement for most regions of the band structures but notice a small degree of overall compression toward the Fermi level.

Given the overall agreement and also considering the fact that the repulsion potential is capable of quite effectively correcting small imperfections in the electronic part, we decide not to optimize the latter any further in this work, a decision justified in retrospect by the excellent results we present. However, let us still emphasize the opportunity for improvement here, should it eventually become necessary.

From a more technical standpoint, we note in passing that while during the PSO optimization we employed an {sp} basis set for lithium, the production Slater Koster (SK) table was constructed including only the s orbital for lithium (with the confinement optimized in the {sp} basis). While this may strike as a rather unorthodox choice, it is motivated by the concomitant observation that (i) optimizing the lithium confinement with the s orbital only produces inherently wrong results, and (ii) the optimization of the repulsive potential on top of an {sp}-basis electronic part showed inherent pitfalls that likely cannot be overcome by any choice of training set. A detailed justification is provided in the SI.

DFTB: Repulsive Potential. It is common practice to assume some analytical form for the repulsive potential and fit the functional parameters as to minimize a set of DFT-DFTB force differences,[21] a protocol easily implemented also for the PSO approach. However, limitations and bias may result from the choice of said parametrized functional form. It needs to be sufficiently flexible to cover a large space of systems and bonding situations. This typically yields a high-dimensional nonlinear optimization problem, which might still be insufficient to capture unexpected subtle, yet extremely relevant physical features. We rather adopt the GPrep method recently developed in our group,[24,25] which employs Gaussian process regression (GPR)[28] to create a flexible functional form "on the fly", while adapting to the physics captured by the training data set, instead of forcing us to guess it *a priori*. In the SI, we give a short introduction to the method and explain the character and effect of the related hyperparameters, referring the reader to Rasmussen[28] for the underlying stochastic theory and to refs 24 and 25 for the application to DFTB repulsive potentials. For the global damping, correlation distance, and data noise hyperparameters,

we verified (see the SI) that results are appropriately robust in a sizeable subspace of the overall hyperparameter space. The same is not necessarily true for the cutoff radii R_{cut}. Since the electronic energy contribution is entirely based on just a sum of noninteracting atomic contributions, the repulsion potential has to account for different chemical environments affecting the same type of atom. In a GPR setting, it is therefore of paramount importance to sample a sufficiently large set of training data that covers all interatomic distance ranges and chemical environments relevant for a faithful representation of the system studied. Ideally, it should also be ascertained that the model quality is stable with respect to (wrt) the explicit choice of the cutoff radii as well as the other hyperparameters, at least within physically motivated boundaries roughly defined by characteristic lengths of the system, *e.g.*, nearest neighbor (NN) distances. For instance, it is generally accepted that adequate V_{rep} cutoff values should fall somewhere between the first and the second NN distances for the pair in consideration.[21] However, V_{rep} may extend to include ranges beyond the second NN distance, should the particular physics the parametrization is aimed at not be entirely captured by shorter-ranged repulsive potentials.

RESULTS AND DISCUSSION

DFTB Repulsion Training. In terms of DFT functional, our starting point is PBE,[29] which has been used by the majority of researchers working on intercalation phenomena and is known to describe LiC_6 well. However, it does not reproduce the dispersive interaction between graphene sheets. To address this, we finally (see "set 3" below) combine the reference PBE calculation with a many-body dispersion (MBD@rsSCS, throughout the text referred to as MBD)[30,31] treatment and the DFTB model with a computationally cheap Lennard-Jones (LJ)[32] dispersion correction.[33] The rationale for this choice is that PBE should reproduce galleries containing many lithium atoms correctly and LJ dispersion should predict empty galleries well while not interfering too much with the PBE description of the concentrated ones. However, it is unclear, how this interaction shapes out for intermediate, dilute lithium stoichiometries. During our investigations, we find that this approach works somewhat decently but needs some controlled adjustments (*vide infra*) to produce truly satisfactory results.

As a first guess, we construct a set of training structures (set 1) that consists of a balanced mix of Li_nC_{36} supercells ($n \in$ (0, 1, ..., 6)), to represent the entire range of charging states. Additionally, those structures are rattled (each atom randomly displaced), as well as compressed or expanded. This procedure yields a smooth distribution of bond lengths and forces. We then train a GPR repulsion potential by matching DFTB

against PBE forces for this structural ensemble, aiming at a first, mostly transferable model. The standard LJ DFTB correction is subsequently applied on top of this parametrized DFTB model. With this approach, we are able to find parametrizations that reproduce all layer distances (of graphite, LiC_{12}, and of LiC_6) correctly, albeit not for a stable range of all parameters.

As shown in Figure 3, the choice of cutoff radius R_{cut}^{CC} for the C−C repulsion potential does not have a major influence on
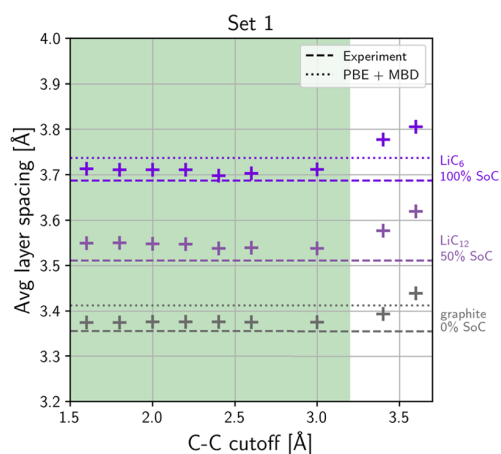

Figure 3. Interlayer distances for graphite (gray), LiC_{12} (SOC 50%, gray-purple), and LiC_6 (SOC 100%, purple) as a function of R_{cut}^{CC}. Note that for LiC_{12} there are two different layer distances to consider: one for the empty gallery and one for the full gallery. Here, we plot the average of the two. The dashed lines show the experimental layer distances we aim to reproduce, as in Trucano et al.[34] (graphite) and Vadlamani et al.[35] (LiC_{12} and LiC_6). The green colored area represents the range within which the absolute deviation between the DFTB value and the experimental reference is smaller than 0.06 Å.

the layer distances for quite a large range of values. In fact, the point at which the predictions stop being accurate can be identified as approximately the experimental values for the interlayer distances. Going beyond that with the cutoff radius essentially corresponds to including interlayer interactions in the potential fit, mixing their description with intralayer covalent bonds. Thus, the restriction of the cutoff radius we find here is physically motivated by the range separation of the interactions that characterize our system: as the second next-neighbor distance in a relaxed graphene sheet is around 2.45 Å and the layer distance is 3.35 Å, the cutoff range defined by the plateau in Figure 3 represents a sweet spot where the GPR learns second next-neighbor interactions but does not yet (mistakenly) take any interlayer interactions (even in the compressed structures) into account in the repulsion potential. However, the same reasoning does not apply to CC bond lengths, which are not correctly reproduced if the GPR learns forces beyond the first NN distance (see the SI). In light of these findings, we select the cutoff value of 2.2 Å for the C−C-repulsion potential. Indeed, we did not encounter any reason to change this selection during the entirety of this work (despite rigorously testing it for each of the training data sets).

However, with this first training set, we do not obtain an equally stable plateau as a function of the Li−C repulsive cutoff (see the SI), with the correct values corresponding to $R_{cut}^{LiC} = 4.0$ Å not belonging to a plateau at all. Furthermore, quite strongly distorted graphite planes in these structures lead to

large forces compared with those acting on intercalated lithium ions, causing a systematic underestimation in lithium force prediction. We tackle the second problem first: while the rattled, scaled structures in set 1 cover a sufficiently large range of bond lengths, they only account for configurations with the lithium ions sitting over the center of a graphite ring, i.e., in a local energy minimum. We recognize this as the reason for the comparably small lithium forces. To balance out this structural bias, we calculate a number of transition paths for lithium diffusion processes in LiC_6 and LiC_{12} stage I/II compounds using a nudged elastic band (NEB) method.[36,37] We are now able to extract structures from these trajectories, in which the lithium ions are subject to stronger forces commensurable with the graphite layers. For our second training set (set 2), we replace higher-saturated rattled and scaled structures with those extracted from the transition paths. In doing so, we assume higher-saturated structures to be responsible for the slight contraction observed in C−C bonds (see the SI).

By this measure, we are able to improve the accuracy for predicting forces on Li ions significantly (albeit still slightly underestimated), without sacrificing the description of the graphite layers. However, while we do observe a plateau for the resulting layer distances with respect to R_{cut}^{LiC}, the interlayer distances are not reproduced equally well as in Figure 3 for set 1 (see Figure 4, yellow area), with the exception of points 3.5
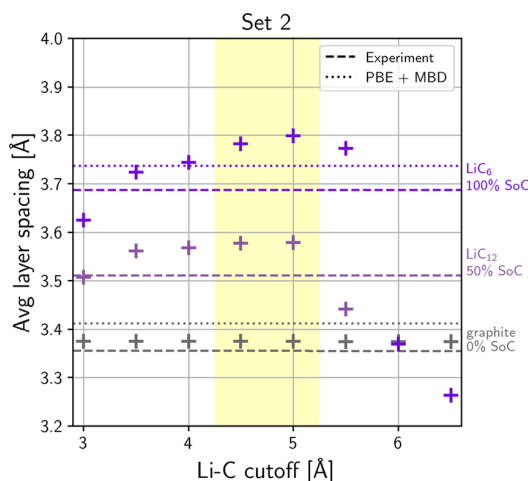

Figure 4. Interlayer distances for LiC_{12} (SOC 50%, gray-purple) and LiC_6 (SOC 100%, bright purple) as a function of R_{cut}^{LiC}, with a fixed R_{cut}^{CC} set to 2.6 Å. The repulsion was trained on a set analogous to set 1 (cf. text), where the higher-saturated structures were replaced by geometries randomly extracted from intralayer Li diffusion paths. For LiC_{12}, the plotted interlayer distance is the average between the values for the filled and the empty gallery. The dashed lines show the experimental layer distances. The yellow colored area represents the range within which the results are stable, however at a wrong value.

and 4.0 Å which do not belong to a plateau. This behavior suggests that our problem here does not lie in the choice of the training set but rather in the treatment of long-ranged interactions.

Let us consider the underlying predicament: so far, the DFTB part of the force residues used for the ML process is calculated without LJ dispersion correction. We then construct the repulsion potential with the purpose of making those DFTB calculations match references based on PBE-DFT, which reliably predicts layer distances for LiC_6. By then using

LJ (required to obtain the correct empty layer distance in graphite) in our actual DFTB calculations (after the parametrization process), we cause the aforementioned offset for highly lithiated compounds. Using LJ already for the force-residue calculations during the ML seems like the obvious solution to this problem. However, this presents a new issue in the lower-saturation range (LiC_x, $x > 12$). There, we previously fitted the repulsion to PBE-DFT references, which are not correct in that range without dispersion correction. The resulting DFTB forces are then shifted by LJ toward the correct value (as is indicated by the quite decent results for LiC_{12} with set 2). However, after the modification, we would then fit the final DFTB forces (that result after applying the LJ) to the (incorrect) PBE-DFT references, thus improving our performance for highly saturated system states, but ruining it for dilute ones, by effectively double-counting dispersive contributions. It becomes apparent that to make this approach work, we need to utilize dispersion-corrected DFT reference forces that are also correct for low-saturation states and, at the same time, compatible with the computationally cheap DFTB-LJ correction.

Our ansatz is that we can, to a degree, encode the difference between the LJ dispersion and the "true" dispersion into the repulsion potential. At this point, we stress that ideally, both the true, nonlocal exchange−correlation functional in DFT and an ideal repulsion energy in DFTB would already encompass all dispersion effects, and it is solely due to approximations in the derivations, e.g., of generalized gradient approximations (GGAs), that they do not in these models. Therefore, rather than mixing our repulsion potential with something fundamentally different (which would be physically questionable), what we do here simply corresponds to partially adding back a contribution that should have been there in the first place. To our knowledge, the currently best way to calculate dispersion-corrected lithium-intercalated graphite, with correct layer distances predicted for the entire saturation range, is the many-body dispersion (MBD) correction.[30,31] This method is computationally rather expensive, but since we only need to run DFT calculations for our training data set, which is very limited in size, this is not vital to us.

In practical terms, we then build a set 3 where DFTB-DFT force residues are replaced by DFTB(LJ)-DFT(MBD) force residues. We do realize that this approach most likely comes with some cost in terms of transferability. To retain as much of it as possible, we choose not to replace all force residues, but only ≈66% (more precisely, only for structures containing no or one lithium atom), which proves sufficient to demonstrate the effectiveness of the presented method in a general way. Nonetheless, further investigating the effect this percentage has on the performance is certainly a task that should be tackled in the future. Of course, alternatively to our approach, it is possible to simply apply the MBD correction scheme directly to our DFTB calculations. However, doing so would cost us 1−2 orders of magnitude in speed, as MBD then becomes the computationally dominating step in production DFTB calculations.

Using the previously explained modifications, we have succeeded at shifting the predicted interlayer distances (within the stable R_{cut}^{LiC} plateau) into the very close proximity of the experimental reference values for both LiC_6 and LiC_{12}, as shown in Figure 5. To be precise, the ranges of R_{cut}^{LiC} = ∼3.3−4.3 and ∼4.3−5.3 Å should be regarded as two distinct plateaus, both close to the correct experimental values.
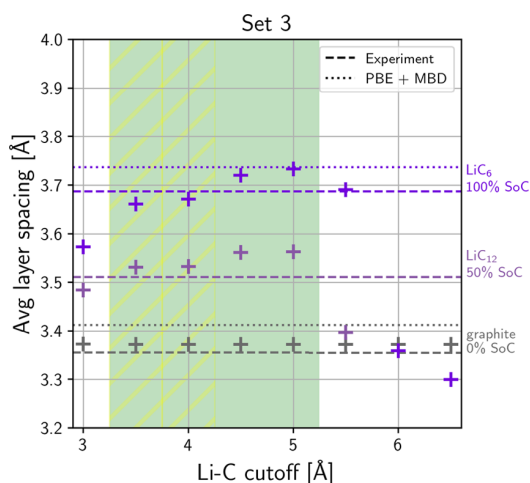

Figure 5. Interlayer distances for LiC_{12} (SOC 50%, gray-purple) and LiC_6 (SOC 100%, bright purple) as a function of R_{cut}^{LiC}, with a fixed R_{cut}^{CC} set to 2.6 Å. The repulsion was trained on a set analogous to set 2 (cf. text), where 70% of the structures were replaced by geometries with MBD-corrected forces. For LiC_{12}, the plotted interlayer distance is the average between the values for the filled and the empty gallery. The dashed lines show the experimental layer distances. The yellow-hatched area represents a range within which the results are stable and correct; however, we consider them not ideal.

However, we shall consider the second as our final plateau, where the resulting interlayer distance falls between the experimental and the DFT reference values, since we trained against DFT reference forces. Of note, the predicted interlayer distance for LiC_{12} becomes wrong already at R_{cut}^{LiC} = 5.5 Å. Once again, this is a physically motivated boundary: it is the distance at which Li atoms start to "feel" the next layer. In LiC_6, which has a larger interlayer spacing and for which the resulting interlayer distance is correct at that point, this happens for R_{cut}^{LiC} > 5.5 Å.

Especially the excellent results for the stage II compound LiC_{12} show that our parametrization is now able to handle both mainly ionic concentrated and mainly dispersive dilute layers to a satisfactory degree. In Figure 6, we illustrate the effect our modification has on the repulsion potential landscape for a wide range of Li−C cutoff radii. First (and most notably), we have moved and solidified the local minimum related to the next-neighbor lithium−carbon interaction (see bottom right). For the set 2 and set 3 potentials, the minima (black and green dashed lines, respectively) are located at atomic distances of 2.33 and 2.30 Å, respectively, which correspond to LiC_6 interlayer distances of 3.80 and 3.73 Å, the exact values which do, in fact, result from the relaxation of those structures, using the two repulsion potentials, respectively. The two-dimensional (2D) maps (top) show that this behavior is apparent for an entire range of cutoff radii, thus ruling out the possibility that the fit is only accidentally correct (as it happens, e.g., for set 1 with R_{cut}^{LiC} = 4.0 Å). We can also clearly see the upper (∼5.3 Å) and lower (∼4.3 Å) boundaries for the cutoff radius, beyond which the physicality of the model falls apart. They define exactly the range within which we find the stable cutoff dependency plateau, which is now at the correct numerical value, as shown in Figure 5. We may identify the upper boundary at 5.3 Å (as discussed above), as the distance between a lithium ion and the second closest graphene sheet, which is an intuitively plausible
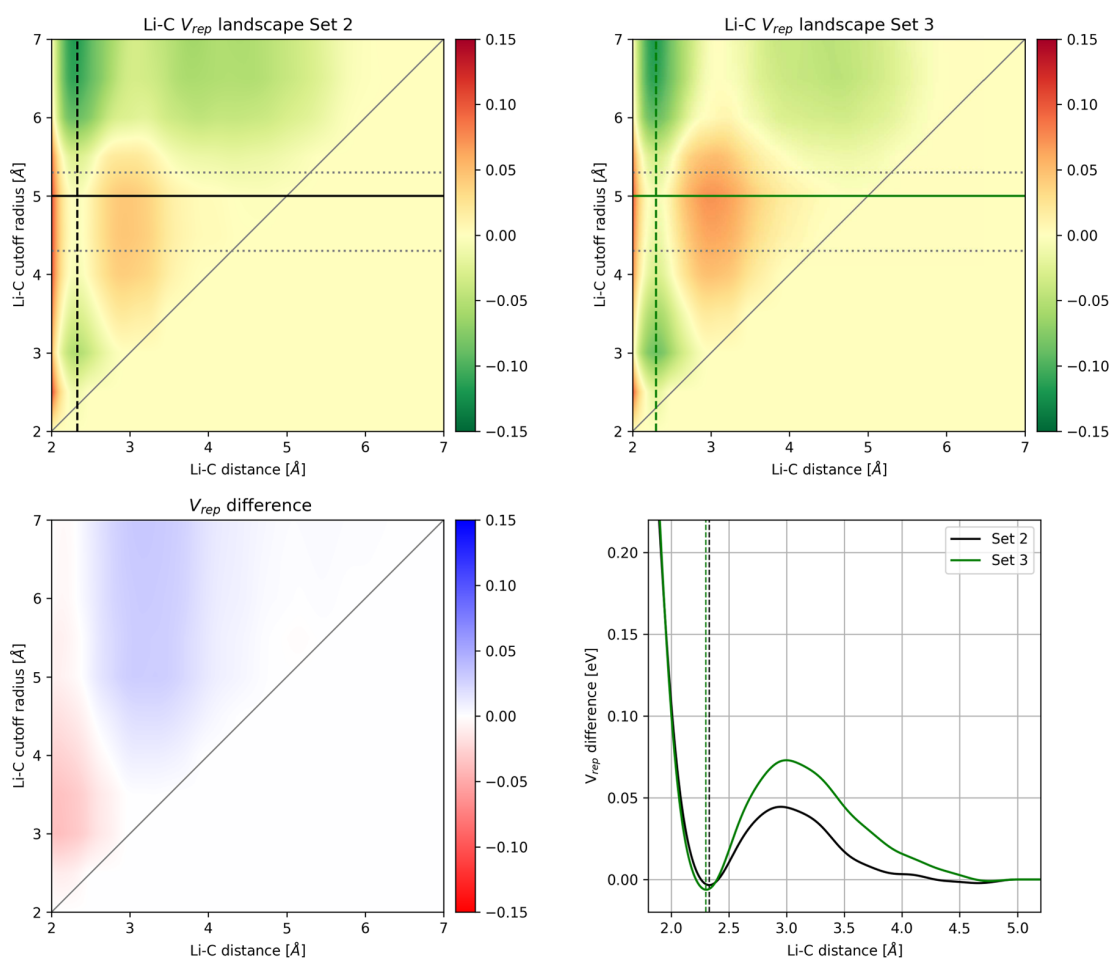
Figure 6. Top: 2D repulsion potential landscape (units eV, expressed by the color bar) depending on the chosen Li−C cutoff radius (*y*-axis) for set 2 (left) and set 3 (right). The black and green dashed lines represent the next-neighbor Li−C distances for sets 2 and 3, respectively. The diagonal lines illustrate the cutoff radii, at which the potential is set to zero. The plateaus are highlighted between thin dotted lines. Bottom: (left) influence of the inclusion of MBD *vs* LJ force residues in the training data on the repulsion potential (units eV, expressed by the color bar). (Right) Detailed repulsion potentials at $R_{cut}^{LiC} = 5.0$ Å.

Table 1. Summary of the Interlayer Distances[a]

	compound	experimental (Å)	DFTB (mÅ)	DFT (mÅ)[38]	filled (mÅ)	empty (mÅ)	barrier (meV)
		(average) interlayer distances with detailed analysis of layer spacing and barriers.					
graphite		3.355[34]	+17	+62		+17	
LiC_{18}	stage III	3.470[c]	+35	+173	+198[b]	−98[b]	468
LiC_{12}	stage II	3.511[35]	+52	−16	+148[b]	−147[b]	480
LiC_6	stage I	3.687[35]	+46	+56	+46		503

[a]We compare interlayer distances resulting from our DFTB parametrization (via structure optimization using the BFGS algorithm[39]) with experimental values, where available. For stage II and III compounds, we consider the average layer distance. We show the relative deviation of our results and compare them with those computed by Krishnan et al.[38] [b]Note that these numbers are not errors but differences between specific and average layer distances [c]Estimated from experimental values for graphite and LiC_6, assuming the filled gallery and the empty galleries to have the same interlayer spacing as LiC_6 and graphite, respectively.

limitation. It is less obvious, though, to assign a clear physical meaning to the lower bound at 4.3 Å, as it cannot be directly related to any particular structural feature of LiC_x. The most likely cause, we believe, is that the cosine-shaped cutoff function employed in the GPR framework starts cutting off physically relevant details from the repulsion potential below that.

A physically motivated lower bound of different nature may be identified by evaluating the relative root-mean-square

deviation (RMSD) of forces as a function of Li−C cutoff, shown in the SI. Overall, we now observe two separate Li−C cutoff plateaus: between approximately 4.3 and 5.3 Å, we obtain accurate layer distances (Figure 5), while for radii above roughly 4.0 Å and until 6.0 Å, our predictions for forces and transition energies are correct. This duality can very simply be explained by the fact that the first property is mostly a *z*-direction phenomenon (and interactions with the second closest graphene sheet limit the physicality of our model),

while the other takes place almost exclusively in the *xy*-plane, where no such limitation applies, hence the broader plateau. Given this difference in fundamental nature, it is very plausible to trust both these plateaus. Thus, their overlap (4.3−5.3 Å) defines the region within which any value of the Li−C cutoff radius produces an almost identical parametrization that performs very well, for all our benchmark criteria, in a stable and trustworthy manner.

Interlayer Distances and Diffusion Barriers. Table 1 reports some resulting interlayer distances and diffusion barriers based on our DFTB parametrization, compared with experimentally determined values, as well as previous theoretical findings. For all calculations, we chose a Li−C cutoff radius of 5.0 Å, following the findings discussed above.

As a quick reminder, stages I, II, and III correspond to every, every other, and every third gallery being filled (to any degree) with lithium. Additionally, one may describe the concentration of the intercalant in a filled gallery as dilute (low) or concentrated (high), thus allowing for a simple classification of fundamentally different compounds. Here, however, we take only concentrated stages into consideration. Therefore, the three states of charge considered here, and the respective elementary diffusion processes (schematically depicted in Figure 7) only differ by the number of empty layers.
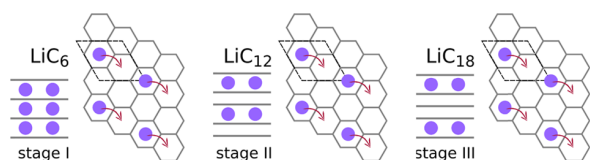

Figure 7. Sketch of some elementary diffusion processes, represented by red arrows, in Li-intercalated graphite in stage I−III configurations. Violet spheres represent lithium ions, and dark gray lines correspond to graphene sheets. The dashed diamond indicates the unit cell.

As Table 1 clearly illustrates, we systematically outperform the method by Krishnan et al.,[38] in terms of accuracy, for every structure they provide comparison for. This is especially remarkable considering the fact that they used full GGA-DFT with dispersion corrections in postprocessing, which is the current state-of-the-art approach, as well as significantly more computationally expensive than our method.

Subsequently, we investigate intralayer next-neighbor diffusion barriers and compare our results to recent experimental findings from ref 40 (based on muon spin relaxation spectroscopy) and theoretical from ref 41 (calculated at the local-density approximation (LDA)-DFT level without dispersion correction, which is only reliable for the predominantly ionic, filled state of charge).

Our calculations yield purely microscopic results within 50 meV from each other for all three relevant compounds, as is shown in Table 1. The deviations between them correlate with the slight differences in the filled-layer spacing of different structures. Our 503 meV barrier for the elementary diffusion in LiC_6 is in perfect agreement with the value of 490 meV reported by Toyoura et al.[41] In contrast, the experimentally determined active barriers of 270 meV for LiC_6 and 170 meV for LiC_{12} show a strong dependency on the system stage.[40] We believe this difference to be caused by concerted effects. Capturing those using kinetic Monte Carlo simulation is something we intend to do in the near future.

CONCLUSIONS

In this work, we put forward, for the first time combining particle swarm optimization (PSO) for the electronic part[23] and machine learning for the repulsion (`GPrep`[24,25]), a well-performing DFTB parametrization for lithium-intercalated graphite which is capable of very accurately reproducing structural properties and qualitative trends in elementary diffusion barriers. The modest computational cost of DFTB will allow us to finally access calculations relating to the intercalation mechanism for LiC_x compounds in the widest range of states of charge, including extremely dilute ones, without sacrificing accuracy. Particularly crucial in this regard is a correct description of dispersion interactions, which for this system, to the best of our knowledge, are consistently captured across all states of charge only by the state-of-the-art many-body dispersion (MBD) approach.[30,31] A careful choice of the training set for `GPrep` allowed us to encode the effect of MBD directly in the pairwise DFTB repulsion, thus saving additional computational cost at runtime.

In the course of this process, we believe to have shown that DFTB is a superior approach for modeling intercalation compared with methods based on classical interatomic potentials or force fields, including the most sophisticated machine learning approaches (*e.g.*, the GAP by ref 18 requires a manual correction term for lithium−lithium electrostatic interactions, which are instead naturally well described by DFTB as employed here). Furthermore, we share key details and choices along this process, showing, *e.g.*, how the choice of the repulsion cutoff is not trivial at all, and thus provide guidance for similar endeavors in the future.

Outlook. Let us conclude with some remarks regarding both perspective applications and future developments. The primary motivation of this work is to ultimately enable a multiscale approach to lithium-intercalated graphite, using DFTB as the *ab initio* energetics driver—or more precisely, a semiempirical surrogate thereof. Among other advantages, DFTB can provide fast and accurate transition barriers for elementary (microscopic) diffusion processes, for the first time accessible in the entire range of states of charge. These can be subsequently used as inputs for kinetic Monte Carlo (kMC) models, to obtain mesoscopic observables, such as electrical impedance[42] or diffusion coefficients, that can be directly compared to experimental data (*e.g.*, spin alignment echo NMR[43,44]). The application of kMC models to battery materials requires a correct treatment of charge transport and polarization phenomena. The necessary methodological adjustments are the subject of ongoing work and will be presented in follow-up publications. Finally, we believe that DFTB shows great promise in the simulation of battery materials in general, thanks to two of its fundamental characteristics: (i) the access to an explicit electronic structure at a fraction of the cost of DFT, and (ii) the correct treatment of long-range electrostatic interactions. Both these qualities are lacking in "conventional" fast-energetics models based on classical interatomic potentials, including the more sophisticated machine-learned ones. In perspective, we thus envision the extension of this parameter set to include not only the Li−Li repulsion but also parameters for the species involved in liquid and/or solid electrolytes and solid electrolyte interfaces (SEI), which are necessary to a full characterization of battery materials along the lines of multiscale modeling as hinted above. We note in passing that DFTB parameters for most

atomic species involved in electrolytes and SEI compounds are already available in, *e.g.*, the `3ob` and `matsci` parameter sets, both available free of charge at `https://dftb.org/parameters/download;` however, there is no guarantee they would perform well for these applications. Nevertheless, one may consider the electronic tabulation of the DFTB interaction as the "transferable" part of the parametrization. In this light, one may adopt the repulsion-less SK tables extracted from the existing DFTB parameters or alternatively use the latter as starting guesses to refine in the PSO, to build new training sets for `GPrep`. Subsequently, more specific chemistry can be targeted "on the fly," exclusively by (re-)training the repulsion. Of note, this procedure is equally valid within a "standard" repulsion fitting approach; however, one of the advantages of `GPrep` is making this step particularly painless. Suitable training sets may, perhaps naively, include molecular dynamics (MD) snapshots, or random displacements, of a representative range of small–medium organic molecules and their complexes with relevant ions, taken as "building blocks" of electrolyte and SEI polymers. Such a training set may or may not be complete enough to capture the complexity of SEI structural features, which are to this day largely unknown but surely would represent an appropriate starting point.

ASSOCIATED CONTENT

Ⓢ Supporting Information

The Supporting Information is available free of charge at https://pubs.acs.org/doi/10.1021/acs.jpca.0c09388.

Computational details, PSO cost function, choice of basis set, `GPrep` hyperparameters, description of training sets, and full validation (PDF)

AUTHOR INFORMATION

Corresponding Author

Chiara Panosetti − *Department of Chemistry, Technische Universität München, 85748 Garching b. München, Germany;* Ⓞ orcid.org/0000-0001-7328-2334; Email: chiara.panosetti@ch.tum.de

Authors

Simon B. Anniés − *Department of Chemistry, Technische Universität München, 85748 Garching b. München, Germany*

Cristina Grosu − *Department of Chemistry, Technische Universität München, 85748 Garching b. München, Germany; Institute of Energy and Climate Research (IEK-9), Forschungszentrum Jülich, 52425 Jülich, Germany*

Stefan Seidlmayer − *Heinz Maier-Leibnitz Zentrum (MLZ), Technische Universität München, 85748 Garching b. München, Germany*

Christoph Scheurer − *Department of Chemistry, Technische Universität München, 85748 Garching b. München, Germany;* Ⓞ orcid.org/0000-0002-7227-8672

Complete contact information is available at:
https://pubs.acs.org/10.1021/acs.jpca.0c09388

Author Contributions

‖C.P. and S.B.A. contributed equally to this work.

Notes

The authors declare no competing financial interest.

REFERENCES

(1) Sharp, M.; Burgess, D. O.; Cogley, J. G.; Ecclestone, M.; Labine, C.; Wolken, G. J. Extreme Melt on Canada's Arctic Ice Caps in the 21St Century. *Geophys. Res. Lett.* **2011**, *38*, No. L11501.

(2) Fisher, D.; Zheng, J.; Burgess, D.; Zdanowicz, C.; Kinnard, C.; Sharp, M.; Bourgeois, J. Recent Melt Rates of Canadian Arctic Ice Caps Are the Highest in Four Millennia. *Global Planet. Change* **2012**, *84–85*, 3–7.

(3) U.S. Global Change Research Program. *Impacts of Climate Change on Human Health in the United States: A Scientific Assessment*; Skyhorse Publishing, 2018.

(4) Anderson, T. R.; Hawkins, E.; Jones, P. D. CO_2, the Greenhouse Effect and Global Warming: from the Pioneering Work of Arrhenius and Callendar to Todayas Earth System Models. *Endeavour* **2016**, *40*, 178–187.

(5) Hennig, G. R. *Progress in Inorganic Chemistry*; John Wiley & Sons, Inc., 1959; pp 125–205.

(6) Guerard, D.; Herold, A. Intercalation of Lithium into Graphite and Other Carbons. *Carbon* **1975**, *13*, 337–345.

(7) Hawrylak, P.; Subbaswamy, K. R. Kinetic Model of Stage Transformation and Intercalation in Graphite. *Phys. Rev. Lett.* **1984**, *53*, 2098–2101.

(8) Conard, J.; Nalimova, V. A.; Guerard, D. NMR Study of LiC_X Graphite Intercalation Compounds Prepared Under High Pressure. *Mol. Cryst. Liq. Cryst. Sci. Technol., Sect. A* **1994**, *245*, 25–30.

(9) Nitta, N.; Wu, F.; Lee, J. T.; Yushin, G. Li-Ion Battery Materials. *Mater. Today* **2015**, *18*, 252–264.

(10) Gallagher, K. G.; Trask, S. E.; Bauer, C.; Woehrle, T.; Lux, S. F.; Tschech, M.; Lamp, P.; Polzin, B. J.; Ha, S.; Long, B.; et al. Optimizing Areal Capacities through Understanding the Limitations of Lithium-Ion Electrodes. *J. Electrochem. Soc.* **2016**, *163*, A138–A149.

(11) Wandt, J.; Jakes, P.; Granwehr, J.; Eichel, R. A.; Gasteiger, H. A. Quantitative and Time-Resolved Detection of Lithium Plating on Graphite Anodes in Lithium Ion Batteries. *Mater. Today* **2018**, *21*, 231–240.

(12) Yang, X.-G.; Zhang, G.; Ge, S.; Wang, C.-Y. Fast Charging of Lithium-Ion Batteries at All Temperatures. *Proc. Natl. Acad. Sci. U.S.A.* **2018**, *115*, 7266–7271.

(13) Smith, R. B.; Khoo, E.; Bazant, M. Z. Intercalation Kinetics in Multiphase-Layered Materials. *J. Phys. Chem. C* **2017**, *121*, 12505–12523.

(14) Daumas, N.; Herold, A. Relations between Phase Concept and Reaction Mechanics in Graphite Insertion Compounds. *C. R. Seances Acad. Sci., Ser. C* **1969**, *268*, 373.

(15) Andersen, M.; Panosetti, C.; Reuter, K. A Practical Guide to Surface Kinetic Monte Carlo Simulations. *Front. Chem.* **2019**, *7*, No. 202.

(16) van Duin, A. C. T.; Dasgupta, S.; Lorant, F.; Goddard, W. A. ReaxFF: A Reactive Force Field for Hydrocarbons. *J. Phys. Chem. A* **2001**, *105*, 9396–9409.

(17) Deringer, V. L.; Csányi, G. Machine Learning Based Interatomic Potential for Amorphous Carbon. *Phys. Rev. B* **2017**, *95*, No. 094203.

(18) Fujikake, S.; Deringer, V. L.; Lee, T. H.; Krynski, M.; Elliott, S. R.; Csányi, G. Gaussian Approximation Potential Modeling of Lithium Intercalation in Carbon Nanostructures. *J. Chem. Phys.* **2018**, *148*, No. 241714.

(19) Elstner, M.; Porezag, D.; Jungnickel, G.; Elsner, J.; Haugk, M.; Frauenheim, T.; Suhai, S.; Seifert, G. Self-Consistent-Charge Density-Functional Tight-Binding Method for Simulations of Complex Materials Properties. *Phys. Rev. B* **1998**, *58*, 7260–7268.

(20) Kohn, W.; Sham, L. J. Self-Consistent Equations Including Exchange and Correlation Effects. *Phys. Rev.* **1965**, *140*, A1133−A1138.

(21) Koskinen, P.; Mäkinen, V. Density-Functional Tight-Binding for Beginners. *Comput. Mater. Sci.* **2009**, *47*, 237−253.

(22) Shi, Y.; Eberhart, R. In *A Modified Particle Swarm Optimizer*, 1998 IEEE International Conference on Evolutionary Computation Proceedings, IEEE World Congress on Computational Intelligence, Cat. No. 98TH8360, 1998.

(23) Chou, C.-P.; Nishimura, Y.; Fan, C.-C.; Mazur, G.; Irle, S.; Witek, H. A. Automatized Parameterization of DFTB Using Particle Swarm Optimization. *J. Chem. Theory Comput.* **2016**, *12*, 53−64.

(24) Engelmann, A. The Generation of Pairwise Interatomic Potentials from Arbitrary Structures—A Machine Learning Approach with Application in DFTB. M.Sc. Thesis, Technical University Munich, 2018.

(25) Panosetti, C.; Engelmann, A.; Nemec, L.; Reuter, K.; Margraf, J. T. Learning to Use the Force: Fitting Repulsive Potentials in Density-Functional Tight-Binding with Gaussian Process Regression. *J. Chem. Theory Comput.* **2020**, *16*, 2181−2191.

(26) Stöhr, M. Simulation of Hybrid-Organic-Inorganic Interfaces with Dispersion-Inclusive Semi-Empirical Electronic Structure Methods. M.Sc. Thesis, Technische Universität München, Yale University, 2018.

(27) Wahiduzzaman, M.; Oliveira, A. F.; Philipsen, P.; Zhechkov, L.; van Lenthe, E.; Witek, H. A.; Heine, T. DFTB Parameters for the Periodic Table: Part 1, Electronic Structure. *J. Chem. Theory Comput.* **2013**, *9*, 4006−4017.

(28) Rasmussen, C. E.; Williams, C. I. *Gaussian Processes for Machine Learning*; MIT Press, 2006.

(29) Perdew, J. P.; Burke, K.; Ernzerhof, M. Generalized Gradient Approximation Made Simple. *Phys. Rev. Lett.* **1996**, *77*, 3865−3868.

(30) Tkatchenko, A.; DiStasio, R. A.; Car, R.; Scheffler, M. Accurate and Efficient Method for Many-Body Van Der Waals Interactions. *Phys. Rev. Lett.* **2012**, *108*, No. 236402.

(31) Ambrosetti, A.; Reilly, A. M.; DiStasio, R. A., Jr.; Tkatchenko, A. Long-Range Correlation Energy Calculated from Coupled Atomic Response Functions. *J. Chem. Phys.* **2014**, *140*, No. 18A508.

(32) Zhechkov, L.; Heine, T.; Patchkovskii, S.; Seifert, G.; Duarte, H. A. An Efficient a Posteriori Treatment for Dispersion Interaction in Density-Functional-Based Tight Binding. *J. Chem. Theory Comput.* **2005**, *1*, 841−847.

(33) Rappe, A. K.; Casewit, C. J.; Colwell, K. S.; Goddard, W. A.; Skiff, W. M. UFF, a Full Periodic Table Force Field for Molecular Mechanics and Molecular Dynamics Simulations. *J. Am. Chem. Soc.* **1992**, *114*, 10024−10035.

(34) Trucano, P.; Chen, R. Structure of Graphite by Neutron Diffraction. *Nature* **1975**, *258*, 136−137.

(35) Vadlamani, B.; An, K.; Jagannathan, M.; Chandran, K. S. R. An In-Situ Electrochemical Cell for Neutron Diffraction Studies of Phase Transitions in Small Volume Electrodes of Li-Ion Batteries. *J. Electrochem. Soc.* **2014**, *161*, A1731−A1741.

(36) Henkelman, G.; Jónsson, H. Improved Tangent Estimate in the Nudged Elastic Band Method for Finding Minimum Energy Paths and Saddle Points. *J. Chem. Phys.* **2000**, *113*, 9978−9985.

(37) Henkelman, G.; Uberuaga, B. P.; Jónsson, H. A Climbing Image Nudged Elastic Band Method for Finding Saddle Points and Minimum Energy Paths. *J. Chem. Phys.* **2000**, *113*, 9901−9904.

(38) Krishnan, S.; Brenet, G.; Machado-Charry, E.; Caliste, D.; Genovese, L.; Deutsch, T.; Pochet, P. Revisiting the Domain Model for Lithium Intercalated Graphite. *Appl. Phys. Lett.* **2013**, *103*, No. 251904.

(39) Shanno, D. F. On Broyden-Fletcher-Goldfarb-Shanno Method. *J. Optim. Theory Appl.* **1985**, *46*, 222−231.

(40) Umegaki, I.; Kawauchi, S.; Sawada, H.; Nozaki, H.; Higuchi, Y.; Miwa, K.; Kondo, Y.; MÅnsson, M.; Telling, M.; Coomer, F. C.; et al. Li-ion diffusion in Li intercalated graphite C 6 Li and C 12 Li probed by μ+ SR. *Phys. Chemi. Chem. Phys.* **2017**, *19*, 19058−19066.

(41) Toyoura, K.; Koyama, Y.; Kuwabara, A.; Tanaka, I. Effects of Off-Stoichiometry of LiC6 on the Lithium Diffusion Mechanism and Diffusivity by First Principles Calculations. *J. Phys. Chem. C* **2010**, *114*, 2375−2379.

(42) Lee, E.; Prinz, F. B.; Cai, W. Kinetic Monte Carlo Simulations of Oxygen Vacancy Diffusion in a Solid Electrolyte: Computing the Electrical Impedance Using the Fluctuation-Dissipation Theorem. *Electrochem. Commun.* **2010**, *12*, 223−226.

(43) Langer, J.; Epp, V.; Heitjans, P.; Mautner, F. A.; Wilkening, M. Lithium Motion in the Anode Material LiC6 as Seen via Time-Domain 7Li NMR. *Phys. Rev. B* **2013**, *88*, No. 094304.

(44) Granwehr, J.; Roberts, P. J. Inverse Laplace Transform of Multidimensional Relaxation Data Without Non-Negativity Constraint. *J. Chem. Theory Comput.* **2012**, *8*, 3473−3482.

B Paper 2

Accessing Structural, Electronic, Transport and Mesoscale Properties of Li-GICs via a Complete DFTB Model with Machine-Learned Repulsion Potential

Simon Anniés*, Chiara Panosetti*, Maria Voronenko, Dario Mauth, Cristiane Rahe, and Christoph Scheurer
Materials, 2021

Accessing Structural, Electronic, Transport and Mesoscale Properties of Li-GICs via a Complete DFTB Model with Machine-Learned Repulsion Potential

Simon Anniés [1,†], Chiara Panosetti [1,2,*,†], Maria Voronenko [1], Dario Mauth [1], Christiane Rahe [3] and Christoph Scheurer [2]

1 Department of Chemistry, Technische Universität München, Lichtenbergstr. 4, 85748 Garching, Germany; simon.annies@tum.de (S.A.); maria.voronenko@tum.de (M.V.); dario.mauth@tum.de (D.M.)
2 Fritz Haber Institute of the Max Planck Society, Faradayweg 4-6, 14195 Berlin, Germany; scheurer@fhi.mpg.de
3 ISEA, RWTH Aachen University, Jägerstraße 17-19, 52066 Aachen, Germany; christiane.rahe@isea.rwth-aachen.de
* Correspondence: panosetti@fhi-berlin.mpg.de
† These authors contributed equally to this work.

Abstract: Lithium-graphite intercalation compounds (Li-GICs) are the most popular anode material for modern lithium-ion batteries and have been subject to numerous studies—both experimental and theoretical. However, the system is still far from being consistently understood in detail across the full range of state of charge (SOC). The performance of approaches based on density functional theory (DFT) varies greatly depending on the choice of functional, and their computational cost is far too high for the large supercells necessary to study dilute and non-equilibrium configurations which are of paramount importance for understanding a complete charging cycle. On the other hand, cheap machine learning methods have made some progress in predicting, e.g., formation energetics, but fail to provide the full picture, including electrostatics and migration barriers. Following up on our previous work, we deliver on the promise of providing a complete and affordable simulation framework for Li-GICs. It is based on density functional tight binding (DFTB), which is fitted to dispersion-corrected DFT data using Gaussian process regression (GPR). In this work, we added the previously neglected lithium–lithium repulsion potential and extend the training set to include superdense Li-GICs (LiC_{6-x}; $x > 0$) and lithium metal, allowing for the investigation of dendrite formation, next-generation modified GIC anodes, and non-equilibrium states during fast charging processes in the future. For an extended range of structural and energetic properties—layer spacing, bond lengths, formation energies and migration barriers—our method compares favorably with experimental results and with state-of-the-art dispersion-corrected DFT at a fraction of the computational cost. We make use of this by investigating some larger-scale system properties—long range Li–Li interactions, dielectric constants and domain-formation—proving our method's capability to bring to light new insights into the Li-GIC system and bridge the gap between DFT and meso-scale methods such as cluster expansions and kinetic Monte Carlo simulations.

Keywords: lithium-ion batteries; DFTB; Li-GIC; graphite; intercalation; multiscale modeling; diffusion barriers; formation energies; energy materials; machine learning

1. Introduction

Lithium-graphite intercalation compounds (Li-GICs) are the primary anode material for commercial Li-ion batteries with a market share of 98% [1] due to their good volumetric and gravimetric capacities, long cycle life, abundant availability, and low cost. Despite investigations into alternatives such as lithium-metal anodes, graphite and modified-graphite compounds will not be replaced in the foreseeable future, as important EV manufacturers, material suppliers and cell producers have recently announced that graphite-containing composites will mark the state of the art for next-generation lithium-ion batteries [2].

Lithium can intercalate into graphite (in an energetically favorable way) up to a stoichiometry of LiC_6 which is commonly taken as the compound defining the state of charge (SOC) of 100%. Recent studies [1,3] (and references therein) have shown that so-called superdense configurations (LiC_x; $x = 2 - 6$) must also be expected, at least locally, as well under ambient conditions. It has been suggested that doping may have the potential to stabilize these compounds and make them accessible for use in batteries [4].

Between SOC 0% (i.e., graphite) and 100% (LiC_6), the system goes through multiple phase transitions [5,6] between so-called stages ($n = 1, 2, \ldots$) that can be experimentally discriminated. Traditionally, these stages have been interpreted in an idealized structural model to directly correlate with the number of $(n - 1)$ empty layers between each pair of filled layers. According to the Daumas–Heróld domain model [7], these configurations will rather form local islands or domains of unknown size.

During the process of filling the system, the lattice parameter in the z direction changes from 3.355 Å per layer at SOC 0% to 3.687–3.706 Å at SOC 100% [8,9]. Additionally, at some point between 5% and 15% SOC, the graphite structure shifts from AB-stacking to AA-stacking, possibly with intermediate configurations such as AAB or ABC [10,11].

Several characteristics make this system challenging to simulate: firstly, layers filled with Li-ions are governed by electrostatics, whereas empty layers are governed by van der Waals (vdW) interactions. Any reliable model must be able to treat both accurately. Secondly, properties such as domain sizes and low-SOC phenomena require large supercells to be investigated. Furthermore, thirdly, Li-GICs—in the context of Li-ion batteries—are an *active* material. Therefore, not only are energetics important, but so are transport properties such as diffusion barriers.

To date, neither a full DFT approach nor a pure machine learning (ML) approach have proven to be capable of efficiently meeting *all* of these requirements: DFT methods [12–14] are too computationally expensive to treat the size of supercells necessary and allow for extensive sampling, whereas pure machine learning approaches [10,15] usually only predict some of the required properties, but not all of them, since they do not grant access to electronic properties such as band structures and charge transfer. Density functional tight binding (DFTB), however, can be 2–3 orders of magnitude faster than DFT (which is comparable to, e.g., charge-adaptive force fields) while still retaining a physical description of the system's electronic properties [16].

In this work, we thus employed a DFTB approach to calculate the structural and energetic properties necessary for a full description of the Li-GIC at all states of charge including superdense ones beyond LiC_6. This comprises bond lengths, layer spacing, formation energetics, long-range Li–Li interactions, and diffusion barriers, all over a wide range of SOC. Our predictions compare favorably with experimental results [5,6,9,17–23] and state-of-the-art dispersion-corrected DFT [11–14,24,25], wherever available.

2. Materials and Methods

2.1. Computational

For this study, we used the implementation in DFTB+ [16] with the parametrization developed in our group. The corresponding Slater-Koster files are publicly available (see Data Availability Statement). The electronic parameters (in [26], only the confinement potential) were optimized by means of particle swarm optimization (PSO) [27]. In our GPrep approach, the repulsion potential was then fitted using Gaussian process regression (GPR) [28] as described in [26]. The initial parametrization in [26] did not include the Li–Li repulsion. Extending that earlier work, the training set now includes not only a wide variety of Li-GIC configurations between SOC 0% and 100%, but also molecular dynamics (MD) snapshots of lithium metal clusters (cf. Supplementary Information), as well as rattled structures extracted from geometry relaxation pathways of LiC_2 and $LiC_{1.75}$, so that our model can also be used to investigate superdense compounds as well as regions governed by metallic interactions, such as dendritic, mossy, or plated lithium. The GPrep hyperparameters were manually adjusted to reproduce selected properties.

Additional details on how the potential shapes changed between [26] and the present work are provided in the Supplementary Information.

DFT calculations, serving as a reference for the DFTB fit, were performed with the all-electron framework FHI-aims [29] with light settings and default tier-2 basis sets, using the PBE exchange-correlation functional [30]. For dispersion correction, the MBD approach was chosen [31,32]. MD simulations for generating the training set and validation structures were performed in the NVE ensemble at 300 K and 1000 K using the LAMMPS code [33] with the embedded atom method (EAM) potential for alkali metals developed by Nichol and Ackland [34].

Geometries were constructed and analyzed by means of the atomic simulation environment (ASE [35]) which we also used as a base framework for all force and energy calculations, structure relaxations (specifically using the BFGS algorithm as an optimizer [36]), and barrier calculations. For the latter, we employed the nudged elastic band (NEB) [37,38] algorithm with the FIRE-optimizer [39] and climbing image switched on.

For all DFTB calculations, we used a well-converged k-point density of at least 0.1/Å. The SCC-tolerance is 10^{-7}. We employed Fermi filling with a Fermi temperature of 300 K, as well as a Broyden mixer [40] for convergence acceleration with a mixing parameter of 0.5. All of these settings were tested with regard to convergence for the whole range of SOC. As described in [26], our parametrization is meant to be used with the Leonnard–Jones dispersion correction [41] switched on.

2.2. Experimental

Open circuit voltage (OCV) curves were recorded to compare the simulation with real measured values. For this purpose, cells were built with graphite against lithium as well as highly oriented pyrolytic graphite (HOPG) against lithium. The cells from EL-Cell (ECC-Std), comparable to button cells, were used as the housing. A Whatman GF\D was used as the separator and EC:DMC 1:1 with 1 mol/L LiPF6 from Sigma-Aldrich was used as the electrolyte. The graphite electrodes were coated on copper current collectors, whereas the HOPG was used without a current collector. The electron conductivity was sufficient due to its low current rate. The graphite was used in 18 mm blanks, whereas the HOPG was cut into narrow strips with a width of approximately 2 mm to ensure the highest possible surface-to-volume ratio. The ions can only intercalate into the HOPG from the cut edges and not through the surface. The graphite cells were initialized with a current rate of C/10 and the HOPG cells were cyclized with a current rate of C/30.

3. Results and Discussion

3.1. Structural Properties

Graphite consists of graphene sheets, within which the C-atoms are arranged in a hexagonal honeycomb structure. The sheets are stacked in an *AB*-stacking order. The lattice is hexagonal with a 2-layer, 4-atom unit cell and lattice parameters *a* and *c* [42]. In our first benchmark, we compared the performance of our DFTB parametrization with Gaussian process regression-based repulsion potential (GPrep-DFTB) with experimental and recent theoretical findings (Table 1).

Table 1. Lattice parameters *a* and *c* of the *AB*-graphite unit cell, predicted using GPrep-DFTB, compared with experimental results, state-of-the-art dispersion-corrected DFT calculations, and a recently published machine learning model.

Method:	GPrep-DFTB	Experiment			DFT			ML
		(*a*)	(*b*)	(*c*)	(*d*)	(*e*)	(*f*)	(*g*)
$a[\text{Å}]$	2.476	2.464	2.461	2.468	2.465	2.477	2.472	2.461
$c[\text{Å}]$	6.746	6.711	6.709	6.712	6.645	7.087	6.975	7.538

Experimental references: (*a*) [17]; (*b*) [18]; DFT: (*c*) revPBE-D3-BJ [14]; (*d*) optB88-vdW [12]; (*e*) revPBE-vdW [12]; (*f*) vdW-optPBE [43]. Machine learning (ML) reference: (*g*) Atomistic Neural Network [10].

All considered benchmark methods performed well in reproducing the in-plane lattice parameter *a*, which is governed by covalent C–C bonds. However, even state-of-the-art dispersion-corrected DFT functionals (except for [14]) struggle with predicting the out-of-plane lattice parameter *c*. This is due to the fact that the latter is governed by van der Waals interactions, which are still notoriously difficult to account for despite considerable effort in creating various correction schemes [31,44–46] for DFT. The recent machine learning approach [10] overestimates *c* by an even larger margin.

GPrep-DFTB results are very close to the experimental references—closer than even the majority of DFT approaches—proving that the method is very capable of treating both covalent C–C bonds and van der Waals interactions in graphite.

When lithium intercalates into graphite, the graphene sheets shift from *AB*-stacking to *AA*-stacking somewhere between 5% and 15% SOC, and the interlayer distance expands from ~3.36 Å to ~3.62–3.7 Å (depending on the SOC of adjacent galleries) for the full gallery. Empty galleries adjacent to filled galleries also slightly expand, due to the extra charge transferred to the graphene sheet from the intercalated Li-ions, making the overall increase in the average *z* direction lattice parameter non-linear.

It is generally accepted that Li-ions do not evenly distribute throughout the entire GIC, but tend to arrange themselves in fully filled domains and empty domains [7,47] (see Figure 1), leading to a local staging behavior with the staging number ($n = 1, 2, \ldots$) indicating that $n - 1$ galleries are empty between each pair of filled galleries only within that limited region. For our second benchmark, we calculated the average interlayer distances depending on the stage $n = 1, \ldots, 9$ of stoichiometry LiC_{6n} (corresponding to LiC_6, LiC_{12}, LiC_{18}, LiC_{24} and higher) with the GPrep-DFTB and compared with experimental and DFT references, where available (Figure 2 and Table 2).

In order to be able to directly compare with DFT, this set of unit cells was constructed with global staging (Figure 1, left) and not according to the domain model, which would render them far too big for DFT. Because of that, it is not obvious whether *AA*- or *AB*-stacking should be assumed for the empty layers. In *real* samples, which are large of scale and governed by the domain model (Figure 1, right), it is probable that empty parts of galleries also exhibit *AA*-stacking, because they are forced into that configuration by adjacent filled domains within that same gallery and because they are not truly empty, either. However, in an idealized system, without factoring this in (Figure 1, left), *AB*-stacking of the empty galleries (as in pure graphite) is also conceivable. Therefore (and because it is unclear which stacking order has been assumed in the DFT reference [13]), we provide predictions for both as well as a prediction area (light blue). Filled galleries are always in *AA*-stacking.
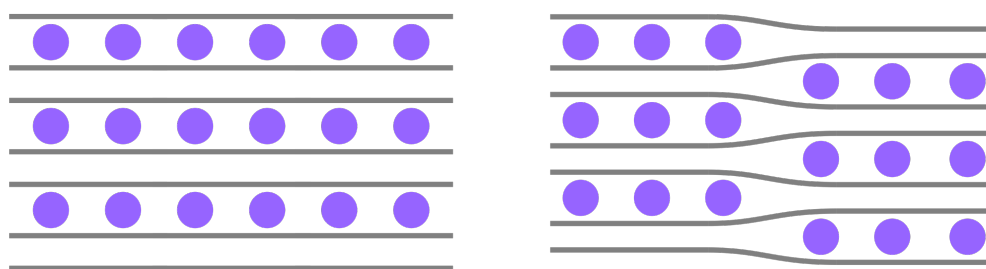

Figure 1. Stage 2 Li-GIC compound (purple: Li-ions, gray: graphene sheets) in a global staging model (**left**) and the Daumas–Heróld domain model (**right**).

For the empty galleries, we predict that interlayer distances remain mostly constant throughout all stages with a slight increase in stage 2, due to the additional electrostatic repulsion caused by the charge transfer from Li-ions in the adjacent filled galleries to the carbon sheets. For the filled galleries, a constant interlayer distance can be observed for stages 4 and higher, whereas stages 3, 2, and 1 progressively show increased interlayer distances, which we attribute again to the electrostatic repulsion of the increasing charge

density. Based on these findings, a simple building block model that assumes invariant interlayer distances proves sufficient to describe the system's behavior in the high-stage ($n > 3$) limit, where filled galleries are too far apart to interact in any way (Figure 2, left: 'fit AA' and 'fit AB'). Only for stages 1 and 2 can the increased filled interlayer distance cause a significant deviation from this model.

Experimental results [5,9] agree very well with our GPrep-DFTB predictions for stages 1, 2, and 3. The DFT-based Ising model by [13] is also accurate for stages 1 and 2, but maintains an overly steep slope for higher stages 3 and 4, which—if continued—would clearly converge towards wrong asymptotic behavior.
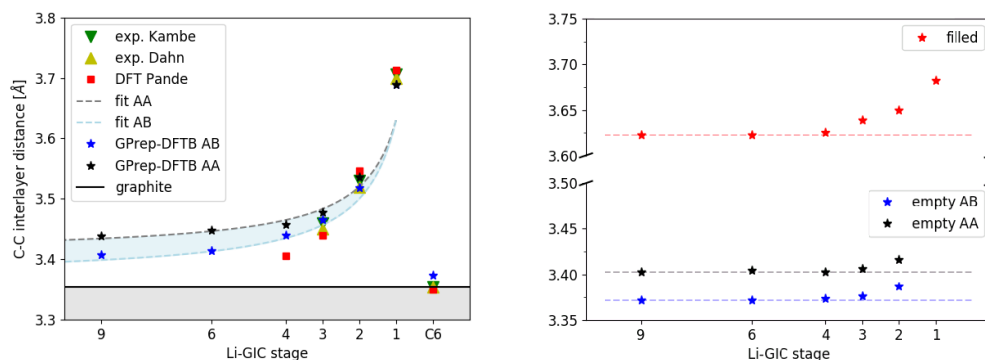

Figure 2. (**Left**): Average C–C interlayer distance in the z direction as a function of the stage of the compound in Å. *AA* and *AB* signifies *AA*-stacking and *AB*-stacking assumed for the *empty* graphite layers. Where available, experimental and theoretical references are also shown. The curves 'fit AA' and 'fit AB' correspond to a simple building block model with just two fixed interlayer distances for empty and filled galleries, respectively. For stages 3 and higher, our predictions adhere closely to that model. For stages 1 and 2, the interlayer spacing of the filled galleries was expanded due to the additional charge transfer. (**Right**): Interlayer spacing of the full galleries, as well as empty galleries in *AA* and *AB* stacking, as a function of the stage (calculated with GPrep-DFTB).

Table 2. C–C interlayer distances in Å. For details, see the caption of Figure 2.

		DFTB		Experiment		DFT
	Filled	**Empty** *AA*/*AB*	**Avg.** *AA*/*AB*	**Avg.** **Dahn [5]**	**Avg.** **Kambe [9]**	**Avg.** **Pande [13]**
stage 1	3.682	-	3.682/3.682	3.700	3.706	3.713
stage 2	3.652	3.416/3.387	3.535/3.518	3.520	3.530	3.546
stage 3	3.639	3.406/3.376	3.478/3.465	3.450	3.460	3.439
stage 4	3.625	3.403/3.373	3.457/3.440	-	-	3.406
stage 6	3.622	3.405/3.372	3.440/3.414	-	-	-
stage 9	3.622	3.403/3.372	3.427/3.407	-	-	-
graphite	-	3.402/3.373	3.402/3.373	3.355	3.355	3.35

3.2. Diffusion Barriers

Diffusion barriers for ion transport are among the most interesting properties of mixed ion-electron conductor (MIEC) materials such as Li-GICs. They are the crucial input parameter of any kinetic Monte Carlo simulation [48] that aims to predict large-scale phenomena such as phase transitions between stages or non-equilibrium configurations during fast charging. They are also quite difficult to reliably calculate, since they are closely linked to the interlayer distance, which, as previously pointed out, is still hard to predict, even with state-of-the-art DFT, especially for dilute, low SOC configurations.

In order to rigorously investigate the transport properties of Li-GICs, we constructed a variety of structures based on 2- and 3-layered supercells with 36 and 48 carbon atoms, respectively. This allows us to consider different staging and Li-stacking orders for equivalent stoichiometries. We fully relaxed all structures, extracted the interlayer distances, and calculated the energy barriers (Table 3) for exemplary bridge-path diffusion processes

(connecting the next-neighbor Li positions) using the NEB method (see Supplementary Information). for the exact initial and final states of the bridge path NEBs, as well as the predicted barrier diagrams.

Table 3. Interlayer distances and migration barriers (to the neighboring Li-position), calculated with GPrep-DFTB for a variety of differently stacked, staged, and filled Li-GICs. Regarding the stacking description, A refers to the carbon sheets, whereas α and β refer to the ordering of Li-ions.

	Stage	Stacking	In-Plane %	Avg LS [Å]	Filled/Empty [Å]	Barrier [eV]
LiC_{48}	III	$AAA\alpha$	1/3	3.446	3.525/3.406	0.493
Li_2C_{48}	III	$AAA\alpha$	2/3	3.478	3.616/3.409	0.441
Li_3C_{48}	III	$AAA\alpha$	3/3	3.478	3.631/3.402	0.424
LiC_{36}	II	$AA\alpha$	1/3	3.469	3.530/3.408	0.504
Li_2C_{36}	II	$AA\alpha$	2/3	3.512	3.614/3.410	0.451
Li_3C_{36}	II	$AA\alpha$	3/3	3.535	3.652/3.418	0.426
Li_2C_{36}	I	$A\alpha A\alpha$	1/3	3.539	3.539/ —	0.492
Li_4C_{36}	I	$A\alpha A\alpha$	2/3	3.625	3.625/ —	0.443
$Li_4C_{36}*$	I	$A\alpha A\beta$	2/3	3.658	3.658/ —	0.412
Li_6C_{36}	I	$A\alpha A\alpha$	3/3	3.682	3.682/ —	0.404
$Li_6C_{36}*$	I	$A\alpha A\beta$	3/3	3.758	3.758/ —	0.396

Analyzing the interlayer distances first, there are multiple trends to observe. First of all, structures with an $A\alpha A\alpha$ order (Greek letters indicating the Li layer order) consistently relax to a smaller interlayer distance than structures with an $A\alpha A\beta$ stacking, implying that the former may be more favorable. In terms of the total energy per unit of 6 carbon atoms, however, we see virtually no difference ($A\alpha A\beta$: -297.279 eV/6C, $A\alpha A\alpha$: -297.253 eV/6C) for both structures fully relaxed in terms of cell parameters and all atom positions. This deviation of $E(A\alpha A\alpha) - E(A\alpha A\beta) = 26$ meV/6C is on the order of $k_B T$ at room temperature, implying that at ambient conditions, no clear distinction between the Li orderings can be made and experiments would probably see a mixture of both. For reference, DFT (PBE + D3), which we consider trustworthy at least for high SOC compounds, predicts a deviation of $E(A\alpha A\alpha) - E(A\alpha A\beta) = -14$ meV/6C. It is necessary to recognize the difference in sign here, but since both values are within $k_B T$ at room temperature and at the limit of DFT errors, we do not believe that this constitutes a relevant difference.

Furthermore, for stoichiometries which can either be arranged as dilute stage 1 or dilute stage 2 (Li_2C_{36}) geometries, stage 2 has the lower interlayer distance and is therefore favored, which is in line with the agreed upon theory of staging and domain formation [47]. This is due to the fact that the z direction expansion of a gallery does not vary linearly with the filling factor. The total expansion from the 0% filling to 100% filling is 0.315 Å for $A\alpha A\alpha$-stacked stage 1 compounds. Filling empty layers by 33% (stage 1—Li_2C_{36}) already expands the interlayer distance by 0.165 Å, which is 52% of the total expansion. At 66% filling (stage 1—Li_4C_{36}), the interlayer distance is expanded by 0.252 Å, which is 80% of the total expansion.

In terms of the diffusion barriers, experimental sources vary quite a lot. This is due to the fact that the measuring technique, as well as additional factors such as temperature, play a role. Furthermore, if total diffusivities are measured, it is difficult to separate those into energetic and kinetic contributions. Langer et al. [21] measured a barrier of 0.55 eV (LiC_6) by means of Lithium nuclear magnetic resonance (Li-NMR), Freilander et al. [22] report 0.6 eV (LiC_6) and 1.0 eV (LiC_{12}) using beta-NMR and Magerl et al. [23] find 1.0 eV (LiC_6) by means of the quasielectric neutron scattering (QENS) at $T > 630$ K.

On the theoretical (DFT) side of things, the revPBE-D3-BJ approach by Thinius et al. [14] (which has proven very accurate for structural parameters and formation energies) predicts the barriers of 0.42 eV (LiC_6) and 0.47 eV (LiC_{12}). Toyoura et al. [24] reported 0.3 eV (LiC_6) and 0.49 eV (empty gallery) by means of DFT (LDA) and Persson et al. [25] predict 0.283 eV (LiC_6) and 0.297 eV (LiC_{12}), using DFT (GGA) with the interlayer distances fixed at experimental values. Even though there is some variation in the absolute numbers, both

theoretical and experimental studies are in general agreement on the ordering of the barrier heights: $LiC_6 < LiC_{12} <$ empty gallery. This corresponds to an inverse dependency on the interlayer distance of the respective gallery.

Using GPrep-DFTB, we predict barriers of 0.404 eV (LiC_6), 0.426 eV (LiC_{12}) and 0.504 eV (empty gallery). These results capture the same previously explained qualitative trend as the references. This also holds true for other configurations that had not been investigated before, such as $A\alpha A\beta$-stacked and stage 3 structures. Quantitatively, our results are in particularly good agreement with the revPBE-D3-BJ approach [14].

3.3. Formation Energetics

The intercalation energies of Li-ions entering the GIC at different states of charge are a crucial measure for predicting the most stable configurations throughout the charging process and the phase transitions between those. Therefore, as a third benchmark, we calculated the formation energies of LiC_6, LiC_{12} and LiC_{18}, and compared them with various experimental and theoretical studies (Table 4).

We calculate the intercalation energies per lithium atom (or, equivalently, per formula unit), as

$$\Delta E_{int}(LiC_{6n}) = E(LiC_{6n}) - nE(C_6) - E(Li) \tag{1}$$

where n is the stage number and $E(\cdot)$ is the DFTB total energy. These are directly comparable to the corresponding literature values obtained by DFT calculations. The latter thus do not include any finite temperature effects. On the other hand, experimental values are formation-free energies or enthalpies. Additionally, the calorimetric reference [20] is taken at elevated temperature (455 K) and with liquid lithium as precursor, rather than at room temperature with a solid lithium electrode. As a final note, the calculated values correspond to infinite phases of perfect stage n stoichiometry, whereas the true compounds at the corresponding stoichiometries are a mixture of domains of yet unknown structural details. Consequently, the values given within the scope of this parametrization study are not yet intended to be quantitatively comparable to the experiment, but one may still identify qualitative trends, just like with regular DFT. The DFTB model opens up the way to forthcoming more realistic, quantitative simulations.

Table 4. Formation energies in eV per formula unit, calculated with GPrep-DFTB and compared to an overview of the experimental and theoretical results from other studies. Both DFTB and DFT values are variations in the total energy ΔE_{int}, while experimental values are variations in enthalpy ΔH_{int} where available—otherwise they are variations in free energy ΔG_{int}).

	GPrep-DFTB	Experiment				DFT		
Ref:		*(a)*	*(b)*	*(c)*	*(d)*	*(e)*	*(f)*	*(g)*
LiC_6	−0.14	−0.156 *	−0.114	−0.144	−0.17	−0.22	−0.07	−0.23
LiC_{12}	−0.40	−0.228 *	−0.352	−0.257	−0.27	−0.28	−0.12	−0.33
LiC_{18}	−0.42	−0.273 *	−0.492	−	−	−	−	−0.29

Experimental references: *(a)*, [19] *(b)* [6] OCV, vs. solid Li; *(c)* calorimetry, vs. liquid Li [20]; DFT references: *(d)* revPBE-D3-BJ [14]; *(e)* optB88-vdW [12]; *(f)* revPBE-vdW [12]; *(g)* GGA-PP [11]; * These values are intercalation free energies ΔG_{int}. The value for LiC_{18} is not directly given in the paper but can be consistently extracted using the same formula the authors used for LiC_{12}.

For the formation energies, the experimental studies [6,19,20] do not agree as closely, as for the structural parameters, but they do at least provide the same ordering for LiC_6 and LiC_{12} and LiC_{18}. Interestingly, the values extracted from open circuit voltage (OCV) measurements only agree in the ordering if the energies are taken per formula unit. Normalizing the energies per graphite unit, LiC_{12} would have a less negative formation energy than LiC_6. As the OCV curves in [6,19] agree with each other, we attribute the mismatch to different methods for extracting the formation energies from the OCV curve. We also note here that our structural models closely correspond to highly oriented pyrolytic graphite

(HOPG), while all the referenced OCV curves were taken with different forms of graphitic carbon. In order to make sure that the deviation was negligible, we measured the OCV curve for HOPG. Due to the small insertion surface for Li-ions, the characteristic voltage plateaus are not as visible. However, in the regions corresponding to the phase transitions between LiC_{18} to LiC_{12} and LiC_{12} to LiC_6, the measured HOPG curve matches within 0.01 V with the references. Our measured OCV curve is shown in the Supplementary Information for both HOPG and the coin cell.

Similarly, as for the C–C interlayer distance, the different DFT functionals vary significantly in their performance predicting the formation energetics of Lithium-GICs. Compared with the experimental studies, revPBE-D3-BJ [14] proves to be best, just as it did previously for the C–C interlayer distance. According to [12], revPBE-vdW correctly predicts the phase transitions between stage 1 and stage 2 qualitatively (even though it strongly underestimates the formation energies), whereas optB88-vdW does not. For revPBE-D3-BJ, we do not have this information.

Overall, the formation energy for LiC_6 tends to be consistent across experimental measurements and most computed references. Our results with GPrep-DFTB are equally accurate for LiC_6, while for both LiC_{12} and LiC_{18}, we obtain more negative formation energies than the majority of references (with the exclusion of [6]). However, this is not necessarily a pitfall, considering that the finite temperature contributions are not included. The effect of the latter is generally nontrivial; in particular, the entropy variation in Li-GICs is *negative* for the largest part of the state of charge range. Given the overall uncertainty in both experimental and computed references, we leave this question open for further investigation and adjustments to the parametrization, if needed. We note in passing that potential refinements to the GPrep-DFTB parametrization are possible with little effort, by simply retraining the repulsion potential with additional training data and/or finely tuned hyperparameters. As a perspective, we intend to use this parametrization to train a cluster expansion similarly to [10,49], in order to perform free energy sampling and calculate the OCV curve. If that agrees with the measurements, then the non-perfect energetics of single ideal geometries is only a minor setback.

3.4. Long-Range Interactions

Having successfully benchmarked our GPrep-DFTB approach against a variety of comparatively small-scale properties, we proceeded towards calculating some larger-scale properties which are out of reach of DFT (at least at a reasonable computational cost). First, we want to investigate the long-range in-plane interaction between two Li-ions within Li-GIC. In order to do that, we constructed a supercell with 218 carbon atoms and two layers to eliminate any periodic next-layer interactions and allow for the bulging of the graphene sheets. We then exhaustively performed 47 full structure relaxations of all symmetry-inequivalent local minima and maxima for two Li atoms within a single layer in that supercell, as well as 41 five-image NEBs for the diffusion processes between each adjacent pair of local minima. With our method, all of this is possible within days and on a regular workstation. This leaves us with 170 data-points, which we use to fit a 2D potential energy landscape for the whole supercell (Figure 3a) and also to plot the Li–Li interactions as a function of the Li–Li distances (Figure 3b,c).

As our results clearly show, the in-plane Li–Li interactions are governed by Coulombic repulsion. Even quantitatively, our predictions agree very well with the approach of Pande et al. [13] (BEEF-vdW-DFT + Ising model). However, they were only able to provide four data points which are local minima and therefore quite cheap to calculate, whereas we can also predict transition states (which require NEB calculations and are much more computationally expensive because of that). This proves that GPrep-DFTB is capable of very accurately capturing the Li-GIC system's electrostatic properties, and of doing so for vastly more and larger supercells than DFT.
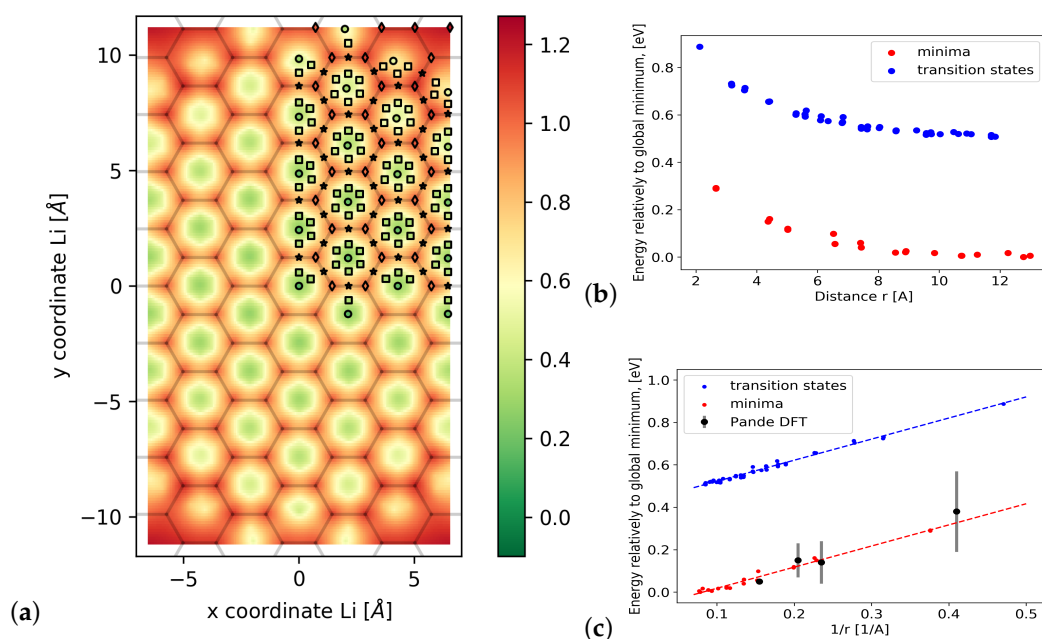
Figure 3. (**a**) Calculated potential energy surface for a freely moving Li-ion with respect to a second fixed ion in the corner of the unit cell (see main text for details of the structural model). Color gradient in eV relative to the global minimum at (0/0). Circles are local minima, diamonds are local maxima, stars are transition states (calculated with the cNEB method), and squares are additional images from the NEBs—all of which have been used for the 2D fit; (**b**) Potential energy depending on the distance between the two Li-ions (blue dots are the transition positions, red dots are the ground states); (**c**) Potential energy depending on the reciprocal distance—clearly showing the Coulombic nature of the interaction, which agrees with [13].

Based on this, it is then possible to extract the slope from Figure 3c, which, via the relation:

$$E = \frac{e^2 Z^2}{4\pi\varepsilon_r} \frac{1}{R} \tag{2}$$

gives us access to the relative dielectric constant ε_r of the system. We note, however, that this is the effective dielectric response experienced by Li-ions within the Li-GIC and not the macroscopic dielectric constant of the GIC *including* the contribution due to the Li ion motion. By means of linear regression, we obtain a slope of 0.996 ± 0.015 eVÅ. This leads to ε_r / Z^2 = 14.46 ± 0.22. For an assumed partial charge Z of 0.8 to 0.9 for the Li-ions, which is in line with the charge analysis performed by Rana et al. [50], we then predict a relative dielectric constant of 9.1–11.9. Expanding on this in future work, we will be able to, for the first time, determine the dielectric constant of Li-GIC as a function of the state of charge, which is an important input parameter for kinetic Monte Carlo simulations of charge carriers.

3.5. Domains vs. Dilute

While the general truth of the Daumas–Heróld domain model [7] has been widely accepted and supported by both theoretical [51,52] and experimental [53,54] studies, qualitative details such as domain sizes and shapes, dependencies on the charging speed and other dynamic factors have not been understood to a sufficient degree. As pointed out in [55], the formation of domains is at least partially responsible for the wide range of Li-ion diffusivities reported from the experiment ($10^{-6} - 10^{-14} \frac{cm^2}{s}$ [25]), and therefore of crucial importance for understanding the overall behavior of Li-GICs, especially when exposed to the rapidly growing charging speeds that are necessary today.

In order to provide a further demonstration of our method's potential to bring forward a new understanding of these phenomena in the future, we constructed four supercells with

roughly 600 atoms each—two of them in a dilutely spaced configuration (with the Li-ions spread evenly across the filled layers, right column in Figure 4) and two of them with a configuration according to the Daumas–Heróld domain model (Figure 4, left column)—and performed full structure relaxations on each of them. Note that what we show here is *one* possible realization of the dilute LiC_{12} and LiC_{24}, but there are necessarily many other disordered realizations with very similar total energies and any experiment would likely see a mix of these.
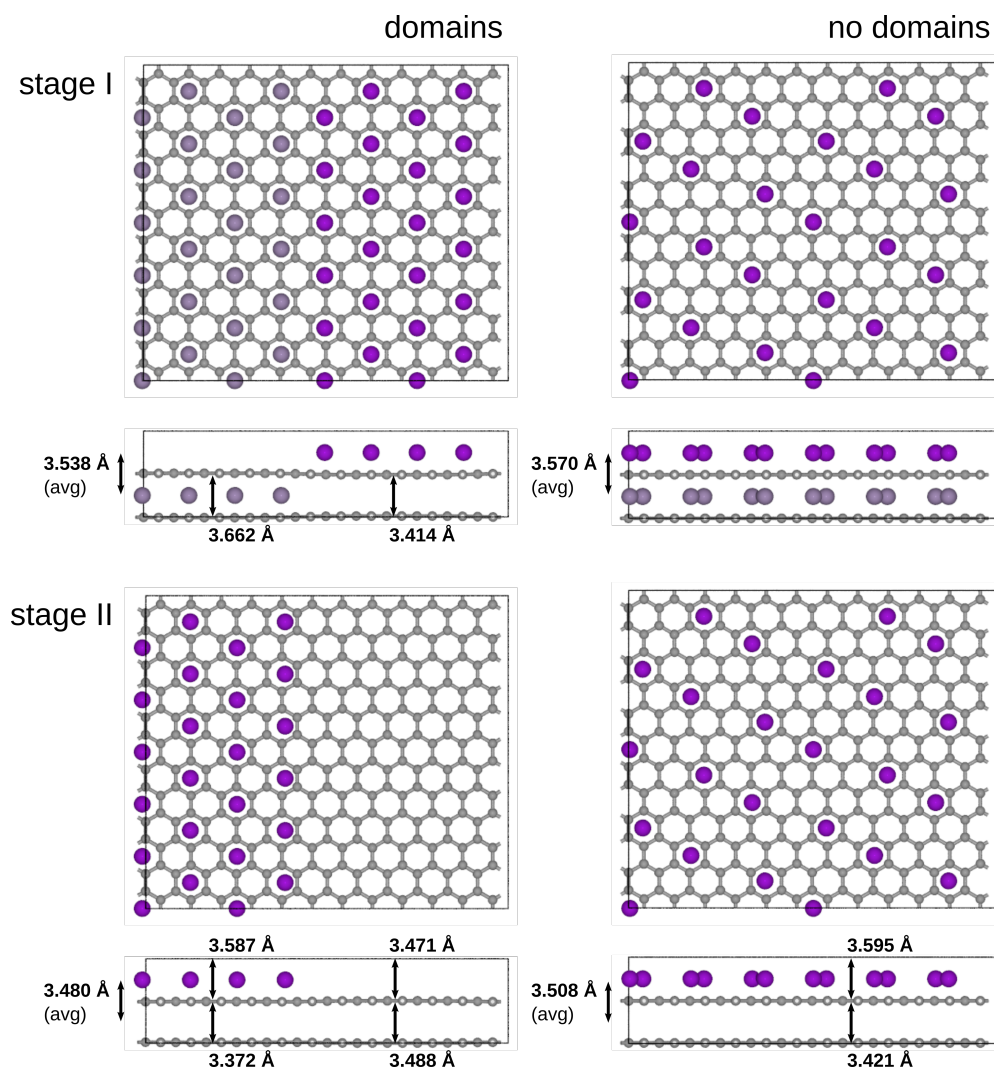
Figure 4. Top- and sideview of stage 1 and stage 2 domain-like and dilute Li-GIC configurations. Structures are fully relaxed, providing both overall average interlayer distances and local interlayer distances for filled and empty areas. For both stages, the domain-like structure has a smaller overall interlayer distance.

Our results show that both in the stage 1 (upper row) and the stage 2 (bottom row) compound, the domain–structure expanded to a significantly smaller overall interlayer distance, meaning it is favored compared to the evenly spaced one. This agrees with the Daumas–Heróld domain model [7]. Furthermore, we were also capable of extracting *local* interlayer distances for different areas of the structure. As shown in Figure 4, the difference in interlayer distance between the empty and filled domains is larger than 0.2 Å, which is much larger than any residual differences in the computed values above. According to both DFT [56] and our own results (Table 3), this difference corresponds to a difference in diffusion barriers of approximately 0.1 eV or 25%. Given this direct dependency, GPrep-DFTB could, for example, be used to reliably predict local diffusivities in large structures

without the need to perform costly NEB calculations. Additionally, we believe that the capacity of GPrep-DFTB for fully relaxing large unit-cells with a multitude of Li-ion distributions has great potential for building more diverse and well-rounded training-sets for, e.g., lattice gas expansions or machine-learning models, than DFT could, also including the 'empty' or 'almost empty' regions of the Daumas–Heród domain model, for which we provided an extensive model in Figure 3. This makes GPrep-DFTB a crucial new bridge between the atomistic scale and the macroscopic scale of Li-GIC modeling.

4. Conclusions

The structural, energetic and electronic properties of Li-GICs were theoretically investigated with our DFTB parametrization (based on GPR repulsion fitting) and benchmarked against dispersion-corrected DFT calculations and experiments. The calculated lattice parameters of graphite ($a = 2.476$ Å, $c = 6.746$ Å) agree better with experiments than most DFT approaches. For stages 1 through 4, our method correctly predicts the non-linear nature of the increase in the interlayer distance in LiC_x upon intercalation, not only qualitatively but quantitively as well. LiC_6 relaxes to an interlayer distance of 3.682 Å. The calculated formation energies of -0.14 eV (LiC_6), -0.40 eV (LiC_{12}) and -0.42 eV (LiC_{18}) per formula unit slightly overestimate the experimental results, but are within the range of DFT predictions. We expect future calculations which include entropy effects to be even more accurate. The calculated diffusion barriers (0.396 eV–0.504 eV, depending on the configuration) show trends supported by accepted theory, such as the Daumas–Heród domain model, and agree with state-of-the-art DFT studies and experiments. In terms of long-range Li–Li interactions, our model captures the Coulombic nature also discovered by DFT, but is at the same time capable of accessing much larger supercells. Based on these calculations, we predict a dielectric constant for LiC_{108} in the range of 9.1–11.9 and recognize the potential of GPrep-DFTB to, for the first time, calculate the dielectric constant of the Li-GIC as a function of the SOC in the near future. Finally, the GPrep-DFTB relaxation of large structures in both dilute and domain-like configurations predicts less expansion of the interlayer distance for the domain structure—again agreeing with previous studies and illustrating the potential of our method for further investigation into the complex and large-scale physics taking place in Li-GICs and for being a new kind of bridge between the atomistic scale and the macroscopic scale of future battery materials.

Conflicts of Interest: The authors declare no conflict of interest.

References

1. Zhang, H.; Yang, Y.; Ren, D.; Wang, L.; He, X. Graphite as anode materials: Fundamental mechanism, recent progress and advances. *Energy Storage Mater.* **2020**, *36*, 147–170. [CrossRef]
2. Asenbauer, J.; Eisenmann, T.; Kuenzel, M.; Kazzazi, A.; Chen, Z.; Bresser, D. The success story of graphite as a lithium-ion anode material–fundamentals, remaining challenges, and recent developments including silicon (oxide) composites. *Sustain. Energy Fuels* **2020**, *4*, 5387. [CrossRef]
3. Grosu, C.; Panosetti, C.; Merz, S.; Jakes, P.; Matera, S.; Eichel, R.A.; Granwehr, J.; Scheurer, C. Lithium intercalation into graphite beyond LiC_6 at ambient pressure. *arXiv* **2021**, arXiv:2107.11137.
4. Zhang, C.; Ma, J.; Han, F.; Liu, H.; Zhang, F.; Fan, C.; Liu, J.; Li, X. Strong anchoring effect of ferric chloride-graphite intercalation compounds (FeCl 3-GICs) with tailored epoxy groups for high-capacity and stable lithium storage. *J. Mater. Chem. A* **2018**, *6*, 17982. [CrossRef]
5. Dahn, J.; Fong, R.; Spoon, M. Suppression of staging in lithium-intercalated carbon by disorder in the host. *Phys. Rev. B* **1990**, *42*, 6424. [CrossRef]
6. Reynier, Y.; Yazami, R.; Fultz, B. The entropy and enthalpy of lithium intercalation into graphite. *J. Power Sources* **2003**, *119*, 850. [CrossRef]
7. Daumas, N.; Heróld, A. Relations between phase concept and reaction mechanics in graphite insertion compounds. *C. R. Acad. Sci. C* **1969**, *268*, 373.
8. Vadlamani, B.; An, K.; Jagannathan, M.; Chandran, K.R. An in situ electrochemical cell for neutron diffraction studies of phase transitions in small volume electrodes of Li-ion batteries. *J. Electrochem. Soc.* **2014**, *161*, A1731. [CrossRef]
9. Kambe, N.; Dresselhaus, M.; Dresselhaus, G.; Basu, S.; McGhie, A.; Fischer, J. Intercalate ordering in first stage graphite-lithium. *Mater. Sci. Eng.* **1979**, *40*, 1. [CrossRef]
10. Babar, M.; Parks, H.L.; Houchins, G.; Viswanathan, V. An accurate machine learning calculator for the lithium-graphite system. *J. Phys. Energy* **2020**, *3*, 014005. [CrossRef]
11. Imai, Y.; Watanabe, A. Energetic evaluation of possible stacking structures of Li-intercalation in graphite using a first-principle pseudopotential calculation. *J. Alloy. Compd.* **2007**, *439*, 258. [CrossRef]
12. Lenchuk, O.; Adelhelm, P.; Mollenhauer, D. Comparative study of density functionals for the description of lithium-graphite intercalation compounds. *J. Comput. Chem.* **2019**, *40*, 2400. [CrossRef]
13. Pande, V.; Viswanathan, V. Robust high-fidelity DFT study of the lithium-graphite phase diagram. *Phys. Rev. Mater.* **2018**, *2*, 125401. [CrossRef]
14. Thinius, S.; Islam, M.M.; Heitjans, P.; Bredow, T. Theoretical study of Li migration in lithium–graphite intercalation compounds with dispersion-corrected DFT methods. *J. Phys. Chem. C* **2014**, *118*, 2273. [CrossRef]
15. Fujikake, S.; Deringer, V.L.; Lee, T.H.; Krynski, M.; Elliott, S.R.; Csányi, G. Gaussian approximation potential modeling of lithium intercalation in carbon nanostructures. *J. Chem. Phys.* **2018**, *148*, 241714. [CrossRef] [PubMed]
16. Hourahine, B.; Aradi, B.; Blum, V.; Bonafé, F.; Buccheri, A.; Camacho, C.; Cevallos, C.; Deshaye, M.Y.; Dumitrică, T.; Dominguez, A.; et al. DFTB+, a software package for efficient approximate density functional theory based atomistic simulations. *J. Chem. Phys.* **2020**, *152*, 124101. [CrossRef]
17. Trucano, P.; Chen, R. Structure of graphite by neutron diffraction. *Nature* **1975**, *258*, 136. [CrossRef]
18. Yin, M.; Cohen, M.L. Structural theory of graphite and graphitic silicon. *Phys. Rev. B* **1984**, *29*, 6996. [CrossRef]
19. Ohzuku, T.; Iwakoshi, Y.; Sawai, K. Formation of lithium-graphite intercalation compounds in nonaqueous electrolytes and their application as a negative electrode for a lithium ion (shuttlecock) cell. *J. Electrochem. Soc.* **1993**, *140*, 2490. [CrossRef]
20. Avdeev, V.V.; Savchenkova, A.P.; Monyakina, L.A.; Nikol'skaya, I.V.; Khvostov, A.V. Intercalation reactions and carbide formation in graphite-lithium system. *J. Phys. Chem. Solids* **1996**, *57*, 947. [CrossRef]
21. Langer, J.; Epp, V.; Heitjans, P.; Mautner, F.A.; Wilkening, M. Lithium motion in the anode material LiC_6 as seen via time-domain ^{7}Li NMR. *Phys. Rev. B* **2013**, *88*, 094304. [CrossRef]
22. Freiländer, P.; Heitjans, P.; Ackermann, H.; Bader, B.; Kiese, G.; Schirmer, A.; Stöckmann, H.J.; Van der Marel, C.; Magerl, A.; Zabel, H. Diffusion Processes in LiC_6 Studied by β-NMR. *Z. Phys. Chem.* **1987**, *151*, 93. [CrossRef]
23. Magerl, A.; Zabel, H.; Anderson, I. In-plane jump diffusion of Li in LiC_6. *Phys. Rev. Lett.* **1985**, *55*, 222. [CrossRef] [PubMed]
24. Toyoura, K.; Koyama, Y.; Kuwabara, A.; Tanaka, I. Effects of off-stoichiometry of LiC_6 on the lithium diffusion mechanism and diffusivity by first principles calculations. *J. Phys. Chem. C* **2010**, *114*, 2375. [CrossRef]
25. Persson, K.; Hinuma, Y.; Meng, Y.S.; Van der Ven, A.; Ceder, G. Thermodynamic and kinetic properties of the Li-graphite system from first-principles calculations. *Phys. Rev. B* **2010**, *82*, 125416. [CrossRef]
26. Panosetti, C.; Anniés, S.B.; Grosu, C.; Seidlmayer, S.; Scheurer, C. DFTB Modeling of Lithium-Intercalated Graphite with Machine-Learned Repulsive Potential. *J. Phys. Chem. C* **2021**, *125*, 691. [CrossRef]
27. Chou, C.P.; Nishimura, Y.; Fan, C.C.; Mazur, G.; Irle, S.; Witek, H.A. Automatized Parameterization of DFTB Using Particle Swarm Optimization. *J. Chem. Theory Comput.* **2016**, *12*, 53. [CrossRef]
28. Panosetti, C.; Engelmann, A.; Nemec, L.; Reuter, K.; Margraf, J.T. Learning to Use the Force: Fitting Repulsive Potentials in Density-Functional Tight-Binding with Gaussian Process Regression. *J. Chem. Theory Comput.* **2020**, *16*, 2181. [CrossRef] [PubMed]

29. Blum, V.; Gehrke, R.; Hanke, F.; Havu, P.; Havu, V.; Ren, X.; Reuter, K.; Scheffler, M. Ab initio molecular simulations with numeric atom-centered orbitals. *Comput. Phys. Commun.* **2009**, *180*, 2175. [CrossRef]

30. Perdew, J.P.; Burke, K.; Ernzerhof, M. Generalized Gradient Approximation Made Simple. *Phys. Rev. Lett.* **1996**, *77*, 3865. [CrossRef]

31. Tkatchenko, A.; Scheffler, M. Accurate Molecular Van Der Waals Interactions from Ground-State Electron Density and Free-Atom Reference Data. *Phys. Rev. Lett.* **2009**, *102*, 073005. [CrossRef] [PubMed]

32. DiStasio, R.A.; Gobre, V.V.; Tkatchenko, A. Many-body van der Waals interactions in molecules and condensed matter. *J. Condens. Matter Phys.* **2014**, *26*, 213202. [CrossRef] [PubMed]

33. Plimpton, S. Fast Parallel Algorithms for Short-Range Molecular Dynamics. *J. Comput. Phys.* **1995**, *117*, 1. [CrossRef]

34. Nichol, A.; Ackland, G.J. Property trends in simple metals: An empirical potential approach. *Phys. Rev. B* **2016**, *93*, 184101. [CrossRef]

35. Bahn, S.R.; Jacobsen, K.W. An object-oriented scripting interface to a legacy electronic structure code. *Comput. Sci. Eng.* **2002**, *4*, 56. [CrossRef]

36. Shanno, D.F. An example of numerical nonconvergence of a variable-metric method. *J. Optim. Theory Appl.* **1985**, *46*, 87. [CrossRef]

37. Henkelman, G.; Jónsson, H. Improved tangent estimate in the nudged elastic band method for finding minimum energy paths and saddle points. *J. Chem. Phys.* **2000**, *113*, 9978. [CrossRef]

38. Henkelman, G.; Uberuaga, B.P.; Jónsson, H. A climbing image nudged elastic band method for finding saddle points and minimum energy paths. *J. Chem. Phys.* **2000**, *113*, 9901. [CrossRef]

39. Bitzek, E.; Koskinen, P.; Gähler, F.; Moseler, M.; Gumbsch, P. Structural relaxation made simple. *Phys. Rev. Lett.* **2006**, *97*, 170201. [CrossRef] [PubMed]

40. Johnson, D.D. Modified Broyden's method for accelerating convergence in self-consistent calculations. *Phys. Rev. B* **1988**, *38*, 12807. [CrossRef] [PubMed]

41. Zhechkov, L.; Heine, T.; Patchkovskii, S.; Seifert, G.; Duarte, H.A. An efficient a posteriori treatment for dispersion interaction in density-functional-based tight binding. *J. Chem. Theory Comput.* **2005**, *1*, 841. [CrossRef] [PubMed]

42. Chung, D. Review graphite. *J. Mater. Sci.* **2002**, *37*, 1475. [CrossRef]

43. Wang, Z.; Selbach, S.M.; Grande, T. Van der Waals density functional study of the energetics of alkali metal intercalation in graphite. *RSC Adv.* **2014**, *4*, 4069. [CrossRef]

44. Grimme, S.; Antony, J.; Ehrlich, S.; Krieg, H. A consistent and accurate ab initio parametrization of density functional dispersion correction (DFT-D) for the 94 elements H-Pu. *J. Chem. Phys.* **2010**, *132*, 154104. [CrossRef]

45. Tkatchenko, A.; DiStasio Jr, R.A.; Car, R.; Scheffler, M. Accurate and efficient method for many-body van der Waals interactions. *Phys. Rev. Lett.* **2012**, *108*, 236402. [CrossRef]

46. Gould, T.; Lebègue, S.; Ángyán, J.G.; Bučko, T. A Fractionally Ionic Approach to Polarizability and van der Waals Many-Body Dispersion Calculations. *J. Chem. Theory Comput.* **2016**, *12*, 5920. [CrossRef]

47. Dresselhaus, M.S.; Dresselhaus, G. Intercalation compounds of graphite. *Adv. Phys.* **2002**, *51*, 1. [CrossRef]

48. Andersen, M.; Panosetti, C.; Reuter, K. A Practical Guide to Surface Kinetic Monte Carlo Simulations. *Front. Chem.* **2019**, *7*, 202. [CrossRef]

49. Mercer, M.P.; Peng, C.; Soares, C.; Hoster, H.E.; Kramer, D. Voltage hysteresis during lithiation/delithiation of graphite associated with meta-stable carbon stackings. *J. Mater. Chem. A* **2021**, *9*, 492. [CrossRef]

50. Rana, K.; Kucukayan-Dogu, G.; Sen, H.S.; Boothroyd, C.; Gulseren, O.; Bengu, E. Analysis of charge transfer for in situ Li intercalated carbon nanotubes. *J. Phys. Chem. C* **2012**, *116*, 11364. [CrossRef]

51. Axdal, S.A.; Chung, D. A theory for the kinetics of intercalation of graphite. *Carbon* **1987**, *25*, 377. [CrossRef]

52. Kirczenow, G. Kinetics of stage ordering and stage transitions. *Phys. Rev. Lett.* **1985**, *55*, 2810. [CrossRef]

53. Dimiev, A.M.; Ceriotti, G.; Behabtu, N.; Zakhidov, D.; Pasquali, M.; Saito, R.; Tour, J.M. Direct real-time monitoring of stage transitions in graphite intercalation compounds. *ACS Nano* **2013**, *7*, 2773. [CrossRef] [PubMed]

54. Wang, F.; Graetz, J.; Moreno, M.S.; Ma, C.; Wu, L.; Volkov, V.; Zhu, Y. Chemical distribution and bonding of lithium in intercalated graphite: Identification with optimized electron energy loss spectroscopy. *ACS Nano* **2011**, *5*, 1190. [CrossRef]

55. Krishnan, S.; Brenet, G.; Machado-Charry, E.; Caliste, D.; Genovese, L.; Deutsch, T.; Pochet, P. Revisiting the domain model for lithium intercalated graphite. *Appl. Phys. Lett.* **2013**, *103*, 251904. [CrossRef]

56. Xu, B.; Wu, M.; Liu, G.; Ouyang, C. Understanding the effect of the layer-to-layer distance on Li-intercalated graphite. *J. Appl. Phys.* **2012**, *111*, 124325. [CrossRef]

C   Paper 3

The intrinsic electrostatic dielectric behaviour of graphite anodes in Li-ion batteries – across the entire functional range of charge

Simon Anniés, Christoph Scheurer, Chiara Panosetti
Electrochimica Acta, 2023

The intrinsic electrostatic dielectric behaviour of graphite anodes in Li-ion batteries—Across the entire functional range of charge

Simon Anniés [a,b,*], Christoph Scheurer [a], Chiara Panosetti [a]

[a] *Fritz-Haber-Institute of the Max–Planck-Society, Faradayweg 4-6, 14195, Berlin, Germany*
[b] *Chair for Theoretical Chemistry, TU Munich, Lichtenbergstr. 4, 85747, Garching b. München, Germany*

ARTICLE INFO

ABSTRACT

Lithium–graphite intercalation compounds (Li-GICs) are by far the most common anode material for modern Li-ion batteries. However, the dielectric response of this material in the electrostatic limit and its variation depending on the state of charge (SOC) has not been investigated to a satisfactory degree – neither by means of theory nor by experiment – and especially not for the higher range of SOC. In this work, we – for the first time – predict a mostly linear dependency of the relative permittivity ϵ_r on the SOC, from ≈ 7 at SOC 0% to ≈ 25 at SOC 100%. This is achieved by making use of our recently published DFTB parametrization for Li-GICs based on a machine-learned repulsive potential in order to overcome the computational hurdles of sampling the long-ranged Coulomb interactions within this material. In doing so, we provide novel insight into a property which is highly desired, particularly as an input parameter for charged kinetic Monte Carlo simulations.

1. Introduction

The relative permittivity (RP) is one of the defining properties of many materials, as it describes the degree to which the Coulomb interactions between charge carriers are screened within the material compared to vacuum. Especially in older literature, this property is also known as "dielectric constant", even though it is far from being constant, but dependent on temperature, the frequency of probing electric fields and even the underlying mechanisms in terms of polarizability, conductivity and others.

Traditionally, the RP has primarily been of interest for insulators, but in recent times it has also been increasingly investigated for conducting materials [1], where it stems from the interaction between a small fraction of the charge carriers and the atoms. The fact that these charge carriers are mobile in conducting materials fundamentally changes the way the property and its dependencies need to be understood within these materials, compared with insulators.

One group of materials of great interest are lithium–graphite intercalation compounds (Li-GICs), which constitute by far the most common anode material in modern lithium ion batteries. During the charging and discharging cycles of the battery, Li-ions are stored between the layers of the graphite host structures, up to a stoichiometry of LiC_6, which traditionally translates to a state of charge (SOC) of 100% and corresponds to one Li-ion above every third C_6 ring of the hexagonal base lattice—even though recent studies have shown that

overlithiation beyond that point is possible at ambient conditions [2]. The distribution of the Li-ions for intermediate SOCs is not uniform, but ordered as shown in Fig. 1, as first explained in [3].

Within the scope of this specific material, we define the RP we are investigating as "the damping of the electrostatic interaction between two Li-ions or Li-ion vacancies embedded in the material caused by the surrounding charge-carrier density". As of note, this is the *electrostatic*, low-frequency RP, as opposed to what is measured in many experiments, which make use of alternating AC-fields at a vast variety of frequencies [1,4]. Furthermore, we point out that this specific property is directionally separated—its contribution in the *xy*-plane (in this work defined as parallel to the graphene sheets, i.e., the *ab*-plane in crystallographic notation) is expected to be different from the contribution in *z*-direction (orthogonal to the graphene sheets). This makes direct comparison with experiments performed on graphite powder as opposed to a "perfect" crystal non-trivial—a problem we address in Section 3.4.

One of the primary motivations for investigating the RP of Li-GICs is the fact that it is a required input parameter for including charge in kinetic Monte Carlo simulations (kMCs), which in turn are a crucial method for studying charge carrier dynamics in functional energy materials [5–8]. Long-ranged Coulomb interactions are a necessity when performing kMC on systems, which include charged or partially charged particles. For example, Casalegno et al. [9] have shown that
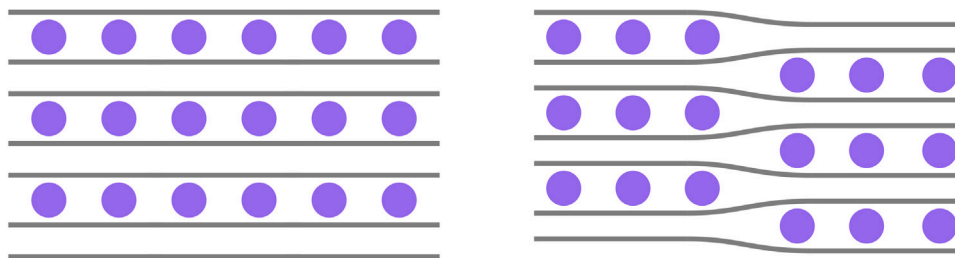

Fig. 1. Illustration of lithium-ions (purple spheres) intercalated into a graphite host structure (grey lines) at 50% state of charge, based on the Daumas–Herold domain model [3]. Li-ions tend to fill up every second layer completely (staging, left), before starting to intercalate into the other half of the layers. However, this behaviour is not global, but occurs in finite-sized domains (right) and is not expected to be perfect in real systems. During the intercalation process, the distance between the graphene sheets (interlayer distance) is increased by around 10%.

not including such interactions, as it would be the case when using e.g. force field approaches with finite-size descriptors, causes an error of 14% in the protonic diffusion coefficients in doped perovskites. The situation becomes especially complicated when looking at materials, which involve changes in the density and/or local ordering of charge carriers as part of their intended function. Examples are anodes, cathodes and electrolytes. but also e.g. perovskites in solar cells. This is due to the fact that the local relative permittivity then is not only influenced by the "host" material, but also by the charge carriers close by. Therefore, the RP of Li-GICs changes significantly depending on the SOC (*vide infra*).

Beyond the previously outlined interest for charge-kMC, we believe there to be many more valuable applications for the relative permittivity of Li-GICs also at higher levels of the multiscale simulation hierarchy: one such motivation is understanding charge gradients, as they occur during the fast charging of modern batteries in electric vehicles, and the chemical pressure which leads to plating and dendrite formation inside the batteries under certain operational conditions. The latter phenomenon is typically investigated by means of continuum simulations like e.g. by Hein et al. [10], which also rely at least implicitly on knowledge of the dielectric response. Furthermore, a simple model of the charge carrier electrostatics could be used as a physical baseline for otherwise short-ranged machine learning models or cluster expansions. Another related field is the development of functional materials based on doped graphite [11].

In order to bring forward new insight into the dielectric behaviour of LI-GICs, we put forward a systematic approach – based on our DFTB parametrization – to investigating this crucial property. The root principle is based upon considering the dielectric response "as felt by the charge-carriers". This translates to sampling the Coulomb-interactions between pairs of charge carriers inside the system, while varying the surrounding charge-carrier density in order to access different states of charge. In doing so, we are able to determine the relative permittivity of Li-GICs, as a function of the SOC, for the entire functional range of the material.

2. Methodology

2.1. Derivation of the relative permittivity ϵ_r from the Coulomb law and discussion of the partial charge transfer

In order to determine the relative permittivity within the system, our approach is to sample the electrostatic interactions between two charge carriers inside the system, placed at varying distances from each other. We begin our considerations with the electrostatic energy E_{Coul} of two charge densities ρ_1 and ρ_2, governed by the Coulomb law

$$E_{Coul} = \frac{1}{4\pi\epsilon_0\epsilon_r} \cdot \iint \frac{\rho_1 \cdot \rho_2}{|\vec{r}_1 - \vec{r}_2|} dr_1 dr_2 \tag{1}$$

where ϵ_0 is the vacuum permittivity. In this work, we chose to approximate the sampled charge carriers as point charges, an approximation

that is unproblematic for Li-ions, but requires a bit more consideration for Li-ion vacancies, which may be more diffuse in shape. In this approximation, the expression becomes

$$E_{Coul} = \frac{1}{4\pi\epsilon_0} \cdot \frac{Q_1 \cdot Q_2}{\epsilon_r} \cdot \frac{1}{|\vec{r}_1 - \vec{r}_2|} \tag{2}$$

which has been rearranged to clearly separate the continuum electrostatic from the geometric quantities. With the two point charges being Li-ions or Li-ion vacancies intercalated into the graphite host structure, we get

$$E_{Coul} = \frac{e^2}{4\pi\epsilon_0} \cdot \frac{Z_{Li}^2}{\epsilon_r} \cdot \frac{1}{R} \tag{3}$$

where e is the electron charge, Z_{Li} the partial charge on the Li-ion and R the distance between the two charge carriers. In order to link this Coulomb energy to the potential energy E_{pot} of an entire supercell, as we obtain from our DFTB calculations, an appropriate reference energy E_0 needs to be introduced, which is the host structure energy in the limit of $R \to \infty$ at that specific stoichiometry. With this we finally get:

$$E_{pot} = \frac{e^2}{4\pi\epsilon_0} \cdot \frac{Z_{Li}^2}{\epsilon_r} \cdot \frac{1}{R} + E_0 \tag{4}$$

The first two terms of this expression can be accessed as the slope of a linear regression, when plotting E_{pot} over $1/R$. In order to relate said slope to ϵ_r, we approximate $E_{Coul} \approx E_{pot} - E_0$. While this obviously holds in the macroscopic limit for a homogeneous medium, here we are attempting to measure the Coulombic repulsion felt by two particles on a potential energy surface (PES) resolved at the atomistic level. The latter is not infinitely smooth, but presents minima, maxima and saddle points due to the carbon host structure. It however shows a sufficiently regular pattern (as shown in [12]) to assume that analogous points (i.e., comparing minima with minima etc.) exhibit analogous local shape. Consistently, the DFTB total energy is indeed expressed, within the formalism of the method [13], as a sum of three contributions: the so-called band structure energy, the Coulomb energy (the expression of which depends explicitly on the partial charges on the individual atoms, *vide infra*), and the repulsive energy. Ideally, we can isolate the Coulomb energy between two particles in the system by considering "the rest of the DFTB total energy" as a background to subtract pointwise, assuming that it will be similar enough in similar local environments. Ideally, this would correspond to the limit for infinitely dilute, unperturbed PES, where the Coulombic interaction between charge carriers vanishes. In this light, for each sampled point we may identify a suitable pointwise reference E_0 as the corresponding point on such unperturbed PES, e.g., in the case of minima, the total energy of a minimum at the centre of any C_6 ring of the graphitic host sufficiently far away from the other charge carrier.

We point out that this approximation neglects distortions of the local structure and electron density that may be caused by two charge carriers being close together—an approximation that holds well for the low SOC regime, but not quite as well for the high SOC regime, as
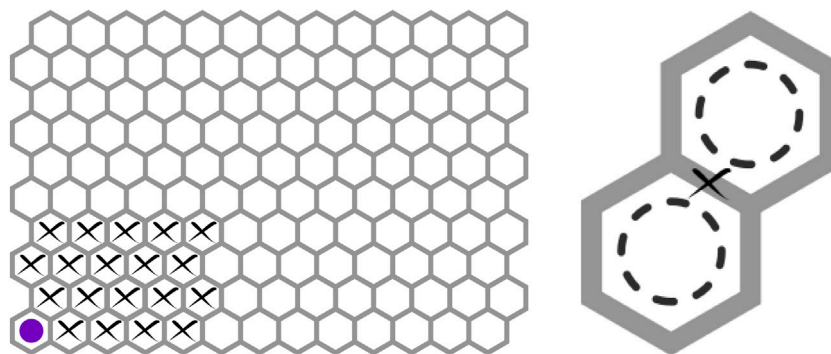
Fig. 2. *Left*: Illustration of the investigated layer for pairwise Coulombic Li-ion-interactions with one fixed Li-ion (*purple*). Of the local minimum locations marked with an "X", a maximum of one is occupied by the other Li-ion, while all others are empty. This layer will be referred to as *inv(Li)* throughout this work. *Right*: Illustration of a "transition state" between two local minima.

will be shown. The reference energy E_0 does not impact the relative energetics, but only causes an up or down shift along the y-axis. Therefore, it is not immediately relevant for the extraction of the ϵ_r, but it is needed for consistent plotting of the Coulomb energy. For this reason, we estimate E_0 by interpolating the slope to the $1/R \to 0$ limit (see the following chapters for more details).

The only other variable that is left, then, is the partial charge of the intercalated lithium Z_{Li}. It is known that, upon intercalation, the electron density of the Li-atom is partially transferred to the carbon host structure, leaving the intercalant as something usually denominated as Li$^+$, but the exact magnitude of said charge transfer is hard to pinpoint—and not an observable. The self-consistent-charge cycles of our DFTB+ calculations output a local electron population of around 0.21 to 0.26 for the Li-intercalants depending on the local environment of the respective Li-ion, which corresponds to a partial charge of $+0.79e$ to $+0.74e$. However, literature reports a variety of different values. Valencia et al. [14] pointed out the large dependency of the partial charge transfer on the method of analysis and presented values of $0.43e$ (Mulliken charge analysis), $0.47e$ (Voronoy), $0.6e$ (Löwdin) and $1.0e$ (Bader). Krishnan et al. [15] found $0.86e$, also by Bader analysis. Song et al. [16] determined $0.68e$ by means of quantum mechanical calculations and comparison with experimental layer spacing, but also pointed out that this value may change with SOC. Finally, Rakotom-ahevitra et al. [17] calculated $0.517e$, using an extra-orbital model. To complicate things further, ϵ_r depends on Z_{Li} quadratically (see Eq. (4)) and is therefore very sensitive to it. For consistency, we will move forward in this work assuming $Z_{Li} = 0.765 \pm 0.05$—the median partial charge to which the SCC converges. The latter indeed directly enters the expression for the Coulombic contribution to the DFTB total energy, as mentioned before, and therefore represents a natural choice within the framework (and within the approximations) of DFTB. We add a generous, but arbitrary measure of uncertainty, and we stress that all absolute numbers for the relative permittivity ϵ_r presented in this work need to be understood with this assumption in mind. However, the same is not true for the electrostatic screening captured by the slopes of the linear regression—this can be taken at face value and may be, depending on the model or method employed, the more valuable property to take into account for future research.

2.2. Computational details

For this study, we used self-consistent-charge Density Functional Tight Binding (SCC-DFTB [18]) as implemented in DFTB+ [19], with the parametrization developed in our group. The corresponding Slater–Koster files are available upon request and have been parametrized and tested as described in [12,20]. The repulsion potential is machine-learned by means of Gaussian Process Regression (GPR) [21].

Geometries have been constructed and analysed by means of the Atomic Simulation Environment (ASE [22]) which we also used as a base framework for all force- and energy-calculations, structure relaxations (specifically using the Broyden–Fletcher–Goldfarb–Shanno (BFGS) algorithm as an optimizer [23]), and transition state calculations. For the latter, we employed the Nudged Elastic Band (NEB, [24]) algorithm with the BFGS optimizer and climbing image [25,26] switched on.

For all DFTB calculations, we used a well converged k-point density of at least 0.1/Å for the z-component of the unit cell. The xy-size of the cell is large enough to sample at the Gamma point. The SCC-tolerance is 10^{-6}. We employed Fermi filling with a Fermi temperature of 0.001 Kelvin, as well as a Broyden mixer [27] for convergence acceleration with a mixing parameter of 0.5. All of these settings have been tested with regard to convergence for the whole range of SOC. As described in [20], our parametrization is meant to be used with the Lennard-Jones dispersion correction [28] switched on.

In terms of supercell size convergence, satisfactory convergence of the extracted slopes of the energies relative to the inverse distances (see Section 2 for details) is reached at distances of around 15 Å between the periodic images of the sampled areas of the investigated layers (see Fig. 2 and Fig. 5), a value we reach or exceed with all used supercells. We point out that convergence of total energies is still not reached at those distances due to the long-ranged nature of the Coulomb interactions, however our property of interest – the previously mentioned slope – is rather robust to total energy shifts of the whole sampled area. Slight further improvements would still be probable with even larger supercells, but due to computation time constraints, and due to the fact that other effects introduce much larger errors to the final results, we chose the supercells described in the previous sections.

3. Results and discussion

3.1. Lithium-intercalant pairwise interaction screening (xy-plane)

In order to sample the pairwise Li-ion interactions within the material, we construct an investigated layer, called *inv(Li)*, consisting of 300 carbon atoms and two Li-ions, one of them fixed in the corner, the other one sampling a number of different positions, as schematically illustrated in Fig. 2. We then combine this investigated layer with varying stackings of empty and filled layers (see Fig. 3), as they predominantly appear in the system according to the staging model. We perform full structure relaxations on the resulting supercells, with two or three layers and 600–900 carbon atoms, for each of the 21 possible Li-ion positions per data point on the SOC axis, and extract the potential energies of the cells. We also perform nudged elastic band (NEB) calculations between all combinations of two relaxed structures,
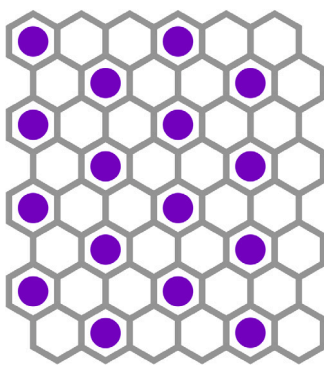
Fig. 3. Illustration of the periodic Li-ion ordering in an adjacent layer at 100% SOC.
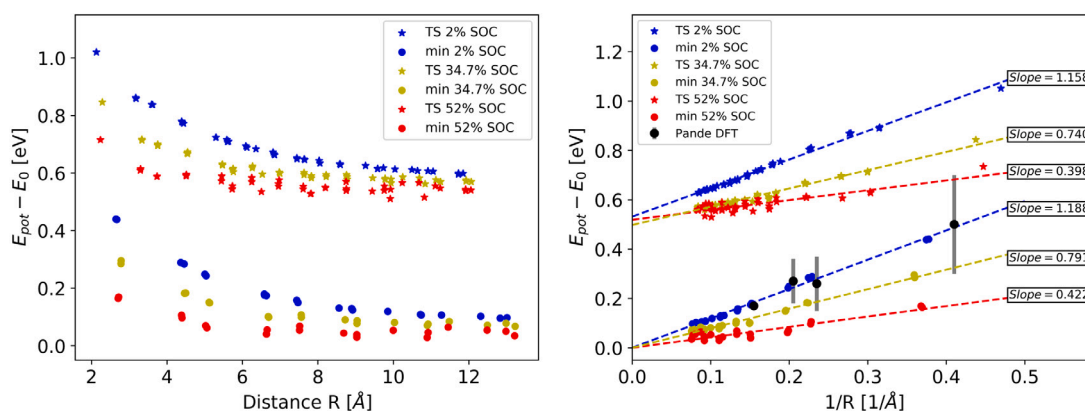

Fig. 4. Approximate Coulomb energies $E_{Coul} \approx E_{pot} - E_0$ of minima and transition states relative to E_0 (at the respective SOC) in dependence of the distance (*left*) and inverse distance (*right*) between the investigated Li-ions at different SOCs (see Table 1). The slopes have been extracted by means of linear regression. The global minima E_0 in the $1/R \to 0$ limit are extrapolated from the linear regression of the slopes of the minima and set to 0 in the plot. The DFT reference is taken from an Ising model based on BEEF-vdW DFT [29]. The data points represent the pair-interactions for next-neighbour, second, third and fourth next neighbour lithium positions. The SOC is not clearly defined without giving the size of the otherwise empty supercell (a limitation of the Ising model), but can be understood as "low" and taken as comparison for our blue data-points.

which have directly adjacent occupied Li-positions, thus acquiring 41 transition states per data point of diffusive next-neighbour jumps.

This is especially relevant for kinetic Monte Carlo applications, where the dynamics are governed by the rates – and therefore, the activation barriers – corresponding to elementary processes bringing the system from one state to another. As our results show, the Coulombic behaviour we get is identical, within method accuracy, for both cases (Fig. 2). This justifies the application of simplified rescaling rules solely based on Coulombic interactions to include the effect of next-neighbour occupations on the elementary barriers, allowing to set up a charged kMC model with one, simple, elementary barrier (the jump of one Li-ion from one site to another in the infinitely dilute limit), and correcting the latter depending on the number and distance of nearest neighbours as well as on the direction of the jump.

By plotting the estimated Coulomb energies $E_{Coul} = E_{pot} - E_0$ as functions of the (inverse) distance between the two Li-ions in the investigated layer, we clearly illustrate how our model captures the Coulombic nature of the interaction close to perfectly in the case where no other Li-ions are present in the adjacent layers (Fig. 4, blue) that could distort the electron density. The very minor scatter in this case likely stems from the small distortions in the carbon structure close to the Li-intercalants and the fact that our full cell relaxations cannot be converged to infinity, but have to be stopped at some threshold forces. In the other two cases, there is some more scatter present, caused by the slightly deformed charge density, due to the filled adjacent layers (one in case of SOC 34.7%, two in case of SOC 52%), but the overall behaviour is still predominantly Coulombic.

Table 1

Results for the data points constructed with an otherwise empty investigated layer with sampled lithium positions *inv(Li)*. The slopes and their RMSEs stem from linear regression of all data points (minima and transition states)—shifted to the same baseline. The corresponding relative permittivities have been calculated via the Coulomb law in Eq. (4).

Structure	Stoichiometry	SOC	Slope [eVÅ]	rel. permit.
inv(Li) − empty	Li_2C_{600}	2.0%	1.168 ± 0.013	7.23 ± 0.86
bilayer graphene	Li_2C_{600}	2.0%	1.111 ± 0.018	7.55 ± 1.04
inv(Li) − empty − full	$Li_{52}C_{900}$	34.7%	0.759 ± 0.018	11.32 ± 1.74
inv(Li) − full	$Li_{52}C_{600}$	52.0%	0.407 ± 0.026	21.04 ± 4.05

In a next step, we extract the slopes from the *1/R*-plots by means of linear regression (see Table 1). We achieve this by shifting the transition state energy levels down to the ground states and then fit all data points at once. Based on that, the relative permittivity ϵ_r can be extracted from the Coulomb law in Eq. (4). For the sake of comparison with experiment, we also perform the same procedure with freestanding bilayer graphene, consisting of one *inv(Li)*-layer between two graphene sheets, which according to our model, has a very similar ϵ_r as (periodic) graphite at the same stoichiometry.

As pointed out in Fig. 4, there is one DFT study available for comparison by Pande et al. [29], and the slope they find at low SOC agrees well with ours. However, due to the computational cost of DFT, they were only able to provide 4 data points, and only at the low end of the range of charge, which is the cheapest to compute.
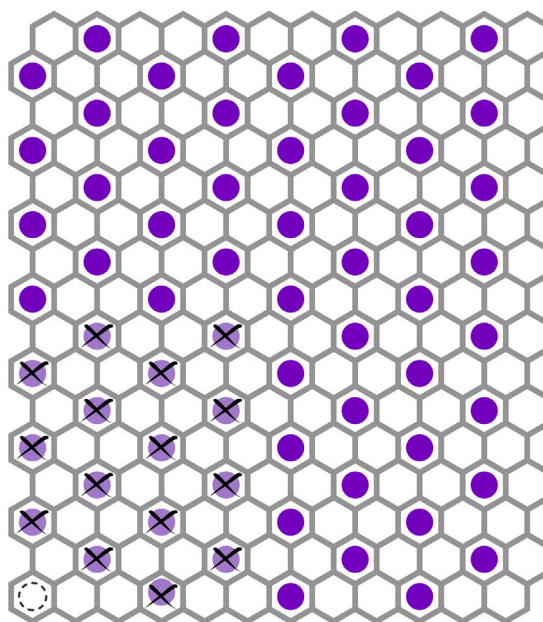
Fig. 5. Illustration of the investigated layer for pairwise Coulombic vacancy-interactions with fixed Li-ions (*purple*) and fixed vacancy #1 (bottom left, dashed circle). Of the positions marked with an "X", the sampled vacancy #2 is located on one, while all others are occupied by Li-ions. This layer will be referred to as *inv(Vac)* throughout this work.
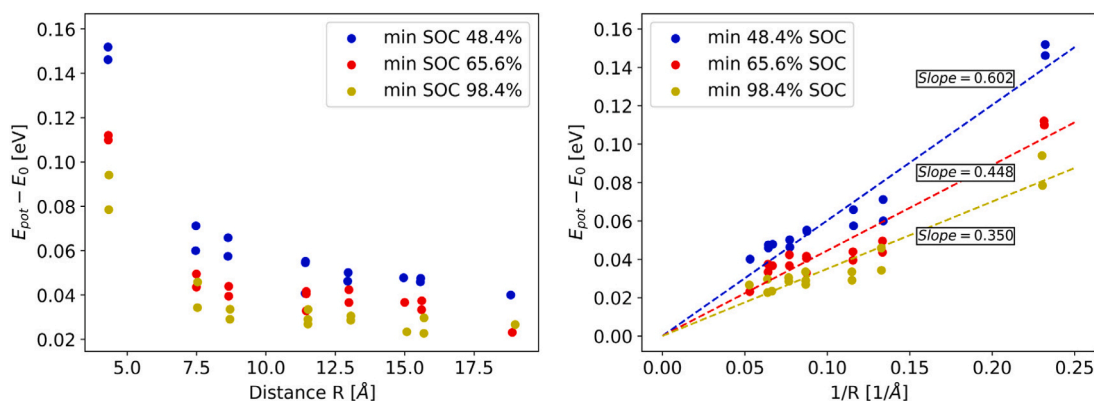

Fig. 6. Approximate Coulomb energies $E_{Coul} \approx E_{pot} - E_0$ of local minima relative to E_0 (at the respective SOC) in dependence of the distance (*left*) and inverse distance (*right*) between the investigated Li-ion vacancies at different SOCs (see Table 2). Slopes have been extracted by means of linear regression. The global minima E_0 in the $1/R \to 0$ limit are extrapolated from the linear regression of the slope and set to 0 in the plot.

Furthermore, Bessler et al. measured a relative permittivity of $\epsilon_r = 6 \pm 2$ for bilayer graphene, which agrees surprisingly well with our result of $\epsilon_r = 7.55 \pm 1.04$ for bilayer graphene with intercalated Li at the level of 2% SOC of a stoichiometrically equivalent HOPG.

3.2. Vacancy pairwise interaction screening (xy-plane)

It is clear that it is not possible to investigate SOCs close to 100% following the same approach, i.e. using the same investigated layer described in the previous chapter. Furthermore, for the higher SOCs, the diffusion mechanism transitions towards vacancy hopping instead of Li-intercalant hopping. Therefore, we introduce a second type of investigated layer (Fig. 5), which samples the pairwise Coulomb interactions between Li-vacancies within a filled layer instead, called *inv(Vac)*.

A key difference here is the fact that, in a filled layer, only every third C_6 ring is occupied by a Li-ion, so the investigated vacancies cannot be placed on each C_6-ring, but only on every third one. Due to this, a slightly larger cell is needed (384 carbon atoms) in order to

Table 2
Results for the data points constructed with a filled investigated layer with sampled vacancy positions *inv(Vac)*. The slopes and their RMSEs stem from linear regression of the data points (minima). The corresponding relative permittivities have been calculated via the Coulomb law in Eq. (4).

Structure	Stoichiometry	SOC	Slope [eVÅ]	rel. permit.
inv(Vac) − empty	$Li_{62}C_{768}$	48.4%	0.602 ± 0.047	14.28 ± 2.95
inv(Vac) − empty − full	$Li_{126}C_{1152}$	65.6%	0.448 ± 0.041	19.28 ± 4.22
inv(Vac) − full	$Li_{126}C_{768}$	98.4%	0.350 ± 0.034	24.70 ± 5.55

sample a reasonable number of data points (15 per SOC), while also keeping the separation from the periodic image large enough to be well converged.

Another consequence is the fact that the diffusion path from one vacancy location to another is not clearly defined—it may be a straight line or pass through one of the two next-neighbour minima in between. Because of this and because we already showed before that the slopes extracted from the minima and from the diffusion path intermediates
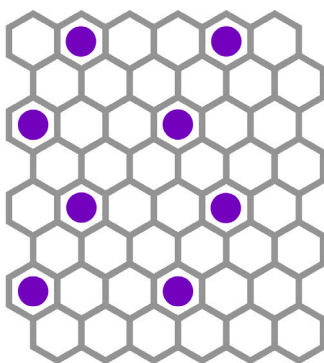
Fig. 7. Illustration of the periodic Li-ion ordering in an adjacent layer at 50% SOC.
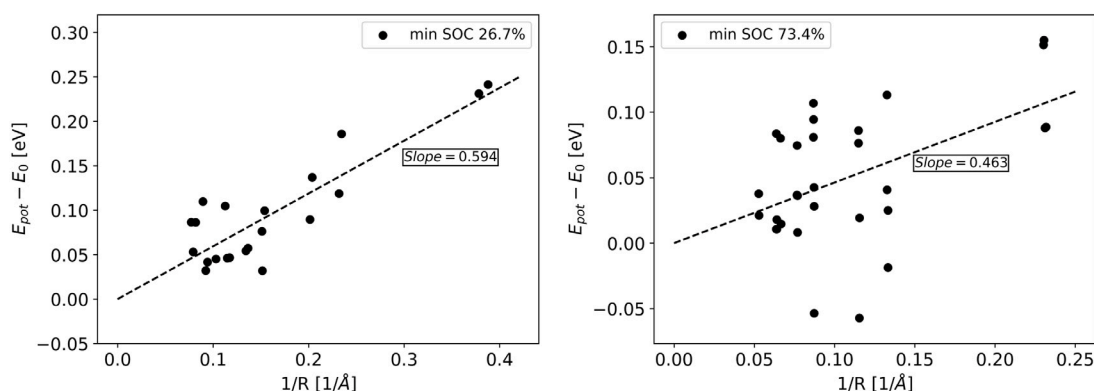

Fig. 8. Approximate Coulomb energies $E_{Coul} \approx E_{pot} - E_0$ of local minima relative to E_0 (at the respective SOC) in dependence of the inverse distance between the investigated sites in the *inv(Li) – dilute* (*left*) and *inv(Vac) – dilute* (*right*) configurations (see Table 3). The global minima E_0 in the $1/R \to 0$ limit are extrapolated from the linear regression of the slope and set to 0 in the plot.

are very similar, we limit our calculations to the minima in this chapter. Other than that, the procedure is the same as in Section 3.1.

As can be seen in Fig. 6, there is more distortion to the Coulombic behaviour present in this case, some of which is even qualitative and cannot just be attributed to the uneven electron density in the adjacent layers. Especially, the data points at "medium" distance (≈ 8 Å in the left plot or ≈ 0.125 1/Å in the right plot of Fig. 6) have lower energy than expected if it was purely governed by the Coulomb law. As pointed out before, this is to be expected within our approximations, since a combination of multiple effects are at play here, that cannot be addressed without explicit treatment of the overlapping local environments of the charge carriers: firstly, for these compositions, there is not just vacuum present in the space between the investigated sites, as it is the case in all configurations in Section 3.1, as well as the closest possible vacancy positions (see Fig. 5). This additional charge density between the sampled sites seems to have an additional stabilizing effect in our DFTB calculations. For vacancy pairs at distances larger than ≈ 10 Å, this effect probably becomes negligible again, since there is hardly any interaction energy left to be screened at those distances. Secondly, the point-charge approximation may be less accurate for a Li-vacancy, than it is for a Li-ion, since the next-neighbour local minima within the host structure are not occupied either. And thirdly, upon inspection of the fully relaxed structures, one realizes that the Li-ions adjacent to the investigated vacancies are not located in the middle of their respective C_6 ring, but slightly displaced towards the vacancy. Due to these additional effects, fitting the potential energies found for these configurations to the unperturbed Coulomb law ($E_{Coul} = E_{pot} - E_0$) is a more severe approximation in the context of the *inv(Vac)* investigated layer than it was for the *inv(Li)* investigated layer. Finally, the slopes

and relative permittivities ϵ_r are summarized in Table 2, analogous to Section 3.1.

3.3. Dilute adjacent layers

One of the complications when investigating Li-GICs is the fact that the same stoichiometry can be realized in a variety of different ways, and while it is known that staged configurations are favoured in equilibrium and in perfect crystals, other – dilute – configurations may still play a role, when the system is under the effects of defects, grain boundaries or nonequilibrium states caused by fast charging. Because of this, we choose to investigate some of these configurations, as well. For this purpose, we make use of the same investigated layers as before, but combine them with an adjacent layer, that is dilutely filled at 50% capacity, with an ordering as illustrated in Fig. 7. In order to realize the periodicity of said layer, a slightly larger cell with 360 carbon atoms is necessary in the case of the Li-ion investigated layer. It is not possible to realize this exact stoichiometry with a perfectly even spacing of the Li-ions, an additional challenge we welcome to further test the robustness of our approach.

As expected, this dilutely filled adjacent layer causes a larger scatter of the potential energies of the individual configurations, which is due to the less even electron density of such a layer compared to a completely empty or full one.

In the *inv(Vac) – dilute* case, this effect is also combined with the already larger scatter we observed and explained previously when sampling this type of investigated layer. We tried to mitigate this by also sampling over two different orientations of the dilute adjacent layers – averaging out the uneven electron density – but the scatter

Table 3
Results for the data points constructed with dilutely filled adjacent layers. The slopes and their RMSEs stem from linear regression of the data points (minima). The corresponding relative permittivities have been calculated via the Coulomb law in Eq. (4). These results correspond to Fig. 8.

Structure	Stoichiometry	SOC	Slope [eVÅ]	rel. permit.
inv(Li) − dilute	$Li_{32}C_{720}$	26.7%	0.594 ± 0.078	14.03 ± 3.12
inv(Vac) − dilute	$Li_{94}C_{768}$	73.4%	0.463 ± 0.152	21.45 ± 9.52

remains very large, which leads to a much larger uncertainty of the resulting slope and relative permittivity ϵ_r (see Table 3).

Nevertheless, the Coulombic nature of the interaction is still clearly visible despite the scatter at least for the *inv(Li) − dilute* case (Fig. 8, left), and is expected to be captured by the (admittedly rough) linear fit in the other case as well – yet of course with a larger uncertainty. Indeed, the resulting slope is still in line with the overall behaviour we find throughout the whole system.

3.4. Dielectric screening in the xy-plane vs. in z-direction

Thus far, we have focused on the dielectric behaviour of Li-GICs parallel to the graphene sheets (xy-plane), because that is what governs the diffusion and intercalation of the Li-ions. However, real graphite anodes and experimental samples often come in powder form, with graphite nanoparticles in random spatial orientation. Experimental measurements of the dielectric behaviour of such samples cannot be directly compared to the results we have presented so far. Therefore, we also investigate the dielectric behaviour in z-direction (perpendicular to the graphene sheets).

In order to do so, we construct a 15-layered supercell with a stoichiometry of Li_2C_{720} which corresponds to an SOC of 1.7%. We sample 5 of the 15 layers (to ensure no self-interaction with the periodic image) with one pair of Li-ions, placed in positions both directly above each other and shifted by one next-neighbour position (those latter interactions are not perfectly in z-direction, but still "through" the graphene sheets). As can be seen, the resulting electrostatic behaviour is not purely Coulombic (see Fig. 9). Similar to the results for the investigated layer *inv(Vac)*, the presence of charge carriers in between the investigated Li positions seems to cause some extra, nonlinear screening. Holding on to the assumption of a linear trend, a linear fit finds a slope of 0.411 ± 0.054, which translates to a relative permittivity of $\epsilon_z = 21.35 \pm 5.50$—significantly larger than the in-plane relative permittivity ϵ_{xy} we find at similar SOC. Based on this, we can average over the 3 spatial dimensions in order to provide a rough estimate of the relative permittivity ϵ_r of randomly oriented graphite powder at very low SOC, simply by applying:

$$\epsilon_r = (2\epsilon_{xy} + \epsilon_z)/3 = 11.93 \tag{5}$$

This result is comparable to the $\epsilon_r \approx 15$ found by Hotta et al. [4] in the GHz range, but again, it is not entirely clear that this comparison is physically valid. Once a more reliable consensus is reached in experiment, our estimation of the partial charge can be further validated. It is also necessary to point out that grain-boundary and grain-size effects may play a significant role, especially the smaller the particles in the powder get, but these effects are not considered at all in the numbers we present here—those are simply intended to help with comparison between our results and experiments.

3.5. Relative permittivity ϵ_r as a function of the SOC

Putting the previous results together (see Fig. 10), we find an approximately linear dependency of the relative permittivity ϵ_r (in the xy-plane) on the SOC of the Li-GIC. Between 20% and 80% SOC, we observe some additional effects of the local ordering – dilute or staged – and of whether Li-ions in the otherwise empty layers or Li-ion vacancies in the otherwise full layers are sampled. These deviations are largest at around 50% SOC, but the average ϵ_r of configurations at roughly equal SOC are still close to the weighted linear regression fit, so the more macroscopic a viewpoint is taken, the less these local phenomena matter. The final uncertainty intervals are translated through Eq. (4) and stem from a combination of our arbitrarily chosen uncertainty in the partial charge Z_{Li}, as described in the methodology section, and the root mean square error (RMSE) of the slope, which is returned by the linear regression and caused by scatter around the Coulombic behaviour, which in turn is due to variations in the electron densities of adjacent layers, local structural perturbations and similar effects not captured by the approximations we made when introducing $E_{Coul} \approx E_{pot} - E_0$ (as described throughout the previous sections), as well as the intrinsic limited accuracy of DFTB.

3.6. Literature overview

The dielectric behaviour of Li-GICs, and solid materials in general, is significantly more complicated than the expression "dielectric constant" would suggest, and is governed by vastly different physics at different frequencies of a probing field. Because of this, one needs to carefully examine whether or not reported numbers from literature can meaningfully be compared or not, as will be discussed in this section. In the static limit, which this work aims to investigate, the probing field is essentially the electrostatic field of the intercalated ion itself, and no periodic movement beyond thermal fluctuations of the electrons is induced. However, this picture changes in the kHZ range, where the entire charge carrier density oscillates with the probing field, causing large polarization and large dielectric screening. For example, Chung et al. [1] measured an RP of $\epsilon_r = 2100$ for highly oriented pyrolytic
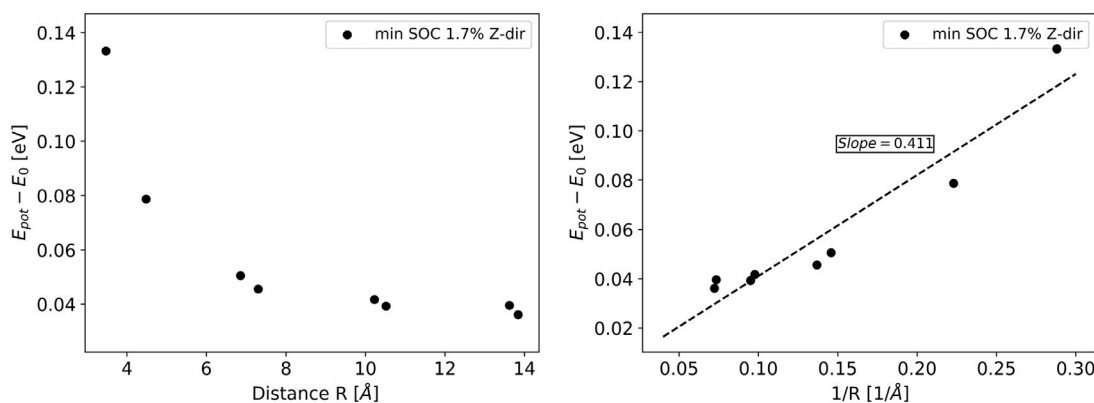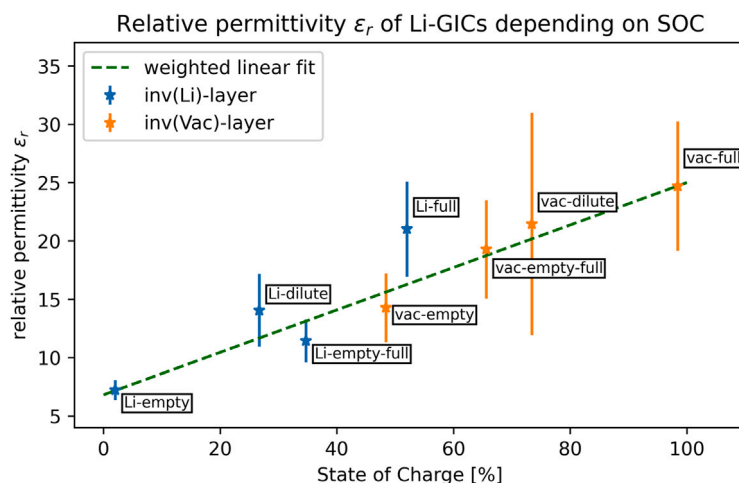

Fig. 9. Approximate Coulomb energies $E_{Coul} \approx E_{pot} - E_0$ of local minima relative to E_0 (at the respective SOC) in dependence of the distance (*left*) and inverse distance (*right*) between the investigated Li-ions in z-direction.

Fig. 10. Relative permittivity ϵ_r in xy-plane (parallel to the graphene sheets), found for different configurations of the Li-GIC material as a function of the respective SOC . The weighted linear fit yields the expression $\epsilon_r(SOC) = 6.8 + 18.2 \cdot SOC$.

graphite (HOPG) and even higher ones for other carbon structures, at 2–10 KHz. Moving on to the GHz regime, a balance is reached where the field oscillations are too fast for macroscopic bulk currents to build up, and a situation occurs that is arguably similar to the static limit and *may* serve as comparison for our research. Hotta et al. [4] put forward a dielectric constant for graphite powder of $\epsilon_r \approx 15$, at 6 GHz. Finally, at even higher frequencies beyond THz, the electric field becomes high enough in energy to excite a significant number of electrons, again creating a physically different situation with much lower dielectric screening, which converges to transparency in the $\omega \to \infty$ limit. A study by Jellison et al. [30] in the frequency regime of visible light finds an RP in xy-plane for HOPG of $\epsilon_r = 4.21$, which, for the previously mentioned reasons, cannot be used as comparison either and is expected to serve as a lower bound in the following.

It is apparent that there is a glaring lack of studies investigating the *exact* property of interest to us, which is – again – the electrostatic dielectric response of a perfect graphite crystal in xy-plane, i.e. parallel to the graphene sheets, as experienced by some internal charge carriers (in this case Li-ions and vacancies). There are some studies available on graphene, either on some substrate or quasi-freestanding, with results ranging from $\epsilon_r = 2.2 - 5.0$ by Elias et al. [31] to $\epsilon_r = 15.4$ by Reed et al. [11], and another study by Bostwick et al. finding $\epsilon_r \approx 4.4$ [32], none of which can serve as direct comparison to our research either. However, there is a study on bilayer graphene (which according to our calculations can be compared with graphite quite well) by Bessler et al. [33], putting forward an RP of $\epsilon_r = 6 \pm 2$. This is likely the most reliable direct experimental comparison currently available to us.

In terms of theoretical approaches to determining the dielectric response of materials, substantial work has been done on water [34–37]. There is also some promising work by Gigli et al. [38] in the development of an integrated machine learning model predicting the dielectric response of $BaTiO_3$. However, all these methods are reliant on the presence of polarizable dipoles within the system, which is not the case for Li-GICs.

4. Conclusion

With this work, we present the first rigorous investigation of the dielectric behaviour of lithium–graphite intercalation compounds (Li-GICs) for the entire functional range of charge during the application as anode of a modern Li-ion battery. In doing so, we provide a straightforward approach for investigating the intrinsic relative permittivity of materials with mobile charge carriers in the electrostatic limit, that can be applied to other materials in the future—given that sufficiently

fast and long-ranged computational methods are available. Thanks to our recently published DFTB parametrization [12,20], we are able to sample the long-ranged Coulomb interactions between two intercalated charge carriers (Li-ions or vacancies) in a variety of stoichiometries and configurational realizations thereof. By examining the approximations we made during this process, we additionally outline ways to further improve this methodology in the future.

The primary finding of this work is the mostly linear dependency from $\epsilon_r \approx 7$ at SOC 0% to $\epsilon_r \approx 25$ at SOC 100% of the relative permittivity on the state of charge. With this, we make valuable contributions to the future modelling of functional materials by means of charged kinetic Monte Carlo and continuum simulations and to the general understanding of Li-GICs. Our results hold for qualitatively different realizations of the intermediate stoichiometries (staged or dilute), as well as both possible types of diffusion (Li-ion or vacancy). The few available experimental studies agree reasonably well with our results, but more investigation is necessary to really pinpoint the quantitative dielectric response, especially at higher SOC. Thanks to our results, it is now clear that only two measurements – one at low and one at high SOC – would suffice for that purpose.

We find that an approximation neglecting the local distortions of the structure and of the electron density caused by the sampled charge carriers holds very well if those charge carriers are Li-ions, and slightly less well, but still within reason, in the vacancy case. Future improvements could be achieved by correcting with some local descriptor based machine learning model that is specifically trained to pick up those local effects.

Additionally, we provide a rough estimate on how the relative permittivity of a perfect crystal and a powder can be compared. Grain-boundary effects are neglected, but should be uniform with space direction and therefore should not have any qualitative impact on our results. This is useful for translating an experimental result for (inter-calated) graphite powder to the internal xy-plane relative permittivity the Li-ions feel locally, which is the one that is actually relevant for their diffusion behaviour.

CRediT authorship contribution statement

Simon Anniés: Conceptualization, Investigation, Methodology, Data curation, Visualization, Software, Formal analysis, Writing – original draft, Writing – review & editing. **Christoph Scheurer:** Conceptualization, Funding acquisition, Supervision, Resources, Writing – review & editing. **Chiara Panosetti:** Conceptualization, Software, Validation, Supervision, Writing – review & editing.

Declaration of competing interest

The authors declare that they have no known competing financial interests or personal relationships that could have appeared to influence the work reported in this paper.

Data availability

Data will be made available on request.

Acknowledgements

References

[1] D. Chung, X. Xi, Factors that govern the electric permittivity of carbon materials in the graphite allotrope family, Carbon 184 (2021) 245–252.

[2] C. Grosu, C. Panosetti, S. Merz, P. Jakes, S. Matera, R.-A. Eichel, J. Granwehr, C. Scheurer, Revisiting the storage capacity limit of graphite battery anodes: spontaneous lithium overintercalation at ambient pressure, 2021, arXiv preprint arXiv:2107.11137.

[3] N. Daumas, A. Herold, Relations between phase concept and reaction mechanics in graphite insertion compounds, C. R. Acad. Sci. C 268 (1969) 373.

[4] M. Hotta, M. Hayashi, M.T. Lanagan, D.K. Agrawal, K. Nagata, Complex permittivity of graphite, carbon black and coal powders in the ranges of X-band frequencies (8.2 to 12.4 GHz) and between 1 and 10 GHz, ISIJ Int. 51 (2011) 1766.

[5] E.M. Gavilán-Arriazu, O.A. Pinto, B.L. De Mishima, D. Barraco, O.A. Oviedo, E.P.M. Leiva, Kinetic Monte Carlo applied to the electrochemical study of the Li-ion graphite system, Electrochim. Acta 331 (2020) 135439.

[6] E.M. Gavilán-Arriazu, M. Mercer, D.E. Barraco, H. Hoster, E. Leiva, Kinetic Monte Carlo simulations applied to Li-ion and post Li-ion batteries: a key link in the multi-scale chain, Prog. Energy 3 (2021).

[7] R.N. Methekar, P.W. Northrop, K. Chen, R.D. Braatz, V.R. Subramanian, Kinetic Monte Carlo simulation of surface heterogeneity in graphite anodes for lithium-ion batteries: passive layer formation, J. Electrochem. Soc. 158 (2011) A363.

[8] J.M. Dean, S.W. Coles, W.R. Saunders, A.R. McCluskey, M.J. Wolf, A.B. Walker, B.J. Morgan, Overscreening and underscreening in solid-electrolyte grain boundary space-charge layers, Phys. Rev. Lett. 127 (2021) 135502.

[9] M. Casalegno, G. Raos, R. Po, Methodological assessment of kinetic Monte Carlo simulations of organic photovoltaic devices: The treatment of electrostatic interactions, J. Chem. Phys. 132 (2010) 094705.

[10] S. Hein, T. Danner, A. Latz, An electrochemical model of lithium plating and stripping in lithium ion batteries, ACS Appl. Energy Mater. 3 (2020) 8519.

[11] J.P. Reed, B. Uchoa, Y.I. Joe, Y. Gan, D. Casa, E. Fradkin, P. Abbamonte, The effective fine-structure constant of freestanding graphene measured in graphite, Science 330 (2010) 805.

[12] S. Anniés, C. Panosetti, M. Voronenko, D. Mauth, C. Rahe, C. Scheurer, Accessing structural, electronic, transport and mesoscale properties of Li-GICs via a complete DFTB model with machine-learned repulsion potential, Materials 14 (2021) 6633.

[13] P. Koskinen, V. Mäkinen, Density-functional tight-binding for beginners, Comput. Mater. Sci. 47 (2009) 237.

[14] F. Valencia, A.H. Romero, F. Ancilotto, P.L. Silvestrelli, Lithium adsorption on graphite from density functional theory calculations, J. Phys. Chem. B 110 (2006) 14832.

[15] S. Krishnan, G. Brenet, E. Machado-Charry, D. Caliste, L. Genovese, T. Deutsch, P. Pochet, Revisiting the domain model for lithium intercalated graphite, Appl. Phys. Lett. 103 (2013) 251904.

[16] M.K. Song, S. Do Hong, K.T. No, The structure of lithium intercalated graphite using an effective atomic charge of lithium, J. Electrochem. Soc. 148 (2001) A1159.

[17] A. Rakotomahevitra, C. Demangeat, J. Parlebas, G. Moraitis, E. Razafindrakoto, Electronic structure and properties of light atoms intercalated in graphite, J. Phys.: Condens. Matter 4 (1992) 4621.

[18] M. Elstner, D. Porezag, G. Jungnickel, J. Elsner, M. Haugk, T. Frauenheim, S. Suhai, G. Seifert, Self-consistent-charge density-functional tight-binding method for simulations of complex materials properties, Phys. Rev. B 58 (1998) 7260.

[19] B. Hourahine, B. Aradi, V. Blum, F. Bonafé, A. Buccheri, C. Camacho, C. Cevallos, M.Y. Deshaye, T. Dumitrică, A. Dominguez, S. Ehlert, M. Elstner, T. van der Heide, J. Hermann, S. Irle, J.J. Kranz, C. Köhler, T. Kowalczyk, T. Kubař, I.S. Lee, V. Lutsker, R.J. Maurer, S.K. Min, I. Mitchell, C. Negre, T.A. Niehaus, A.M.N. Niklasson, A.J. Page, A. Pecchia, G. Penazzi, M.P. Persson, J. Řezáč, C.G. Sánchez, M. Sternberg, M. Stöhr, F. Stuckenberg, A. Tkatchenko, V.W. z. Yu, T. Frauenheim, DFTB+, a software package for efficient approximate density functional theory based atomistic simulations, J. Chem. Phys. 152 (2020) 124101.

[20] C. Panosetti, S.B. Anniés, C. Grosu, S. Seidlmayer, C. Scheurer, DFTB modeling of lithium-intercalated graphite with machine-learned repulsive potential, J. Phys. Chem. A 125 (2021) 691.

[21] C. Panosetti, A. Engelmann, L. Nemec, K. Reuter, J.T. Margraf, Learning to use the force: Fitting repulsive potentials in density-functional tight-binding with gaussian process regression, J. Chem. Theory Comput. 16 (2020) 2181.

[22] S.R. Bahn, K.W. Jacobsen, An object-oriented scripting interface to a legacy electronic structure code, Comput. Sci. Eng. 4 (2002) 56.

[23] D.F. Shanno, On Broyden-Fletcher-Goldfarb-Shanno method, J. Optim. Theory Appl. 46 (1985) 87.

[24] B.J. Berne, G. Ciccotti, D.F. Coker, Classical and Quantum Dynamics in Condensed Phase Simulations: Proceedings of the International School of Physics, World Sci., 1998.

[25] G. Henkelman, H. Jónsson, Improved tangent estimate in the nudged elastic band method for finding minimum energy paths and saddle points, J. Chem. Phys. 113 (2000) 9978.

[26] G. Henkelman, B.P. Uberuaga, H. Jónsson, A climbing image nudged elastic band method for finding saddle points and minimum energy paths, J. Chem. Phys. 113 (2000) 9901.

[27] D.D. Johnson, Modified Broyden's method for accelerating convergence in self-consistent calculations, Phys. Rev. B 38 (1988) 12807.

[28] L. Zhechkov, T. Heine, S. Patchkovskii, G. Seifert, H.A. Duarte, An efficient a posteriori treatment for dispersion interaction in density-functional-based tight binding, J. Chem. Theory Comput. 1 (2005) 841.

[29] V. Pande, V. Viswanathan, Robust high-fidelity DFT study of the lithium-graphite phase diagram, Phys. Rev. Mater. 2 (2018) 125401.

[30] G.E. Jellison Jr., J.D. Hunn, H.N. Lee, Measurement of optical functions of highly oriented pyrolytic graphite in the visible, Phys. Rev. B 76 (2007) 085125.

[31] D. Elias, R. Gorbachev, A. Mayorov, S. Morozov, A. Zhukov, P. Blake, L. Ponomarenko, I. Grigorieva, K. Novoselov, F. Guinea, et al., Dirac cones reshaped by interaction effects in suspended graphene, Nat. Phys. 7 (2011) 701.

[32] A. Bostwick, F. Speck, T. Seyller, K. Horn, M. Polini, R. Asgari, A.H. MacDonald, E. Rotenberg, Observation of plasmarons in quasi-freestanding doped graphene, Science 328 (2010) 999.

[33] R. Bessler, U. Duerig, E. Koren, The dielectric constant of a bilayer graphene interface, Nanoscale Adv. 1 (2019) 1702.

[34] G. Raabe, R.J. Sadus, Molecular dynamics simulation of the dielectric constant of water: The effect of bond flexibility, J. Chem. Phys. 134 (2011) 234501.

[35] J. Aragones, L. MacDowell, C. Vega, Dielectric constant of ices and water: a lesson about water interactions, J. Phys. Chem. A 115 (2011) 5745.

[36] M. Sharma, R. Resta, R. Car, Dipolar correlations and the dielectric permittivity of water, Phys. Rev. Lett. 98 (2007) 247401.

[37] L. Ruiz Pestana, O. Marsalek, T.E. Markland, T. Head-Gordon, The quest for accurate liquid water properties from first principles, J. Phys. Chem. Lett. 9 (2018) 5009.

[38] L. Gigli, M. Veit, M. Kotiuga, G. Pizzi, N. Marzari, M. Ceriotti, Thermodynamics and dielectric response of $BaTiO_3$ by data-driven modeling, 2021, arXiv preprint arXiv:2111.05129.